

# Spectroscopy and modeling of $^{171}\text{Yb}$ Rydberg states for high-fidelity two-qubit gates

Michael Peper,<sup>1</sup> Yiyi Li,<sup>1</sup> Daniel Y. Knapp,<sup>1,2,\*</sup> Mila Bileska,<sup>1,2</sup> Shuo Ma,<sup>1,2</sup> Genyue Liu,<sup>1</sup> Pai Peng,<sup>1</sup> Bichen Zhang,<sup>1</sup> Sebastian P. Horvath,<sup>1</sup> Alex P. Burgers,<sup>1,†</sup> and Jeff D. Thompson<sup>1,‡</sup>

<sup>1</sup>*Department of Electrical and Computer Engineering,  
Princeton University, Princeton, NJ 08544, USA*

<sup>2</sup>*Department of Physics, Princeton University, Princeton, NJ 08544, USA*

(Dated: November 15, 2024)

Highly excited Rydberg states and their interactions play an important role in quantum computing and simulation. These properties can be predicted accurately for alkali atoms with simple Rydberg level structures. However, an extension of these methods to more complex atoms such as alkaline-earth atoms has not been demonstrated or experimentally validated. Here, we present multichannel quantum defect (MQDT) models for highly excited  $^{174}\text{Yb}$  and  $^{171}\text{Yb}$  Rydberg states with  $L \leq 2$ . The models are developed using a combination of existing literature data and new, high-precision laser and microwave spectroscopy in an atomic beam, and validated by detailed comparison with experimentally measured Stark shifts and magnetic moments. We then use these models to compute interaction potentials between two Yb atoms, and find excellent agreement with direct measurements in an optical tweezer array. From the computed interaction potential, we identify an anomalous Förster resonance that likely degraded the fidelity of previous entangling gates in  $^{171}\text{Yb}$  using  $F = 3/2$  Rydberg states. We then identify a more suitable  $F = 1/2$  state, and achieve a state-of-the-art controlled-Z gate fidelity of  $\mathcal{F} = 0.994(1)$ , with the remaining error fully explained by known sources. This work establishes a solid foundation for the continued development of quantum computing, simulation and entanglement-enhanced metrology with Yb neutral atom arrays.

## I. INTRODUCTION

Rydberg-mediated interactions between neutral atoms in optical tweezer arrays are enabling for quantum computing, simulation and quantum-enhanced metrology [1–4]. To realize high-fidelity operations, a detailed understanding of the properties of the Rydberg states and their interactions is required. Alkali atoms such as Rb or Cs can be described by simple quantum defect models, which have been validated by extensive spectroscopy [5–11]. This allows the wavefunctions, and in turn, matrix elements, interaction potentials and decay rates to be computed [12–14]. Experimental studies have confirmed the predicted interaction potentials [15–17] and decay rates [18–20]. A particularly stringent test of the interaction model comes from spectroscopy of so-called macrodimer states [21–24].

Many recent experiments have focused on divalent alkaline-earth-like atoms, in particular Sr [25–28] and Yb [29–32]. Tweezer arrays of  $^{88}\text{Sr}$  Rydberg atoms have been used to study many-body dynamics [33, 34] and entanglement-enhanced optical clocks [35, 36]. On the other hand,  $^{171}\text{Yb}$  is ideal for use as a qubit for quantum computing, with demonstrated long coherence times for the pure nuclear spin qubit with  $I = 1/2$  [30–32],

mid-circuit measurement and atom reloading [37, 38] and hardware efficient error correction strategies [39, 40].

A challenge to the continued development of divalent atomic qubits, particularly those based on  $^{171}\text{Yb}$ , is the relative lack of spectroscopic information and models for the behavior of the Rydberg states. The Rydberg states of divalent atoms are more complex than alkali atoms, because of the presence of singlet and triplet Rydberg series, interactions between series converging to other ionization thresholds (*i.e.*, series perturbers), and hyperfine coupling (in the case of isotopes with nuclear spin  $I > 0$ , such as  $^{87}\text{Sr}$  and  $^{171}\text{Yb}$ ). These states can be described in the framework of multichannel quantum defect theory (MQDT) [41, 42], which in turn allows the computation of matrix elements, interaction potentials and decay rates [43, 44].

Single-channel approximations have been used to predict interaction potentials in both  $^{174}\text{Yb}$  and  $^{88}\text{Sr}$ , which both have no nuclear spin ( $I = 0$ ) [43, 45]. Moreover, relatively complete MQDT descriptions of  $^{88}\text{Sr}$  have been developed and used to study lifetimes and branching ratios [43], and MQDT models have been developed to fit spectroscopic data for certain Rydberg series in  $^{174}\text{Yb}$  [46–50]. The energies of certain Rydberg series in  $^{87}\text{Sr}$  ( $I = 9/2$ ) have also been determined [51] and used to predict  $C_6$  coefficients using an MQDT formalism [52]. However, to the best of our knowledge, there is no comprehensive spectroscopy or MQDT model of the Rydberg states of  $^{171}\text{Yb}$ , and no MQDT interaction models for divalent atoms have been experimentally verified at a level approaching the precision of alkali atom models.

In this article, we present four main results. First, we present refined MQDT models for the Rydberg states of  $^{174}\text{Yb}$  with  $L \leq 2$  (Section II). This set of states is suf-

\* Current address: Department of Physics and Astronomy, Laser-Lab, Vrije Universiteit Amsterdam, de Boelelaan 1081, 1081 HV Amsterdam, The Netherlands

† Current address: Department of Electrical and Computer Engineering, College of Engineering, University of Michigan, Ann Arbor, MI 48109, USA.

‡ jdthompson@princeton.edu

ficient to accurately predict the interactions and polarizability of the  $L = 0$  states that are most frequently used in experiments. This extends prior work [46, 49, 50, 53–61] by incorporating new spectroscopic measurements and re-fitting all of the MQDT models simultaneously with a global fit for improved consistency and accuracy. Furthermore, we determine singlet-triplet mixing angles by comparison to experimental measurements of the static dipole polarizability, which are undetermined by the state energies alone [62]. We find excellent agreement with measured Rydberg state energies, polarizabilities and magnetic moments.

Next, we extend these models to describe  $^{171}\text{Yb}$  states with  $L \leq 2$  by including the hyperfine interaction (Sec. III). The models are refined and validated by comparison to extensive laser and microwave spectroscopy of  $^{171}\text{Yb}$  Rydberg states from an atomic beam apparatus. We also test the MQDT model matrix elements by comparison to measured static dipole polarizabilities and magnetic moments, finding excellent agreement.

Third, we use the  $^{171}\text{Yb}$  MQDT models to compute the interaction potential for Rydberg atom pairs, which we verify against direct measurements using pairs of atoms in an optical tweezer array (Sec. IV). We show that the  $^{171}\text{Yb}$   $F = 3/2$  Rydberg state that was previously used to implement entangling gates [31, 40] has a surprisingly small Förster defect ( $< 10$  MHz) over a large range of effective principal quantum number  $\nu$ . This gives rise to an imperfect blockade, and we conjecture that it is responsible for the discrepancy between the measured ( $\mathcal{F} = 0.980(1)$ ) and predicted ( $\mathcal{F}_{th} = 0.989$ ) gate error in Ref. [40].

Finally, in Sec. V we leverage these models to predict that certain  $F = 1/2$  states should have a larger Förster defect, giving rise to a cleaner blockade and improved gate fidelity. We then experimentally demonstrate improved gates with  $\mathcal{F} = 0.994(1)$ . Importantly, the dominant remaining errors are well-understood (arising from Rydberg state decay and Doppler shifts), which is promising for future improvements in gate fidelity with increased laser power.

This work solidifies the foundation for future quantum computing, simulation and quantum-enhanced metrology applications of  $^{171}\text{Yb}$  Rydberg atoms. The developed MQDT models not only reproduce the energies of ytterbium Rydberg states, but also enable an accurate prediction of matrix elements, polarizabilities, and Rydberg interactions within a self-consistent framework. This comprehensive approach also establishes the basis for treating other complex atomic systems including  $^{87}\text{Sr}$  [63], and lanthanide atoms such as Ho [64] or Er [65].

## II. MULTICHANNEL QUANTUM DEFECT MODEL OF $^{174}\text{Yb}$

Fig. 1a illustrates the basic principle of MQDT, in the context of  $^{174}\text{Yb}$  (the most abundant isotope, with nu-

clear spin  $I = 0$ ). The ground state of  $^{174}\text{Yb}$  has the electronic configuration  $[\text{Xe}]4f^{14}6s^2$ , and the states of primary interest are singly-excited states  $[\text{Xe}]4f^{14}6snl$ , where  $n, l$  are the principal quantum number and orbital angular momentum of the excited electron (the Xe core and  $4f^{14}$  electrons are omitted henceforth, unless otherwise noted). These states are approximately described in  $LS$  coupling by the term symbol  $^{2S+1}L_J$  with total electron spin  $S = \{0, 1\}$ ,  $L = l$ , and total electronic angular momentum  $J$ . In single-channel quantum defect theory, these states form isolated series converging to the ground state of the  $^{174}\text{Yb}^+$  ion with the electron configuration  $6s^1$ . The energy of the states in this series is  $E_n = I_{6s} - R/\nu_{6s}^2$ , where  $\nu_{6s} = n - \mu$  is the effective quantum number, and  $\mu(n, L, J)$  is the quantum defect that captures the interaction with the core for that series, with only weak dependence on  $n$ .

Compared to lighter divalent atoms such as Sr, this picture is complicated for Yb by a relatively high density of low-lying excited states in  $\text{Yb}^+$ , which give rise to doubly-excited states in the energy range of interest (*e.g.*,  $[\text{Xe}]4f^{14}6pnl$ ). These doubly-excited states are part of additional Rydberg series converging to higher thresholds (Fig. 1a), and couple to the singly-excited Rydberg states of interest through configuration interactions, which mix series with the same  $J$  and parity. This alters the energy spectrum through level repulsion (*i.e.*, series perturbers), which gives rise to sharp variations in  $\mu$  with  $n$ , and correspondingly modifies the wavefunctions needed to compute quantities of interest such as matrix elements, interactions and lifetimes. This effect can be described quantitatively using MQDT, treating the interacting series as a set of coupled channels and parameterizing the interactions with a small number of mixing angles or a  $K$ -matrix [66, 67]. We give a pedagogical introduction of the MQDT approach in Appendix A.

Previous work in  $^{174}\text{Yb}$  has reported spectroscopic measurements of certain  $S$ ,  $P$ ,  $D$ , and  $F$  states, along with MQDT models that adequately reproduce their energy spectrum [29, 46–49] (a comprehensive summary can be found in Ref. [50]). We improved these models by performing additional microwave spectroscopy of some  $P$  Rydberg states between  $n = 30 - 50$  (using an atomic beam apparatus, App. B). The resulting MQDT model is summarized in Fig. 1b.

However, mixing between channels converging to the same threshold (*i.e.*, singlet-triplet mixing) does not alter the state energies [62], but can significantly alter wavefunctions and matrix elements [68]. To develop an MQDT model with accurate wavefunctions, we augment the traditional approach of fitting the energy levels with additional measurements of the static dipole polarizability of the atomic states, which depend directly on the matrix elements and wavefunctions.

In Fig. 1c, we present measurements of the static dipole polarizability (red dots) for the  $^1S_0$  series, near its crossing with  $^3P_1$ . By adjusting the single-triplet mixing angle in the  $^{1,3}P_1$  MQDT model, we can accurately capture the

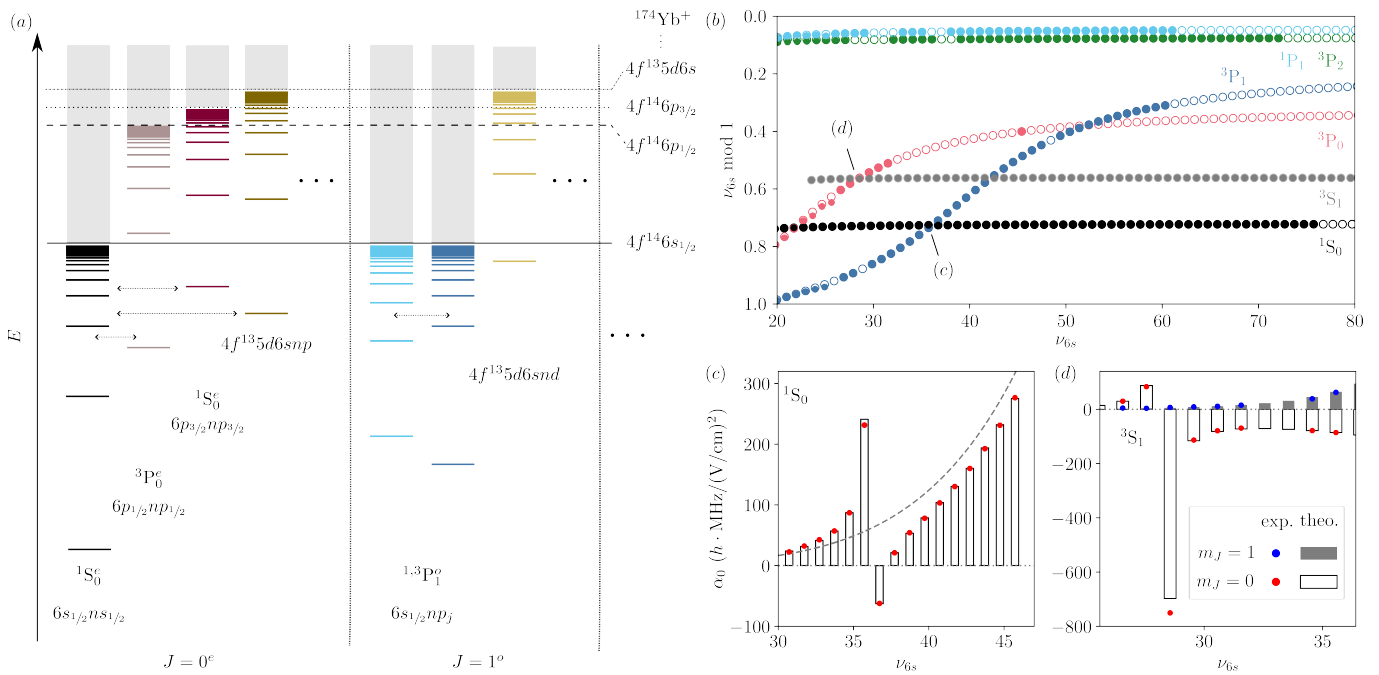


Figure 1. (a) Schematic diagram of several Rydberg series  $^{174}\text{Yb}$ , illustrating the principle of MQDT. Both singly-excited ( $6s_{1/2}nl$ ) and doubly-excited (e.g.,  $6pnl$ ) series are included, converging to different thresholds corresponding to excited states of the  $^{174}\text{Yb}^+$  ion (note that in this schematic diagram, the energy level spacings are not to scale, and only the subset of channels most relevant for the presented MQDT models are included). The Rydberg series are sorted by total angular momentum  $J$  and parity (even/odd denoted by  $e/o$  superscripts).  $LS$  coupling term symbols are written where possible (i.e.,  $^1S_0$ ). Configuration interactions mix series with the same  $J$  and parity, as indicated by the horizontal arrows. (b) Lu-Fano-like plot of the  $L = 0$  and  $L = 1$  Rydberg series of  $^{174}\text{Yb}$ , showing the fractional part of the quantum defect ( $\nu_{6s} \bmod 1$ ) as a function of the effective principal quantum number,  $\nu_{6s}$ . The open circles show the eigenstates predicted by the MQDT model, while the filled circles show experimentally determined energies. (c) Static dipole polarizability  $\alpha_0$  (see Eq. (B1)) of the  $n^1S_0$  series close to a level crossing with the  $n^3P_1$  series (red points: experiment, bars: MQDT prediction). The gray, dashed line indicates the expected  $\nu^7$  scaling in the absence of singlet-triplet mixing. (d) Static dipole polarizability  $\alpha_0$  of the  $n^3S_1$  series near a crossing with  $n^3P_0$ . The experimental data for the polarizability of the  $m_J = 0$  (red) and  $m_J = 1$  (blue) states agrees well with the theoretical predictions from the MQDT model.

resonance-like feature, which deviates strongly from the usual  $\nu^7$  polarizability trend [69]. The final model predicts a triplet character of the  $^1P_1$  Rydberg series that varies between 6.30(3)% for  $n = 40$  and 2.96(16)% for  $n = 100$ , which is consistent with previous estimates based on measurements of diamagnetic shifts [57], but considerably more precise (Appendix D 2). As an additional check of the predicted MQDT wavefunctions, we characterize the scalar and tensor polarizability of the  $n^3S_1$  Rydberg series near its crossing with  $^3P_0$ , finding excellent agreement (Fig. 1d). The measured polarizabilities of  $6sns^1S_0$  and  $6sns^3S_1$  states are summarized in the supplemental material [70].

Through a similar analysis for the  $^{1,3}D_2$  using literature data for the magnetic moments of these states [59] we find a triplet character of  $n^1D_2$  Rydberg states of approximately 15% (details in Appendix D 5).

Other details of the spectroscopy are presented in Appendix B. A complete tabulation of the model parameters and the compiled spectroscopic data are presented in the supplemental material [70]. A more detailed description of the developed MQDT models is presented in

Appendix D.

### III. MQDT MODEL OF $^{171}\text{Yb}$

In contrast to  $^{174}\text{Yb}$ ,  $^{171}\text{Yb}$  has a non-zero nuclear spin of  $I = 1/2$ . The absence of hyperfine coupling in low-lying  $J = 0$  manifolds (i.e.,  $^1S_0$  or  $^3P_0$ ) results in an ideal nuclear spin qubit [30, 31, 63]. Counterintuitively, the Rydberg states of  $^{171}\text{Yb}$  have a fairly strong hyperfine coupling, which arises from the interplay of hyperfine coupling in the  $\text{Yb}^+$  core and the exchange interaction between the core and Rydberg electrons. This coupling is necessary to implement entangling gate operations on the pure nuclear spin qubit [31, 40], but also significantly complicates the description of the Rydberg series [51, 71–73]. We note that the role of hyperfine coupling in  $^{171}\text{Yb}$  qubits is almost opposite to alkali atoms, where the ground state has strong hyperfine coupling, while direct hyperfine coupling of the Rydberg state can be largely neglected [74].

In the context of MQDT, hyperfine effects can be rep-

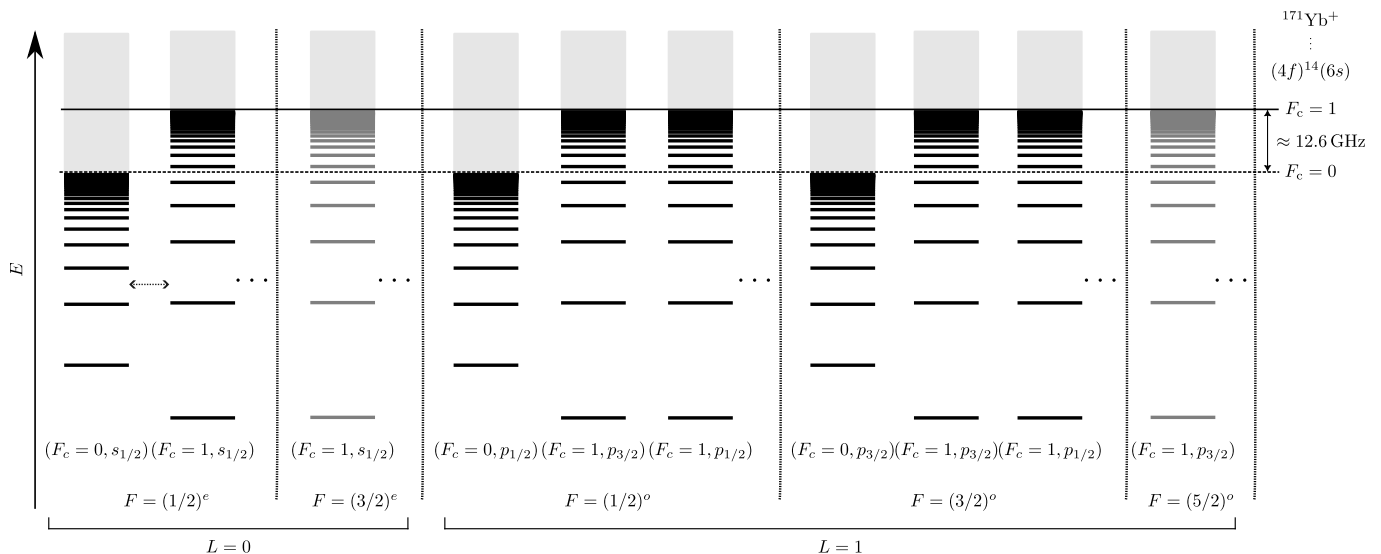


Figure 2. Schematic energy level diagram of the  $L = 0$  and  $L = 1$  Rydberg states of  $^{171}\text{Yb}$ , indicating Rydberg series converging to the two hyperfine states of the  $^{171}\text{Yb}^+$  ground state. Channels converging to electronically excited states of the ion core are not shown, but are included in the MQDT models. The series are labeled by their good quantum numbers  $F$  and parity (denoted by superscript  $e$ , for even, and  $o$  for odd).

resented as a coupling between multiple Rydberg series with the same parity and total angular momentum  $F$ , converging to different thresholds corresponding to the hyperfine-split ion core states (Fig. 2). In the case of  $^{171}\text{Yb}^+$ , the  $6s^2S_{1/2}$  ground state is split into two hyperfine states with total angular momentum  $F_c = 0$  and  $F_c = 1$ , separated by  $A_{HF} = 12.642812$  GHz [75]. For the range of  $\nu$  relevant for quantum information applications ( $40 \lesssim \nu \lesssim 100$ ), the hyperfine interaction energy is comparable to the spacing between principal quantum levels, resulting in strong channel mixing when there is more than one series with the same  $F$  and parity [76]. For example, the  $6sns$  states in  $^{171}\text{Yb}$  give rise to two coupled  $F = 1/2$  series converging to  $F_c = 0$  and  $F_c = 1$ , and a single  $F = 3/2$  series converging to the  $F_c = 1$  threshold.

The effect of hyperfine-induced channel mixing has been experimentally studied previously in several species, including  $^{87}\text{Sr}$  [51, 72, 77, 78] and  $^{135,137}\text{Ba}$  [47, 79]. However, only a small number of measurements of  $^{171}\text{Yb}$  Rydberg states have been reported [31, 80–82].

### A. $L = 0$ states

There are three Rydberg series with  $L = 0$  in  $^{171}\text{Yb}$  (Fig. 2). At low  $\nu$ , where hyperfine coupling is a small perturbation compared to the singlet-triplet splitting, these series are described in the  $LS$  basis as a single  $^1S_0$  series with  $F = 1/2$ , and two  $^3S_1$  series with  $F = \{1/2, 3/2\}$ . Very close to the threshold,  $jj$ -coupling is more appropriate: one  $F = 1/2$  series results from adding the outer electron spin ( $s = 1/2$ ) to the  $F_c = 0$  ion core, while the other  $F = 1/2$  and  $F = 3/2$  series are

connected to  $F_c = 1$ . While these descriptions are equivalent for the  $F = 3/2$  series, the  $F = 1/2$  eigenstates cannot be simply described in either basis in between these limits, necessitating an MQDT model for these states.

We have experimentally measured the energy of most  $L = 0$   $F = 1/2$  states with  $25 < \nu < 120$  using laser spectroscopy as described in Appendix B. The measured  $L = 0$  Rydberg state energies and associated MQDT model predictions are shown in Fig. 3a. The agreement is excellent: the  $F = 1/2$  states have a root-mean-squared deviation of 2.3 MHz from the model, consistent with the  $3\sigma$  uncertainty of 10 MHz of the wavelength meter used to determine the laser frequencies.

In analogy to the Stark shift measurements for  $^{174}\text{Yb}$  in Fig. 1c and d, we test the wavefunctions by comparing the measured and predicted magnetic moments of a subset of states, shown in Fig. 3c. For low  $\nu$ , the magnetic moments are close to the Landé  $g$ -factors for  $LS$ -coupled states, but they deviate significantly above  $\nu = 40$ .

The primary characteristic of the  $F = 1/2$  series is the avoided crossings in the energy spectrum. These can be understood from the channel structure of Fig. 2: strong channel mixing and level repulsion occur when the separation between Rydberg levels is comparable to the ion core hyperfine splitting. For  $^{171}\text{Yb}$ , the  $\Delta n = 1, 2$  and 3 level crossings occur at  $\nu \approx 80, 100$  and 115, respectively, though we note that the wavefunction character is already affected far below the first avoided crossing at  $\nu = 80$ . The physical mechanism for this mixing is the exchange interaction between the inner and outer electrons.

The coloring of the curves in Fig. 3 is a guide to the eye. The transition from  $LS$ - to  $jj$ -coupled states makes it challenging to introduce an unambiguous partition of

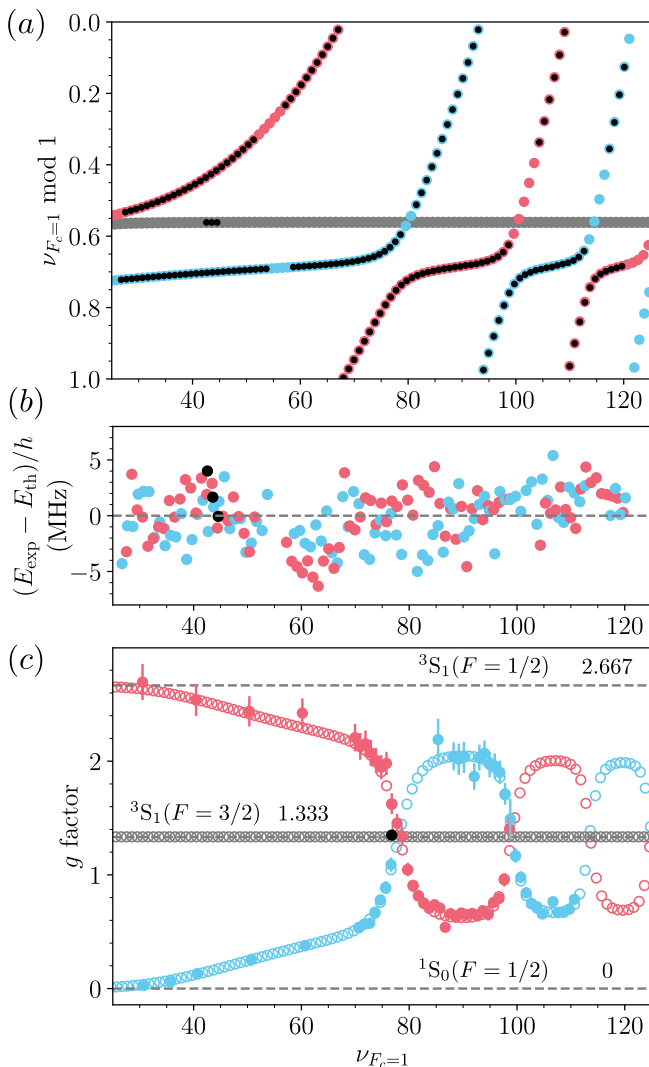


Figure 3. (a) Lu-Fano-type plot of  $^{171}\text{Yb}$   $|\nu, L=0, F=1/2\rangle$  Rydberg states (red, blue) and  $|\nu, L=0, F=3/2\rangle$  states (gray). The black points correspond to experimentally observed states, whereas the colored points denote bound states in the MQDT model. For  $\nu < 70$ , we refer to the red states as “triplet connected” and the blue states as “singlet connected” based on their dominant character in  $LS$  coupling. This description breaks down at higher principal quantum numbers. (b) Deviation between measured and modeled bound state energies (red and blue for  $F=1/2$  and black for  $F=3/2$ ). (c) Measured (filled circles, color code as in (b)) and predicted (empty circles)  $g$ -factors. The gray dashed lines indicate the Landé  $g$  factors in pure  $LS$  coupling.

all of the  $F=1/2$  states into two series. Throughout this paper, we identify specific states by  $F, l$  and the effective principal quantum number  $\nu$  specified to two decimal places, (*e.g.*,  $|\nu = 54.28, L=0, F=1/2, m_F=1/2\rangle$ ). In this description,  $L$  is the Rydberg electron angular momentum in the  $6snl$  channels. In the specific case of the  $F=1/2$  S states, we also find it convenient to refer to the states with  $\nu < 70$  as being “triplet-connected” or

“singlet-connected” based on their dominant character in  $LS$  coupling.

Hyperfine coupling does not affect the  $F=3/2$  series, which follows the same behavior as the  $^3S_1$  series in  $^{174}\text{Yb}$ , converging to the  $F_c=1$  ionization limit. We have measured the energies of several  $F=3/2$  states to confirm this behavior (Fig. 3a).

The MQDT model parameters, tables of measured energy levels for  $S F=1/2$  and  $S F=3/2$ , as well as Landé  $g$  factors and values of DC polarizabilities of  $S F=1/2$  Rydberg states are presented in the supplemental material [70].

## B. $L=1$ states

There are seven  $L=1$  series in  $^{171}\text{Yb}$ . In  $LS$  coupling, they can be described as  $^3P_0(F=1/2)$ ,  $^1P_1(F=\{1/2, 3/2\})$ ,  $^3P_1(F=\{1/2, 3/2\})$  and  $^3P_2(F=\{3/2, 5/2\})$ . In  $^{174}\text{Yb}$ , spin-orbit coupling mixes the two  $J=1$  series as discussed in Section II; in  $^{171}\text{Yb}$ , hyperfine coupling additionally mixes the three  $F=1/2$  series and the three  $F=3/2$  series (Fig. 2).

We have experimentally measured the energies of a number of  $|\nu, L=1, F=1/2\rangle$  and  $|\nu, L=1, F=3/2\rangle$  states, using microwave transitions from  $|\nu, L=0, F=1/2\rangle$  states (for details, refer to Appendix B). The results are shown in Fig. 4, along with previously published measurements of low- $\nu$  states from three-photon laser spectroscopy [81, 82].

As in the case of the  $|\nu, L=0, F=1/2\rangle$  series, we begin with the  $^{174}\text{Yb}$  MQDT models of  $^{1,3}P_1$  and  $^3P_0$  (for  $F=1/2$ ) and  $^{1,3}P_1$  and  $^3P_2$  (for  $F=3/2$ ) presented in Appendix D and refine the model by a global fit to the observed state energies of the  $|\nu, L=1, F=1/2\rangle$  and  $|\nu, L=1, F=3/2\rangle$  Rydberg states. A comparison of the experimental state energies and the MQDT model energies is presented in Lu-Fano-type plots in Fig. 4(a) and (b) for  $F=1/2$  and  $F=3/2$ , respectively.

The behavior of the  $L=1$  states is considerably more complex than the  $L=0$  states, because the hyperfine coupling acts on states that were already strongly perturbed in  $^{174}\text{Yb}$ .

We observe systematic deviations between the experimental and modeled energies. The high accuracy of the microwave measurements (100 kHz) makes it clear that the deviations are systematic as opposed to random. Particularly, the dispersion-like feature in the fit residuals observed near  $\nu \approx 43$  for  $F=3/2$  suggests the existence of an additional perturbing Rydberg series. The perturbing Rydberg state could come from unaccounted hyperfine splitting of excited states of the ion core, or from interactions with odd-parity  $L=3$  Rydberg channels. Based on DC polarizabilities of the measured P Rydberg states with  $\nu < 70$  and our ability to resolve Rydberg states with much larger DC polarizability, we conclude that the observed systematic deviations are not due to uncompensated stray electric fields. The significant de-

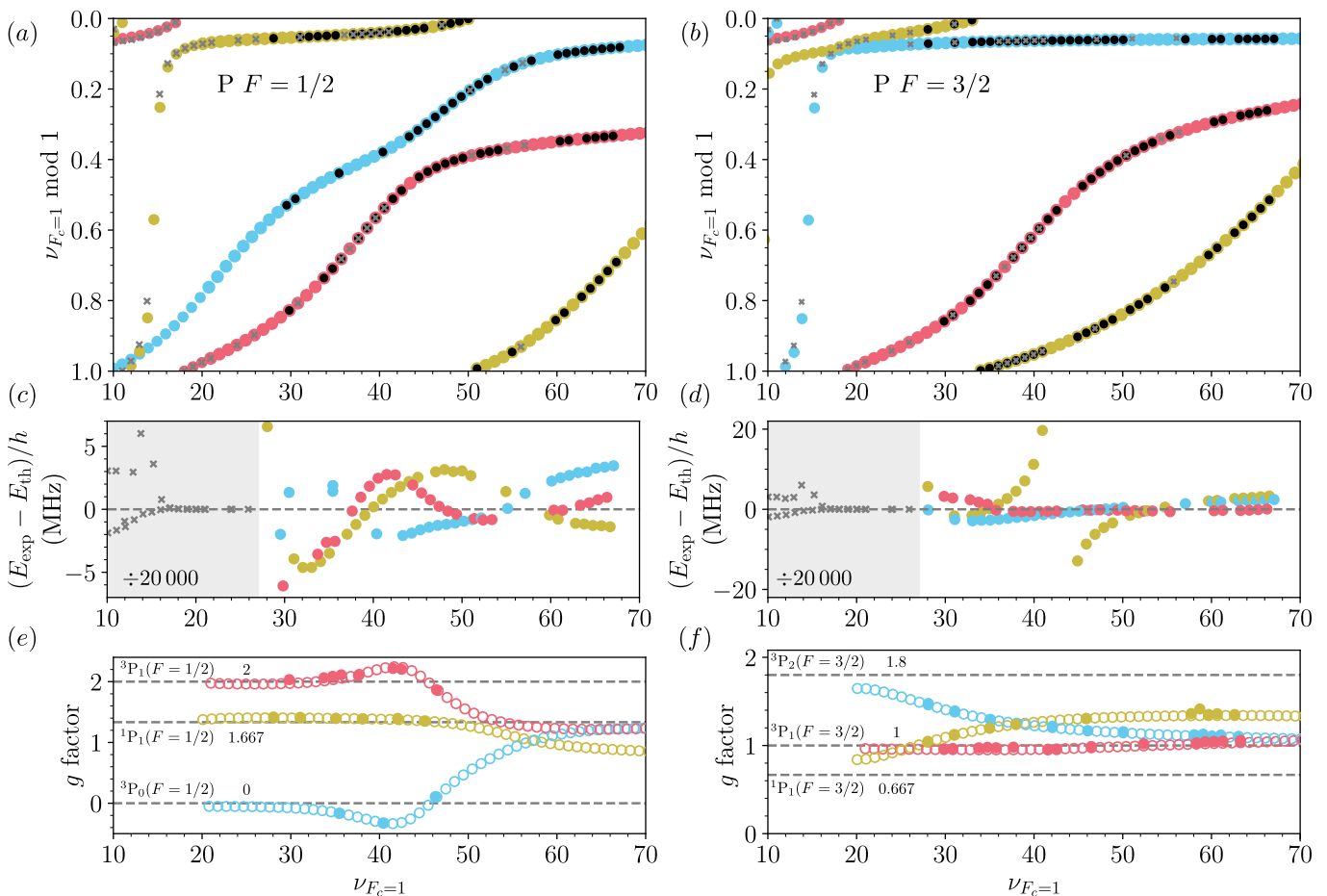


Figure 4. (a) and (b) Lu-Fano-type plot of  $^{171}\text{Yb}$   $|\nu, L = 1, F = 1/2\rangle$  and  $|\nu, L = 1, F = 3/2\rangle$  Rydberg states, respectively. The black points correspond to experimentally observed states by microwave spectroscopy, as described in Appendix B. The gray crosses are three-photon laser spectroscopy data from Ref. [82]. The colored points denote the MQDT model bound states (the colors are chosen to guide the eye). (c) and (d) Deviation between measured and modeled bound state energies. The deviations of the laser spectroscopy measurements are divided by a factor of 20 000, and are not shown for states that were also observed by microwave spectroscopy. (e) and (f) Measured (filled circles) and predicted (empty circles)  $g$ -factors. The gray dashed lines indicate the Landé  $g$  factors in pure  $LS$  coupling.

viations for states with  $\nu < 16$  suggest an additional perturber in that energy range, as well.

To confirm the accuracy of the MQDT wavefunctions, we also compare the predicted magnetic moments to experimental measurements (Figs. 4 (e) and (f)). As with the  $L = 0$  series, the moments align with the Landé  $g$ -factors for  $LS$  coupling at low principal quantum number, and deviate significantly at large  $\nu$  because of the combination of singlet-triplet mixing and hyperfine interaction.

We have not directly measured any  $^{171}\text{Yb}$   $L = 1$ ,  $F = 5/2$  states. In  $LS$  coupling, this series can be described as  $^3P_2(F = 5/2)$  converging to the upper  $F_c = 1$  hyperfine threshold. We therefore model this series using the MQDT model for the  $^3P_2$  series presented for  $^{174}\text{Yb}$  in the previous section. To account for isotope dependent effects, we use the MQDT model parameters as optimized from a fit to the observed  $|\nu, L = 1, F = 3/2\rangle$  Rydberg states, which contain a contribution from the  $^3P_2(F = 3/2)$  states.

A summary of all measured  $L = 1$  state energies, Landé  $g$  factors, and MQDT model parameters are presented in the supplemental material [70].

### C. Verification of MQDT models with Stark shifts

As with  $^{174}\text{Yb}$ , we probe the accuracy of Rydberg state energies and matrix elements obtained from our MQDT models by measuring the dc Stark shift of  $|\nu, L = 0, F = 1/2\rangle$  states near degeneracies with  $|\nu, L = 1, F = 1/2\rangle$  and  $|\nu, L = 1, F = 3/2\rangle$  Rydberg states (Fig. 5a). The measured Stark shifts are in excellent agreement with the theoretical predictions (Fig. 5b–e), indicating good MQDT models for all relevant states, producing both accurate energies and channel contributions. Certain states with near-degenerate opposite parity states do not have quadratic Stark shifts even at very small electric fields, so we make the compari-

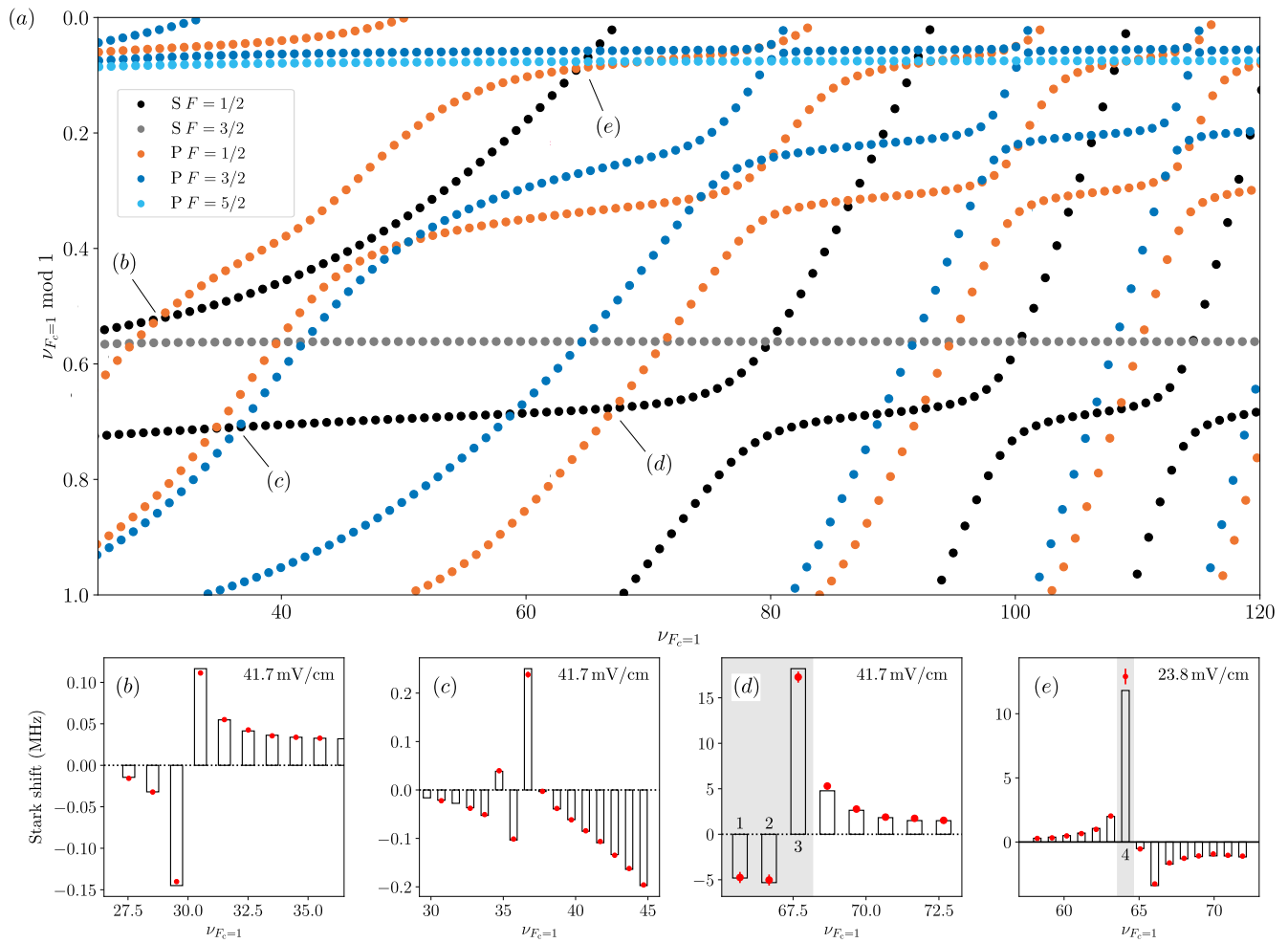


Figure 5. (a) Combined plot summarizing the MQDT model energies for all  $L = 0$  and  $L = 1$  Rydberg series in  $^{171}\text{Yb}$ . (b–e) Measured (red) and predicted (black bars) Stark shifts of selected  $L = 0$   $F = 1/2$  series in the vicinity of crossings with  $L = 1$  Rydberg series, at locations indicated by markers in panel (a). The Stark shift is reported at the electric field strength indicated in each panel. The gray shaded states correspond to near-degeneracies with significantly non-quadratic Stark shifts. A detailed comparison of the shifts of these states to a non-perturbative model is shown in Fig. 17.

son between experiment and theory using the magnitude of the Stark shift at a particular field, instead of the usual static dipole polarizability. For these states, we also compare the measured field-dependent Stark shift with a non-perturbative calculation, and find excellent agreement (Fig. 17 in App. E1). The experimentally determined static dipole polarizabilities and Stark shifts are presented in the supplemental material [70]. Predicted polarizability trends of the  $L = 0$  Rydberg states of both  $^{171}\text{Yb}$  and  $^{174}\text{Yb}$  Rydberg states are presented in Appendix F.

#### IV. RYDBERG-RYDBERG INTERACTIONS IN $^{171}\text{Yb}$

A precise understanding of the interaction potential is important to realize high-fidelity gate operations. In this

section, we use the developed MQDT model to predict the interaction potential for a pair of  $^{171}\text{Yb}$  atoms, then validate the model using direct experimental measurements in an optical tweezer array. The calculation builds on established techniques for performing similar calculations in alkali atoms, based on numerically diagonalizing the multipolar interaction Hamiltonian in a large basis of pair states [83, 84]. In the context of alkali atoms, this approach has been experimentally validated by spectroscopic measurements in optical tweezers [15, 16] and optical lattices [24]. We follow the formalism extending these techniques to states described by MQDT that was introduced previously in Refs. [44, 52].

We first consider the interaction potential between a pair of atoms in a  $|\nu, L = 0, F = 1/2, m_F\rangle$  state. For concreteness, we focus on the triplet-connected  $|\nu_{4,28}, L = 0, F = 1/2, m_F\rangle$  states. The calculated pair potentials for the four combinations of  $m_F$  sublevels is

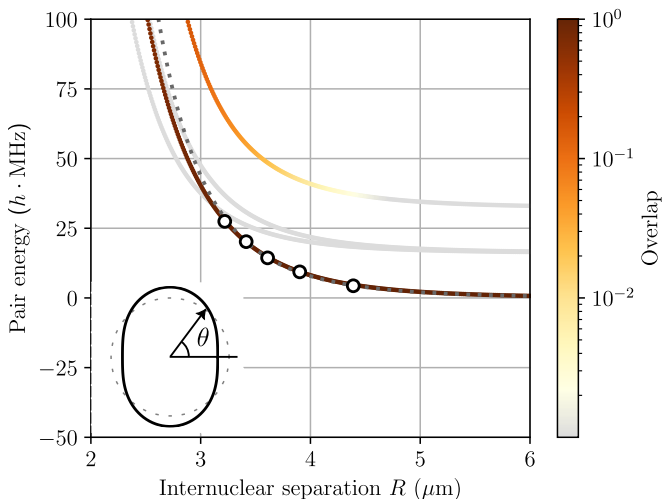


Figure 6. Predicted pair-interaction potentials for a target Rydberg state  $|t\rangle = |54.28, L=0, F=1/2, m_F=-1/2\rangle$ , together with measured energy shifts (white circles). The magnetic field strength is  $4.88(6)$  G, corresponding to a Zeeman splitting of  $16.1$  MHz, and is oriented at  $\theta = \pi/2$  to the inter-atomic axis. The color of the curves denotes the overlap of each eigenstate with the target pair state  $|t\rangle^{\otimes 2}$ . The gray, dashed line shows the asymptotic  $1/R^6$  scaling. *Inset*: predicted angle-dependence of the  $C_6$  coefficient.  $\theta$  is the angle between the magnetic field and the inter-atomic axis.

shown in Fig. 6. The predicted pair potential closely follows the expected van der Waals form  $V(R) = C_6/R^6$ , with  $C_6 \approx h \cdot 34 \text{ GHz}(\mu\text{m})^6$ . For comparison, we note that the  $C_6$  coefficient for the Rb  $nS_{1/2}$  state with the most similar  $\nu$  ( $n=57$ ) is  $C_6 \approx h \cdot 76 \text{ GHz}(\mu\text{m})^6$  [84].

We test the theoretical prediction by directly measuring the van der Waals shift using a pair of atoms in optical tweezers with separations from  $3.3$ – $4.5 \mu\text{m}$ . The measured energy shift is in excellent agreement with the predicted pair potential after scaling the experimental interatomic separation by a factor of  $0.97$  relative to the predicted separation (Fig. 6), which we attribute to imperfect focusing of the optical system used to project the tweezer array. Additional details about the measurement technique are described in Appendix C.

We note that there is a nearby  $F=3/2$   $D$  state with a detuning of only  $68$  MHz at zero magnetic field. As this state is also laser-accessible from  $^3P_0$ , it could cause problems for blockade gates if its van der Waals interaction has the opposite sign from the target state, pushing it into resonance. We are unable to predict the  $D$  state interactions, because we do not yet have an MQDT model for the  $F$  states. However, we note that this problem can be avoided by using the next lowest triplet-connected  $S$  state with  $\nu = 53.30$ , where the nearest  $D$  state is detuned by more than  $600$  MHz.

The predicted interaction strength is anisotropic, where the  $C_6$  coefficient is approximately  $46\%$  larger when the internuclear axis is aligned perpendicular to the magnetic field compared to a parallel alignment to

the magnetic field (Fig. 6, inset). In contrast, the van der Waals interaction between alkali atoms in  $S$  states is usually highly isotropic, because of the small spin-orbit coupling in the  $P$  states participating in the interaction [85]. For example, the  $C_6$  coefficient for the  $50^2S_{1/2}$  state in Rb has an anisotropy of approximately  $1\%$ . The large anisotropy in this  $^{171}\text{Yb}$  state is attributed to the large spin-orbit coupling in Yb (scaling as  $Z^4$ ), and series perturbations that lift the degeneracy between  $J$  manifolds (as shown in Fig. 1b for the  $^{174}\text{Yb}$   $P$  series), which has the same effect as spin-orbit coupling. The anisotropy also results in off-diagonal  $C_6$  interactions that mix different  $m_F$  levels. As seen from the color scale in Fig. 6, the  $|m_F=1/2, m_F=1/2\rangle$  state acquires a significant  $|m_F=-1/2, m_F=-1/2\rangle$  character once the van der Waals shift becomes comparable to the Zeeman splitting. This effect is suppressed if the interatomic spacing is parallel to the magnetic field, as a consequence of the dipole-dipole selection rules [85].

We have computed the  $C_6$  coefficient for all of the  $F=1/2$  series, and summarized the results in Fig. 22. The  $C_6$  coefficient for the triplet-connected  $F=1/2$  series follows the expected  $\nu^{11}$  scaling in the range  $\nu \lesssim 65$ . The singlet-connected  $F=1/2$  series has a much smaller  $C_6$  coefficient in this range, with the exception of isolated states with accidental hyperfine-induced Förster resonances. This is consistent with previous estimates of a small  $C_6$  for the  $^{174}\text{Yb } ^1S_0$  series using a single-channel approximation [86].

Next, we consider an  $F=3/2$  target state. Specifically, we consider the state  $|54.56, L=0, F=3/2, m_F=+3/2\rangle$ , which was used to implement two-qubit gates in Ref. [40]. The computed pair potential is shown in Fig. 7a. Unlike the  $F=1/2$  state shown in Fig. 6, the pair potential for this  $F=3/2$  state deviates strongly from the idealized  $C_6/R^6$  van der Waals scaling, because of a previously unknown Förster resonance with a pair state made up of  $L=1$  states with  $F=3/2$  and  $F=5/2$ . At zero magnetic field, this pair state is detuned by only approximately  $3$  MHz from the  $|54.56, L=0, F=3/2\rangle^{\otimes 2}$  pair state. The complex series of crossings results from different magnetic sublevels being pushed into exact resonance by the interaction, in a finite magnetic field of  $B \approx 5$  G. Similar behavior is observed for the  $m_F=-3/2$  states, though the resulting spectrum is slightly less complex as the Zeeman shift has the same sign as the van der Waals interaction.

We have also experimentally measured the interaction shifts for this state. We are able to identify all pair states from this complex spectrum with an overlap of more than  $10\%$  with the target state, and find good agreement for both  $m_F=+3/2$  and  $m_F=-3/2$  using the same rescaling factor of the interatomic separation ( $0.97$ ) used in Fig. 6. In the case of  $m_F=+3/2$ , we observe deviations of  $1$ – $2$  MHz for one of the eigenstates. This is comparable in magnitude to the fit residuals in the  $F=3/2$   $P$  series MQDT model (Fig. 4; the  $F=3/2$  state that contributes to the Förster resonance is in the blue-colored series in

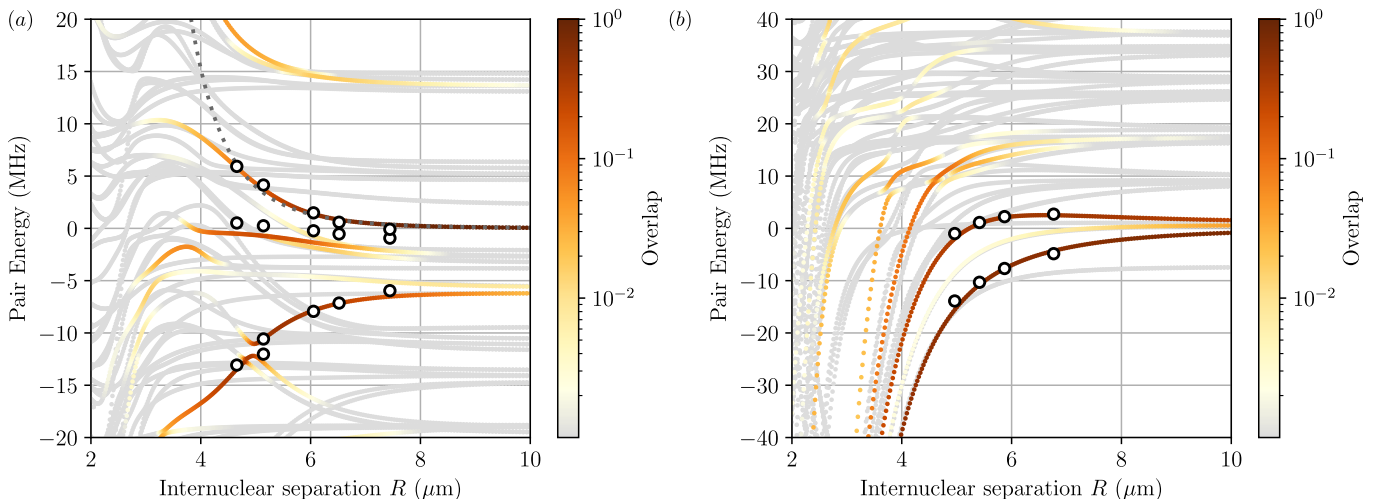


Figure 7. Predicted pair-interaction potentials for a target state  $|54.56, L=0, F=3/2, m_F\rangle$  with (a)  $m_F = 3/2$  and (b)  $m_F = -3/2$ , at a magnetic field of 5.03(6) G ( $\theta = \pi/2$ ). The color of the curves denotes the overlap with the target pair state. The white circles indicate experimentally observed resonances as described in the text. The gray dashed line in panel (a) shows the asymptotic  $1/R^6$  scaling.

that figure).

A quantitative analysis of Rydberg interaction strengths of  $S F = 1/2$  and  $S F = 3/2$  Rydberg states is presented in App. G.

## V. IMPROVED TWO-QUBIT GATES

The Förster resonance observed for the  $|54.56, L=0, F=3/2\rangle$  state is not accidental, but rather a systematic trend: almost all  $|\nu, L=0, F=3/2\rangle$  states with  $\nu > 30$  have a Förster defect less than 10 MHz (Fig. 23). While Förster resonances are sometimes sought to increase the strength of the Rydberg-Rydberg interaction at long range [87, 88], such a near-degenerate resonance is problematic for two-qubit gates because it results in a large number of weakly allowed transitions near zero energy at short separations, allowing Rydberg excitation within the blockade radius [89]. This effect is sometimes referred to as *Rydberg spaghetti*. At the same time, Förster resonances increase the long-range tail of the interactions, preventing parallel implementation of gates in a qubit array [90]. Understanding the existence of this Förster resonance resolves several observations from Ref. [40], including an unknown contribution to the error budget of about 1%, and the need to use a large separation ( $43 \mu\text{m}$ ) between adjacent dimers to achieve the highest gate fidelity.

We now demonstrate improved gate performance using the  $|54.28, L=0, F=1/2\rangle$  state. Previous demonstrations of entangling gates in  $^{171}\text{Yb}$  used  $F=3/2$  states [31, 40]. The highest reported fidelity is  $\mathcal{F} = 0.980(1)$ , which is approximately 1% lower than the predicted fidelity of  $\mathcal{F} = 0.989$  based on error sources that were understood at the time [40]. We conjecture the

additional errors were the result of unwanted Rydberg excitation to nearby pair states (Fig. 7), and that the  $F=1/2$  state with a cleaner interaction potential will lead to higher fidelity.

We implement a two-qubit gate using the same approach as Ref. [40]. Briefly, we prepare an array of four pairs of atoms (with a spacing of  $d = 2.4 \mu\text{m}$  between atoms within a pair, and  $D = 24 \mu\text{m}$  between pairs) and implement CZ gates in parallel using a variant of the time-optimal two-qubit gate [91]. The gate is driven using a UV laser at 302 nm, with a power of 20 mW in a beam with a  $1/e^2$  radius of  $12 \mu\text{m}$  to achieve a Rabi frequency of  $\Omega = 2\pi \times 2.5$  MHz between  $^3P_0$   $m_F = +1/2$  and Rydberg state with  $m_F = -1/2$ . Because of geometric constraints, the laser is linearly polarized perpendicular to the magnetic field, such that only half of the power contributes to the  $\sigma^-$  transition that drives the gate. We estimate the fidelity using the randomized circuit characterization approach of Ref. [40, 92], with interleaved global single-qubit gates. With these parameters, we observe a CZ gate fidelity of  $\mathcal{F} = 0.994(1)$  (Fig. 8).

The randomized circuit characterization involves varying the number of two-qubit gates  $d$  while keeping the number of single-qubit gates and the overall sequence duration constant. This approach allows us to isolate errors specific to two-qubit operations from other sources of error in the circuit. Each randomized circuit is designed to bring the system to the final state  $|00\rangle$ . As a function of the circuit depth  $d$ , we experimentally characterize the success rate  $P_{00}$  of the circuit. The experimental success rates are fitted to an exponential decay model  $P_{00} = A(1 - \epsilon)^d$ . Only two-qubit gate errors will contribute to  $\epsilon$ , while the offset at zero circuit depth  $A \approx 0.87$  captures other sources of error in the circuit, including state preparation and measurement errors, and

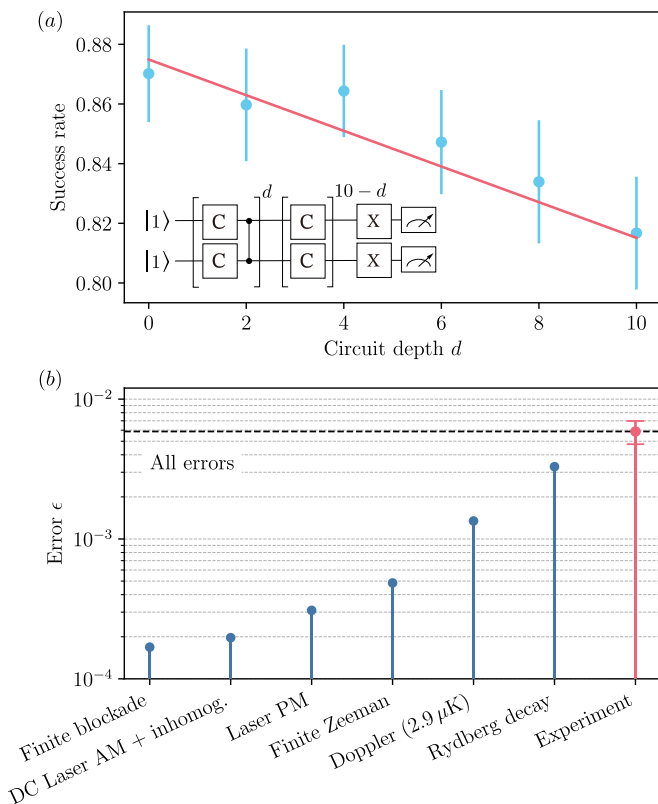


Figure 8. (a) Randomized circuit characterization of the time-optimal CZ gate, using a variable depth  $d$ . The fitted error rate is  $\epsilon = 5.6(1.1) \times 10^{-3}$  per two-qubit gate. (b) Numerical simulation of contributions to the gate error, including the finite Rydberg state lifetime, Doppler shifts from atomic motion, off-resonant excitation of neighbouring  $m_F$  sublevels in finite magnetic fields, shot-to-shot and site-to-site laser amplitude variations, finite Rydberg blockade, and fast laser phase noise (PM). The total simulated error rate with all sources applied simultaneously is  $\epsilon = 5.9 \times 10^{-3}$  (black dashed line), in good agreement with the experimentally measured error rate (red point).

single-qubit gate errors [40, 92, 93].

This result improves on the previous best gate in  $^{171}\text{Yb}$  by a factor of 3.3. Importantly, the error budget for the gate in Fig. 8a is now in excellent agreement with a model based on independently measured sources of error (Fig. 8b) [40]. The dominant contributions are the finite lifetime of the Rydberg state (measured to be  $T_r = 56(4) \mu\text{s}$ , contributing an error of  $\epsilon = 3.3 \times 10^{-3}$ ) and Doppler shifts ( $\epsilon = 1.4 \times 10^{-3}$  at an atomic temperature during the gate of  $T = 2.9 \mu\text{K}$ ). We also estimate the impact of other sources of error, including unwanted excitation of the other  $m_F$  sublevel of the Rydberg state ( $\epsilon = 4.8 \times 10^{-4}$ ), site-to-site and shot-to-shot laser intensity variation ( $\epsilon = 2.0 \times 10^{-4}$ ), a finite Rydberg blockade strength ( $\epsilon = 1.7 \times 10^{-4}$ ; the pulse is not compensated for the finite blockade [90, 91]), and fast laser phase noise ( $\epsilon_{\text{PM}} = 3.1 \times 10^{-4}$ ). Since the dominant errors can be suppressed by increasing the gate speed (*i.e.*, with ad-

ditional laser power), these results suggest that significantly higher gate fidelities are within reach for  $^{171}\text{Yb}$ .

## VI. DISCUSSION AND CONCLUSION

We have presented detailed spectroscopy and modeling of the Rydberg states of both  $^{174}\text{Yb}$  and  $^{171}\text{Yb}$  with  $L \leq 2$ . The models are validated with experimental measurements of Stark shifts, magnetic moments and Rydberg interactions. To the best of our knowledge, this is the most comprehensive validation of an MQDT model for a complex atom, and allows key properties for Rydberg atom quantum computing and simulation to be predicted with the level of accuracy that is routine for alkali atoms. This will provide vital input for future experiments in quantum computing and simulation with Yb, or with Yb-alkali mixtures. Moreover, the calculation technique is a template for exploring other atoms in the lanthanide group, such as Ho or Er [64, 65].

We used this model to identify the likely cause of previously unattributed errors in entangling gates using  $F = 3/2$  Rydberg states. We also predicted a more suitable Rydberg state with  $F = 1/2$ , leading to an improved gate fidelity of  $\mathcal{F} = 0.994(1)$ , with errors reduced by a factor of 3.3 compared to the previous best gate demonstration using  $^{171}\text{Yb}$  [40].

We identify several avenues for future work. The first is including states with  $L \geq 3$ , which are needed to accurately predict the interactions of  $D$  states, which can create blockade violations for  $S$  states. The second is to extend the model to predict Rydberg state lifetimes and decay branching ratios, which will involve more careful fitting of MQDT models to low- $n$  perturbers and including matrix elements between different core electron states [43]. While low- $n$  perturbers have little effect on the Rydberg character of high- $n$  states, they can have a large impact on the lifetime and decay branching ratio by providing a new decay pathway via the population of the perturbing state [20, 43].

Another area of interest is the behavior of autoionizing states, of the form  $6p_{1/2}nl$ . These states have found use for Rydberg atom detection [94, 95], coherent control [96, 97] and in quantum error correction [39]. To our knowledge, only the  $^{174}\text{Yb } ^3S_1$  autoionizing series has been characterized [96]. A systematic study, including  $^{171}\text{Yb}$ , would be beneficial for applications relying on use of these states.

Finally, we note that these models may have applications beyond quantum computing. Ytterbium clocks are among the most precise in the world [98], and Rydberg states can be used for generating entanglement to enhance precision [35, 36]. It has also been proposed to use Rydberg states for *in situ* absolute calibration of the temperature through the blackbody radiation spectrum [99], which would warrant more precise validation of the modeled matrix elements.

## ACKNOWLEDGMENTS

We gratefully acknowledge helpful conversations with Adam Kaufman and Aruku Senoo, and Prof. Herbert Rinneberg for providing a copy of Ref. [82]. This work was supported by the Army Research Office (W911NF-1810215), the Office of Naval Research (N00014-20-1-2426), DARPA ONISQ (W911NF-20-10021), the National Science Foundation (QLCI grant OMA-2120757, and NSF CAREER PHY-2047620), the Sloan Foundation and the Gordon and Betty Moore Foundation (Grant DOI 10.37807/gbmf12253).

## Appendix A: MQDT formalism

Energies and wavefunctions of Rydberg states are crucial for evaluating state properties (*e.g.*, Stark shifts [12]). Several open-source programs have been developed for non-perturbative calculations of Stark shifts and interaction potentials for alkali metal atoms [83, 84], or alkaline earth atoms within a single channel quantum defect approximation [45]. However, for divalent atoms, a multichannel quantum defect theory (MQDT) treatment is necessary to obtain accurate Rydberg state energies and wavefunctions.

MQDT was introduced by Seaton [41] and reformulated with the concept of frame transformations by Fano [42] and is established as a powerful framework for analyzing the Rydberg states of atoms [43, 62, 64, 65, 73, 79, 100–106] and molecules [42, 107, 108] with low-lying core-excited states.

Calculations based on MQDT models predicting DC polarizabilities and Rydberg-Rydberg interaction for complex atoms have been presented previously [44, 52, 68], but the conceptual complexity and lack of comprehensive MQDT characterization of atomic species has limited the broad adoption of this approach.

This appendix is intended to serve as a comprehensive introduction and overview to this approach, which will be useful beyond the specific case of Yb atoms. We have also made the software used to perform the computations in this work available as an open-source package, `rydcalc` [109].

### 1. MQDT model

MQDT treats the short and long-range interactions of a single active electron with different configurations of the ion core. Each unique combination of angular quantum numbers of the electron-ion-core system is referred to as a channel. When the active electron is far away from the ion core, the system is well described by “collision” channels indexed by  $i$ . In this region, the interaction between the ion core and the active electron is dominated by the Coulomb interaction and the system is appropriately described in  $jj$ -coupling.

The energy  $E$  can be expressed with respect to the ionization limit of the  $i^{\text{th}}$  collision channel  $I_i$  as

$$E = I_i - (hcR_M)/\nu_i^2 \quad (\text{A1})$$

where  $\nu_i$  is the effective principal quantum number with respect to  $I_i$  and  $R_M = R_\infty(1 - m_e/M)$  is the mass-reduced Rydberg constant, where  $m_e$  is the mass of the electron and  $M$  is the atomic mass.

When the active electron is close to the ion core, their interaction is dominated by non-Coulombic electrostatic interactions. Channels describing the angular momentum coupling (typically  $LS$  coupling) in this regime more appropriately are called “close-coupling” channels indexed by  $\alpha$ . In this region, scattering between the electron and the ion core mixes  $i$  channels with the same total angular momentum  $J$  (or  $F$  in the presence of a non-zero nuclear spin) and parity. The wavefunction of channel  $i$  can therefore be expressed as a superposition of  $\alpha$  channel wavefunctions with amplitude  $\tilde{A}_\alpha$ . At large electron-ion-core separations, the wavefunction at energy  $E$  can be written as [62]

$$|\Psi\rangle = \sum_i |\Phi_i\rangle \left[ f(\nu_i, r) \sum_\alpha U_{i\alpha} \cos(\pi\mu_\alpha) \tilde{A}_\alpha - g(\nu_i, r) \sum_\alpha U_{i\alpha} \sin(\pi\mu_\alpha) \tilde{A}_\alpha \right], \quad (\text{A2})$$

where the terms in the square brackets correspond to the radial part of the active electron’s wavefunction, and the spin and orbital angular momentum couplings of the outer electron and the ion core wavefunction are given by  $|\Phi_i\rangle$ .  $f(\nu_i, r)$  and  $g(\nu_i, r)$  correspond to the regular and irregular Coulomb wavefunctions [42]. The short-range, non-Coulombic interaction of the Rydberg electron and the ion core are encoded in eigenchannel quantum defects  $\mu_\alpha$  and the channels are coupled by the unitary transformation matrix  $U_{i\alpha}$ .

For discrete bound states, the wavefunction Eq. (A2) must remain finite at large separation, resulting in the boundary condition [42, 62]:

$$\sum_\alpha \tilde{A}_\alpha U_{i\alpha} \sin[\pi(\nu_i + \mu_\alpha)] = 0 \quad (\text{A3})$$

This gives non-trivial solutions for the bound state energies  $\nu_i$  when  $\det |F_{i\alpha}| = 0$  is zero, where  $F_{i\alpha}$  is given by:

$$F_{i\alpha} = U_{i\alpha} \sin[\pi(\mu_\alpha + \nu_i)]. \quad (\text{A4})$$

Bound states are found at the intersection of the surface spanned by Eq. (A4) and the curve:

$$\nu_i = \left( \frac{I_i - I_j}{R_M} + \frac{1}{\nu_j^2} \right)^{-1/2}, \quad (\text{A5})$$

where  $\nu_i$  and  $\nu_j$  are effective principal quantum numbers relative to the  $i^{\text{th}}$  and  $j^{\text{th}}$  ionization limit  $I_i$  and  $I_j$ , respectively.

The MQDT model is fully specified by the unitary transformation matrix  $U_{i\alpha}$  and the eigenchannel quantum defects  $\mu_\alpha$ . The task in determining accurate MQDT models therefore reduces to finding values of  $U_{i\alpha}$  and  $\mu_\alpha$ , which reproduce experimental observables such as state energies, Landé  $g$ -factors or DC polarizabilities.

## 2. MQDT model parameters

The transformation matrix  $U_{i\alpha}$  is orthogonal and can therefore be constructed from at most  $N(N-1)/2$  rotation matrices, in the case of an  $N$  channel model [100]. In practice, the mixing between channels is small and a suitable approximation can be made by composing significantly fewer rotation matrices. As noted above, the natural basis at long range is  $jj$ -coupled, while at short range it is  $LS$ -coupled. We can therefore simplify  $U_{i\alpha}$  by introducing an intermediate basis  $\bar{\alpha}$  of purely  $LS$  coupled channels, and writing  $U_{i\alpha}$  as the product of the  $jj$ - $LS$  transformation matrix  $U_{i\bar{\alpha}}$  and a second matrix  $V_{\bar{\alpha}\alpha}$  representing mixing between  $LS$ -coupled channels [100, 110]:

$$U_{i\alpha} = U_{i\bar{\alpha}} V_{\bar{\alpha}\alpha}, \quad (\text{A6})$$

where  $U_{i\bar{\alpha}}$  corresponds to the  $LS$ - $jj$  frame transformation

$$\begin{aligned} U_{i\bar{\alpha}} &= \langle ((S_c L_c) J_c (s \ell) j) J | ((S_c s) S (L_c \ell) L) J \rangle \\ &= [S, L, J_c, j]^{1/2} \begin{Bmatrix} S_c & L_c & J_c \\ s & \ell & j \\ S & L & J \end{Bmatrix} \end{aligned} \quad (\text{A7})$$

from Eq. (6.4.2) of Ref. [111] and  $[a, b, \dots]^{1/2} = \sqrt{(2a+1)(2b+1)\dots}$ .

The second matrix  $V_{\bar{\alpha}\alpha}$  accounts for configuration interaction by introducing couplings between the  $\bar{\alpha}$  channels.  $V_{\bar{\alpha}\alpha}$  is typically expressed as a series of rotations by Euler angles  $\theta_{ij}$  around channels  $i$  and  $j$  (see Eq. (15) of Ref. [112])

$$V_{\bar{\alpha}\alpha} = \prod \mathcal{R}(\theta_{ij}). \quad (\text{A8})$$

If the  $\theta_{ij}$  are small, the sequence of the rotations in Eq. (A8) is not critical, however, in general  $U_{i\alpha}$  will be sensitive to the chosen order.

In general, even in the absence of multi-channel interactions, the eigenchannel quantum defect is energy dependent. The energy dependence originates for example from a polarization of the ion core by the outer electron [113]. In practice, the eigenchannel quantum defect only slowly varies with energy and we treat energy-dependence of the eigenchannel quantum defects as

$$\mu_\alpha(\epsilon) = \mu_\alpha^{(0)} + \epsilon \mu_\alpha^{(2)} + \epsilon^2 \mu_\alpha^{(4)} \dots \quad (\text{A9})$$

and similarly we treat the energy dependence of  $\theta_{ij}$  by

$$\theta_{ij}(\epsilon) = \theta_{ij}^{(0)} + \epsilon \theta_{ij}^{(2)} \dots, \quad (\text{A10})$$

where  $\epsilon = 1/\nu^2$  [100].

## 3. MQDT models for hyperfine isotopes

For isotopes with non-zero nuclear spin, the hyperfine interaction in the ion core has to be considered. Here, we follow a similar formalism introduced in earlier work [73, 77, 78].

In the close-coupling region, the hyperfine interaction in the ion core is small compared to the exchange interaction and can be treated as perturbation to the fine structure. The close-coupling  $\alpha$  channels are split into  $\alpha_F = |(((S_c s) S (L_c \ell) L) J I) F\rangle$  channels, where the MQDT parameters  $\mu_\alpha \approx \mu_{\alpha_F}$  and  $U_{i\alpha} \approx U_{i\alpha_F}$  are only slightly affected. Therefore, we can construct the MQDT models for isotopes with non-zero nuclear spin from MQDT models obtained from even isotopes with nuclear spin  $I = 0$ . In this work, we use the MQDT models and parameters obtained for  $^{174}\text{Yb}$  and introduce hyperfine coupling of the ion core with

$$U_{i_F, \alpha_F} = U_{i_F, i} U_{i, \alpha_F} \quad (\text{A11})$$

where

$$U_{i, \alpha_F} = U_{i\bar{\alpha}} V_{\bar{\alpha}\alpha_F}, \quad (\text{A12})$$

and  $U_{i_F, i}$  is the frame transformation

$$\begin{aligned} U_{i_F, i} &= \langle (((J_c I) F_c j) F) | (J_c j) J I) F \rangle \\ &= (-1)^{I+j+F_c+J} [J, F_c]^{1/2} \begin{Bmatrix} I & J_c & F_c \\ j & F & J \end{Bmatrix}, \end{aligned} \quad (\text{A13})$$

where  $J$  corresponds to the total electronic angular momentum,  $I$  is the nuclear spin,  $F$  is the total angular momentum including nuclear spin, which uses Eq. (6.4.2) of Ref. [111].

We find that directly applying the  $^{174}\text{Yb}$  MQDT parameters (*i.e.* eigenchannel quantum defects  $\mu_\alpha$  and rotations  $\theta_{ij}$ ) to the  $^{171}\text{Yb}$  energies generally gives good agreement, but we find that a slight re-optimization of the model parameters is necessary for an improved modeling. We attribute this variation to three main reasons. First, a small isotope dependence [52] and hyperfine-induced mixing of channels can yield variations in the close-coupling parameters. Second, while we do not explicitly include direct coupling of the outer electron with

the nucleus, this interaction can be expressed through the matrix elements of  $V_{\alpha\alpha}$  and  $\mu_\alpha$ . Therefore, to the extent that this interaction is significant, it can be incorporated into the model. We note that the magnitude of this direct coupling scales as  $\nu^{-3}$  [69] and is at the scale of 1 MHz at  $\nu = 30$ , which is smaller than the current disagreement between the MQDT model and the experimentally measured state energies (*i.e.*, Fig.4). Therefore, attempting to predict this interaction strength and including it by hand would not significantly improve the model prediction. Third, we only consider the hyperfine splitting in the  $6s^2S_{1/2}$  ground state of the  $^{171}\text{Yb}^+$  ion. We neglect the hyperfine splitting of excited states of the  $^{171}\text{Yb}^+$  ion core. This is likely a good approximation because the excited states are energetically far above the channels converging to the  $^{171}\text{Yb}^+$  ground state considered in this work, but could lead to changes in the MQDT parameters.

#### 4. MQDT wavefunctions

Once a bound state  $b$  has been found with Eq. (A4) and Eq. (A5), its wavefunctions are conveniently expressed in the  $jj$  basis and Eq. (A2) is rewritten as

$$|\psi_b\rangle = |\Psi_b\rangle / N_b = \sum_i |\Phi_i\rangle P_{\nu_i, b, l_i}(r) A_{i, b}, \quad (\text{A14})$$

where  $P_{\nu_i, b, l_i}(r)$  is the radial Coulomb function of the active electron,  $A_{i, b}$  are the normalized channel contributions in terms of collision channels  $i$  in  $jj$ -coupling [100]

$$A_{i, b} = (-1)^{l_i+1} (\nu_{i, b})^{3/2} \sum_\alpha U_{i\alpha} \cos[\pi(\nu_{i, b} + \mu_\alpha)] \tilde{A}_{\alpha, b} / N_b, \quad (\text{A15})$$

and  $N_b$  ensures the normalization [41] of the wavefunction and is given by [100]

$$\begin{aligned} N_b^2 &= \sum_{i, \alpha} \nu_{i, b}^3 U_{i\alpha} \cos[\pi(\nu_{i, b} + \mu_\alpha)] \tilde{A}_{\alpha, b} \\ &+ \sum_\alpha \left( \frac{d\mu_\alpha}{dE} \right) \tilde{A}_{\alpha, b}^2 \\ &+ \frac{1}{\pi} \sum_{i, \alpha, \beta} \left( \frac{dU_{i, \alpha}}{dE} \right) U_{i, \beta} \sin[\pi(\mu_\alpha - \mu_\beta)] \tilde{A}_{\alpha, b} \tilde{A}_{\beta, b}. \end{aligned} \quad (\text{A16})$$

The wavefunction coefficients  $\tilde{A}_{\alpha, b}$  of Eq. (A2) are obtained by evaluating

$$\tilde{A}_{\alpha, b} = C_{i\alpha} / \left[ \sum_\alpha C_{i\alpha}^2 \right]^{1/2}, \quad (\text{A17})$$

where  $C_{i\alpha}$  is the cofactor of the  $i^{\text{th}}$  row and  $\alpha^{\text{th}}$  column of the matrix  $F_{i\alpha}$  (see Eq. (A4)), and in the evaluation of Eq. (A17), channel  $i$  can be chosen for convenience [100].

The close-coupling  $\alpha$  channel fractions ( $LS$  coupling) can be obtained from  $A_i$  as:

$$A_{\bar{\alpha}, b} = \sum_i U_{i\bar{\alpha}} A_{i, b}. \quad (\text{A18})$$

#### 5. Evaluation of matrix elements

We evaluate the matrix elements following the procedures introduced in Ref. [44], which are summarized in the following.

Single atom matrix elements between state  $b$  and  $b'$  of operator  $\hat{\zeta}$  acting on the channel function  $|\Phi_i\rangle$  in Eq. (A14) that leaving the orbital angular momentum  $l$  of the Rydberg electron unchanged are evaluated by

$$\zeta_{b, b'} = \sum_{i, i'} (A^T)_{b, i} \langle \Phi_i | \hat{\zeta} | \Phi_{i'} \rangle O_{ib, i'b'} A_{i', b'} \quad (\text{A19})$$

where

$$O_{ib, i'b'} = \int_0^\infty P_{\nu_i, b, l_i}(r) P_{\nu_{i'}, b', l_{i'}}(r) dr \quad (\text{A20})$$

is a radial overlap integral. The overlap integral can either be evaluated using analytic approximations [44, 114] or numerical wavefunctions obtained from the Numerov algorithm [12, 114].

This form of matrix elements is used in the evaluation of magnetic moments in the paramagnetic interaction Hamiltonian

$$H_{\text{PM}} = -\vec{\mu} \cdot \vec{B} = \{ \mu_B [\vec{L}_c + \vec{\ell} + g_s (\vec{S}_c + \vec{s})] - \mu_I \vec{I} \} \cdot \vec{B} \quad (\text{A21})$$

using the expressions presented in Ref. [44] for the general case of Rydberg states with hyperfine interaction in the ion core, where  $\mu_B$  is the Bohr magneton,  $\mu_I$  is the nuclear magnetic moment, and  $g_s$  is the electron spin  $g$ -factor.

For the case of the multipole operator  $\hat{\mathcal{Q}}^{(kq)} = r^k Y_{k, q}(\Omega)$ , the contribution of the core electrons is neglected and only the contribution of the Rydberg electron is considered (because of its much larger spatial extent):

$$\mathcal{Q}_{b, b'}^{(kq)} = \sum_{i, i'} (A^T)_{b, i} \langle \Phi_i | Y_{kq} | \Phi_{i'} \rangle R_{ib, i'b'}^{(k)} A_{i', b}, \quad (\text{A22})$$

where  $R_{ib, i'b'}^{(k)}$  is the radial integral

$$R_{ib, i'b'}^{(k)} = \int r^k P_{\nu_i, b, l_i}(r) P_{\nu_{i'}, b', l_{i'}}(r) dr. \quad (\text{A23})$$

Matrix elements of the form presented in Eq. (A22), are used in the calculation of Stark shifts [12], Rydberg-Rydberg interactions [14] and the diamagnetic shift.

The diamagnetic interaction Hamiltonian [115] is given by

$$H_{\text{DM}} = \frac{1}{8m_e} \left| \vec{d} \times \vec{B} \right|^2, \quad (\text{A24})$$

and can be expressed in terms of spherical harmonics (compare, e.g., Ref [83])

$$H_{\text{DM}} = \frac{e^2}{12m_e} r^2 \sqrt{4\pi} \left( Y_{0,0} - \sqrt{\frac{1}{5}} Y_{2,0} \right) B^2. \quad (\text{A25})$$

Due to the multichannel nature of MQDT eigenstates, calculating matrix elements between two MQDT eigenstates as presented in Eq. (A19) and Eq. (A22) requires calculating radial and angular integrals for all combinations of the electronic configurations encoded in the channel wavefunctions. We note that if a state has contributions from channels with significantly different ionization limits, the radial Coulomb functions  $P_{\nu_{i,b},l_i}(r)$  of each channel will vary significantly in spatial extent because of the  $\nu_{i,b}^2$  scaling of the orbital radius of the active electron. In practice, we neglect the contribution of channels with ionization limits significantly larger than the first ionization limit, since the associated wavefunctions are much more compact than those belonging to the lower limit and have comparatively small contributions to matrix elements of the form  $r^k$ . The only case in which radial wavefunctions corresponding to different thresholds are considered is in the case of the hyperfine-split thresholds in  $^{171}\text{Yb}$ .

## 6. Numerical evaluation

We compute state polarizabilities and interaction potentials following numerical techniques established for alkali atoms [12, 83, 84, 116], but adapted to compute matrix elements of MQDT eigenstates as described in the

previous section. We review the approach here to high-light important features.

The energy of an atom in an electric and magnetic fields  $F$  and  $B$  is given by:

$$H = H_0 + F e r + H_{\text{PM}} + H_{\text{DM}} \quad (\text{A26})$$

where  $H_0$  encodes the energy in the absence of the field, and  $H_{\text{PM}}$  and  $H_{\text{DM}}$  are defined in Eqs. (A21) and (A24), respectively. To determine the energy shift for a target state  $|\psi_0\rangle$ , we numerically evaluate the matrix elements of Eq. (A26) in a large basis of states  $\{|\psi_i\rangle\}$ , and then diagonalize [12].

The matrix elements  $\langle \psi_i | r | \psi'_i \rangle$  and  $\langle \psi_i | r^2 | \psi'_i \rangle$  (in  $H_{\text{DM}}$ ) are evaluated using Eq. (A22). Computing the radial integral in Eq. (A23) requires numerical wavefunctions, which we compute using the Numerov method [12], following the implementation in the Alkali Rydberg Calculator [84]. The Numerov method computes the radial wavefunction of a bound state from its energy, relative to the ionization limit. We note that MQDT states do not have a unique radial wavefunction: each channel may have a distinct ionization limit. Therefore, the matrix element in Eq. (A22) involves summing over several different wavefunctions.

The energy shift in small magnetic fields can be estimated from the diagonal elements of Eq. (A26). The Stark shift in a small electric field can be estimated from diagonalizing Eq. (A26) in a small basis consisting of the several closest states with opposite parity. However, evaluating a full Stark map with multiple level crossings, or evaluating the diamagnetic shift in large fields resulting in level crossings, requires a larger basis of hundreds or thousands of states.

The Hamiltonian of two interacting Rydberg atoms in the Born-Oppenheimer approximation can be written as

$$H = H^{(1)} + H^{(2)} + H_{\text{int}}, \quad (\text{A27})$$

where  $H^{(1)}$  and  $H^{(2)}$  are the Hamiltonians of the two isolated Rydberg atoms (Eq. (A26)). The interaction Hamiltonian  $H_{\text{int}}$  is evaluated through an expansion over multipole terms  $k_1$  and  $k_2$  [117, 118]

$$H_{\text{int}} = \sum_{k_1, k_2} \frac{(-1)^{k_2}}{R^{k_1+k_2+1}} \sqrt{\frac{(4\pi)^3 (2k_1+2k_2)!}{(2k_1+1)! (2k_2+1)! (2k_1+2k_2+1)}} \times \sum_{p=-(k_1+k_2)}^{k_1+k_2} \sum_{p_1=-k_1}^{k_1} \sum_{p_2=-k_2}^{k_2} C_{k_1, p_1, k_2, p_2}^{k_1+k_2, p} r_1^{k_1} r_2^{k_2} Y_{k_1, p_1}(\hat{r}_1) Y_{k_2, p_2}(\hat{r}_2) Y_{k_1+k_2, p}(\hat{R}), \quad (\text{A28})$$

where  $\hat{R}$  is a vector representing the internuclear axis,

$C_{k_1, p_1, k_2, p_2}^{k_1+k_2, p} = \langle k_1, p_1; k_2, p_2 | k_1 + k_2, p \rangle$  is a Clebsch-

Gordan coefficient, and  $Y_{\kappa,p}(\hat{r})$  are unit-normalized spherical harmonics.

The calculations presented in this work are restricted to dipole-dipole interactions ( $k_1 = k_2 = 1$ ), though we note that higher-order multipoles can become important at short separations [24], and the  $R^{-5}$  term from  $k_1 = k_2 = 1$  can also dominate the asymptotically long-range interaction [86].

As with the case of the field shift, the matrix elements are evaluated numerically using Eq. (A22) at fixed internuclear separations  $R$ . The size of the required basis for computing pair interactions is much larger than for evaluating single-atom energy level shifts. Moreover, compared to alkali atoms,  $^{174}\text{Yb}$  has twice the number of Rydberg states ( $S = 0$  and  $S = 1$ ), while  $^{171}\text{Yb}$  has four times as many when including the nuclear spin.

We therefore restrict the size Rydberg pair basis by only including pair states with significant contribution to the interaction potential in an energy range close to a target pair state [14]. The Rydberg pair basis is formed in two steps. First, we build the pair basis from a set of single atom states with similar effective principal quantum number  $\nu$  and orbital angular momentum  $L$  as the target state. The resulting pair basis is then further truncated to pair states with a small pair-energy defect  $\Delta E$  to the target pair state. Depending on the orientation of the internuclear axis with respect to external fields and the included orders of the multipole expansion, the basis size can be additionally restricted by making use of selection rules of the spherical harmonics under the conservation of certain symmetries [83].

$\Delta E$ ,  $\Delta\nu$  and  $\Delta L$  are then increased until convergence is observed. Typically, values of  $\Delta\nu \lesssim 3$  are sufficient to produce accurate interaction potentials [14, 83]. To give a sense of scale, the computations in Fig. 7 included Rydberg pair state with  $\Delta\nu < 3$ ,  $\Delta L = 1$ , and  $\Delta E < 10$  GHz, yielding a basis of approximately 2000 pair states.

## Appendix B: Atomic beam spectroscopy apparatus

The spectroscopic data presented in this article are obtained by laser and radiofrequency (RF) spectroscopy on an atomic beam of  $^{174}\text{Yb}$  or  $^{171}\text{Yb}$  atoms (see Fig. 9a and b). The atomic beam is generated by heating a sample of ytterbium to a temperature of 310 °C in an oven with a collimator opening of approximately 1 cm. The atomic beam is further collimated by a pinhole with a diameter of 3 mm, approximately 12 cm after the oven collimator and 9 cm before the spectroscopy region.

Transitions to S and D Rydberg states are driven by a two-photon laser transition through the intermediate  $6s6p^1P_1$  state. The laser light needed for the transition with wavelengths of 399 nm ( $6s^2^1S_0 \rightarrow 6s6p^1P_1$ ) and 394–399 nm ( $6s6p^1P_1 \rightarrow$  Rydberg state) is generated by frequency doubling the output of tunable titanium-sapphire (Ti:sapph) lasers in a resonantly enhanced frequency doubling cavity. The isotope shifts on

the  $6s^2^1S_0 \rightarrow 6s6p^1P_1$  transition [119] are used for an isotope selective excitation into the Rydberg state. To minimize Doppler shifts on the two-photon laser transitions, counter-propagating laser beams are applied at a 90° angle relative to the atomic beam (along the  $y$  axis in Fig. 9). Laser pulses with length of 1-3  $\mu\text{s}$  are generated by acousto-optic modulators. The laser frequencies are monitored by measuring the frequency of the fundamental output of the Ti:sapph laser using a HIGHFINESSE WS8-10 wavelength meter with a specified  $3\sigma$  uncertainty of 10 MHz. At regular intervals, the wavelength meter is calibrated to a 399 nm laser that is frequency locked to a ultra-low-expansion cavity with known offset from the  $^1S_0 \rightarrow ^1P_1 (F = 3/2)$  transition in  $^{171}\text{Yb}$ .

Population in Rydberg states is detected by state-selective pulsed-field ionization (see, e.g., [69]). High-voltage (HV) ramps with a maximum voltage of 2.5 kV are generated by switching between a low-voltage (during Rydberg spectroscopy) and a HV input using HV MOSFET switches (BEHLKE HTS 31-03-GSM) and are applied to a set of electrodes (on the right side of the atomic beam in Fig. 9) through a  $RC$  low-pass filter ( $\tau = 1 \mu\text{s}$ ). The resulting maximum field of  $\approx 833 \text{ V cm}^{-1}$  limits the lowest detectable Rydberg states in our setup to an effective principal quantum number  $\nu \approx 26$ . The resulting  $\text{Yb}^+$  ions are accelerated towards and detected on a time-resolved microchannel-plate (MCP) ion detector (HAMAMATSU F13446-11) and recorded on an oscilloscope. To reduce electric field inhomogeneities caused by the high-voltage (typically  $-1.9 \text{ kV}$ ) applied to the front surface of the MCP, we place a grounded grid mesh about halfway in between the spectroscopy region and the MCP. The experiment is operated at a repetition rate of 1 kHz, limited by the current drawn at the HV supply generating the HV field-ionization ramps.

An exemplary laser spectrum of the  $|40.70, S, F = 1/2\rangle$  Rydberg state of  $^{171}\text{Yb}$  is presented in Fig. 9c. Transition frequencies to the Rydberg state are determined by a least-square fit of the data to a Gaussian line shape model.

Transition between Rydberg states are driven using RF with frequencies in the range of 10-175 GHz. The RF radiation is obtained from a WINDFREAK TECHN., LLC SYNTHHD PRO (up to 24 GHz) dual-channel microwave generator or by using a combination of active x4 (MARKI MICROWAVE AQA-2156, 21-56 GHz, 20 dBm) and/or passive x4 (MARKI MICROWAVE MMQ-40125H, 40-175 GHz, 0 dBm) frequency multipliers. The microwave generator is referenced to a stable 10 MHz reference signal obtained from a GPS disciplined Rb atomic clock (STANFORD RESEARCH SYSTEMS FS725). RF pulses with duration of 1-8  $\mu\text{s}$  are obtained by amplitude modulating the output of the microwave generator before frequency multiplication using PIN absorptive modulators (HEWLETT PACKARD 33008C or 11720A). The obtained RF radiation is coupled into the vacuum chamber through vacuum viewports using suitable horn antennas. All laser radiation is switched off for the duration of

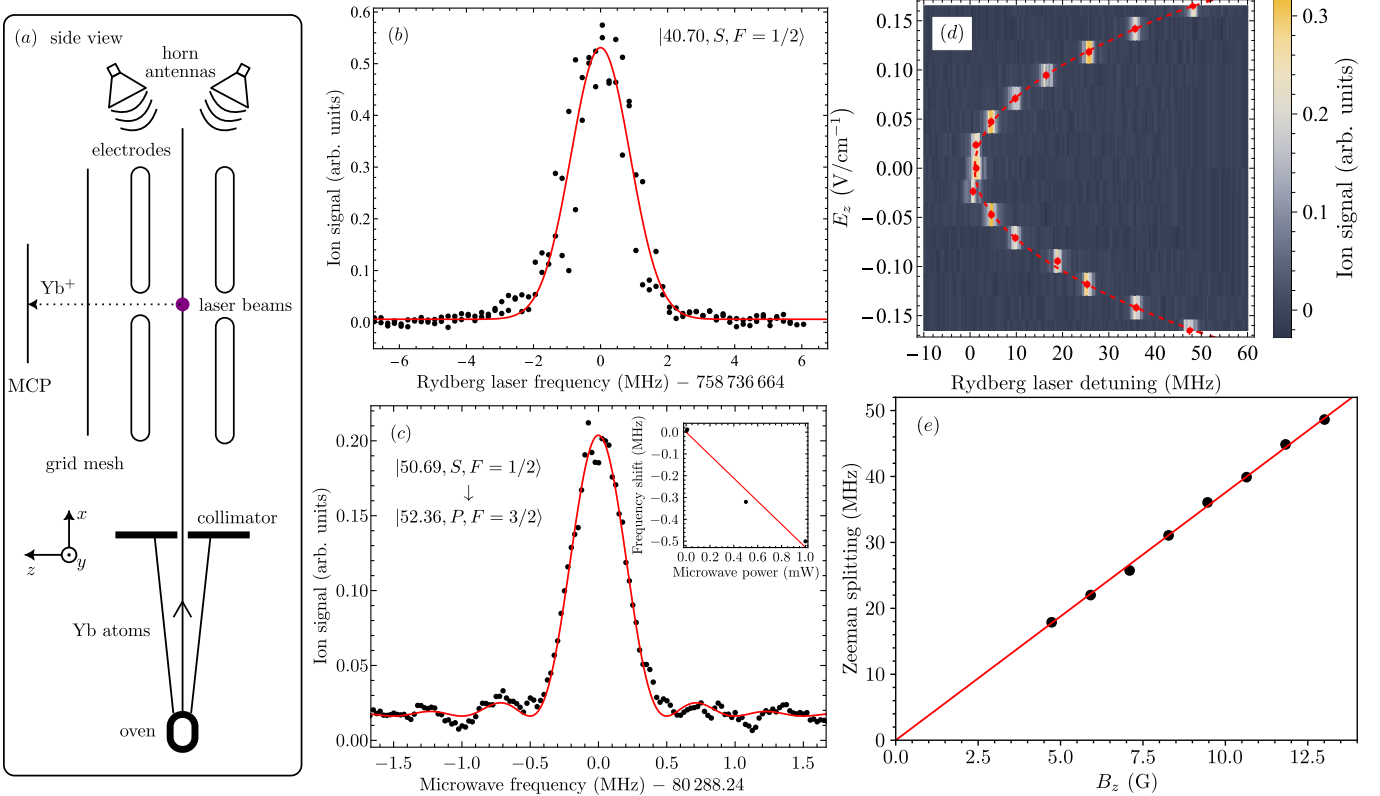


Figure 9. (a) Schematic of the atomic beam apparatus used for spectroscopy on Yb Rydberg state. See text for details. (b) Typical laser excitation spectrum, showing the  $^{171}\text{Yb}$ ,  $|40.70, S, F = 1/2\rangle$  Rydberg state. Each black point corresponds to the integrated time-resolved ion signal averaged over 1000 repetitions of the experiment. The obtained data is fit to a Gaussian line shape model (red line) with a full width at half maximum (FWHM) of 2.1 MHz. (c) Typical microwave spectrum of a  $|50.69, S, F = 1/2\rangle \rightarrow |52.36, P, F = 3/2\rangle$  transition in  $^{171}\text{Yb}$ . Each black point corresponds to the integrated time-resolved ion signal averaged over 1000 repetitions of the experiment. The obtained data is fit to a sinc<sup>2</sup> line shape model (red line) for a  $2\ \mu\text{s}$  rectangular microwave pulse. *Inset:* Extrapolation of the transition frequency to zero microwave power. (d) Typical polarizability measurement of the  $|62.14, S, F = 1/2\rangle$  Rydberg state, obtained by recording laser spectra in a range of electric fields  $F_z$ . The transition frequencies (red dots) are obtained by a least-squared fit of a Gaussian line shape model to the experimental data. The static dipole polarizability of the state is obtained by a least-squared fit of Eq. (B1) (dashed red line) to observed Stark shifts. (e) Zeeman splittings between the  $|50.69, S, F = 1/2, m_F = \pm 1/2\rangle$  magnetic sub-levels obtained by laser spectroscopy in a magnetic field  $B_z$ .  $g$  factors of the Rydberg states are obtained by a least-square fit of the experimental data to Eq. (B2).

the RF pulses. The power of the RF radiation is controlled using either a digital step attenuator (ANALOG DEVICES ADRF5740) or a WR-10 direct-reading attenuator (MI-WAVE 510W/387). A microwave spectrum of the  $33^1S_0 \rightarrow 33^1P_1$  transition in  $^{174}\text{Yb}$  is presented in Fig. 9d. Transition frequencies between Rydberg states are determined by a least-square fit of the data to either a sinc<sup>2</sup> or Lorentzian line shape model. All stated Rydberg-Rydberg transitions have been measured at varying RF powers and extrapolated to “zero” RF power to remove frequency shifts caused by AC-Stark shifts.

To control the electric field in the spectroscopy region, we apply voltages to two segmented circular electrodes (4 segments each) separated by 3 cm. Stray electric fields are compensated at the beginning of each day, by minimizing the quadratic Stark shift of the  $6s130s\ 130^1S_0$

Rydberg state of  $^{174}\text{Yb}$ . We observe day-to-day fluctuations of the required electric compensation fields of less than 3 mV/cm.

We determine values for the static dipole polarizabilities  $\alpha_0$  of Rydberg states by measuring a shift in the transition frequencies caused by applying electric fields  $F$  between the two segmented circular electrodes and subsequent fitting to

$$\Delta E_{\text{Stark}} = -(1/2) \alpha_0 F^2. \quad (\text{B1})$$

When possible, we ensured that the static dipole polarizabilities are determined in a range of quadratic Stark shifts. For some cases, the Stark shift deviates from a quadratic scaling even at very small electric fields and we report values for the Stark shift at a given electric field instead.

Magnetic fields in all three spatial directions are controlled by three pairs of coils placed outside the vacuum chamber, arranged in Helmholtz configuration. The magnetic fields generated by the coils are calibrated by RF spectroscopy of the Zeeman splittings on a  $n'{}^3S_1 \leftarrow n{}^1S_0$  transition, and assuming a  $g$ -factor of the mostly unperturbed  $n{}^3S_1$  Rydberg series to be  $g({}^3S_1) = g_s \approx 2.0023$ . We obtain values for Landé  $g$  factors of Rydberg states by measuring Zeeman shifts caused by applying calibrated magnetic fields  $B$  and subsequent a subsequent linear fit to

$$\Delta E_{\text{Zeeman}} = mg\mu_B B, \quad (\text{B2})$$

where we measured the Zeeman shifts at sufficiently small magnetic fields to avoid the effect of non-linear diamagnetic shifts.

### Appendix C: Measuring Rydberg interactions in optical tweezers

We measure the distance-dependent interactions between single  ${}^{171}\text{Yb}$  Rydberg atoms trapped in optical tweezer arrays using the setup described in Ref. [40]. Similar approaches have been previously used to measure  $C_6$  coefficients of Rydberg-pair states in Rb [15] and angle-dependent dipole-dipole interaction strengths [16]. We initialize pairs of atoms in the  $|1\rangle \equiv |m_F = +1/2\rangle$  sublevel of the  $6s6p{}^3P_0$  metastable state. Static magnetic fields are applied at  $90^\circ$  ( $\theta = \pi/2$ ) with respect to the internuclear separation. Transitions into Rydberg pair states are subsequently driven by a two-photon transition detuned by  $\Delta E$  from the asymptotic case of two isolated Rydberg atoms. Pairs of atoms transferred into Rydberg states are blown out of the optical tweezers by driving a transition (369 nm) into an autoionizing state [96]. Remaining atoms in the  $|1\rangle$  state are depumped into the  ${}^1S_0$  ground state for fluorescence imaging. The excitation of a Rydberg-pair state is inferred by conditioning the remaining atom population after a given experimental sequence on pair-wise atom loss. An exemplary pair-state spectrum close to the  $|54.28, L = 0, F = 1/2, -1/2\rangle^{\otimes 2}$  asymptotic pair state is given in Fig. 10c. For a given optical tweezer separation, we observe an increase in pairwise atom loss when tuning the two-photon transition over a Rydberg pair state. The pair-state resonance shifts to larger two-photon detuning when reducing the tweezer separation, indicating a larger interaction between the two Rydberg atoms. We fit the observed pair-state spectra using a Gaussian line shape model. The resulting center frequency of the fits are presented in Fig. 6 and Fig. 7.

On top of the shift of the pair-state resonance, we also observe a broadening. We attribute the observed broadening to the spatial fluctuations of the single atoms in the optical tweezers ( $T \approx 3 \mu\text{K}$ ). Due to the spatial fluctuations of the atoms, the linewidth of the pair-state

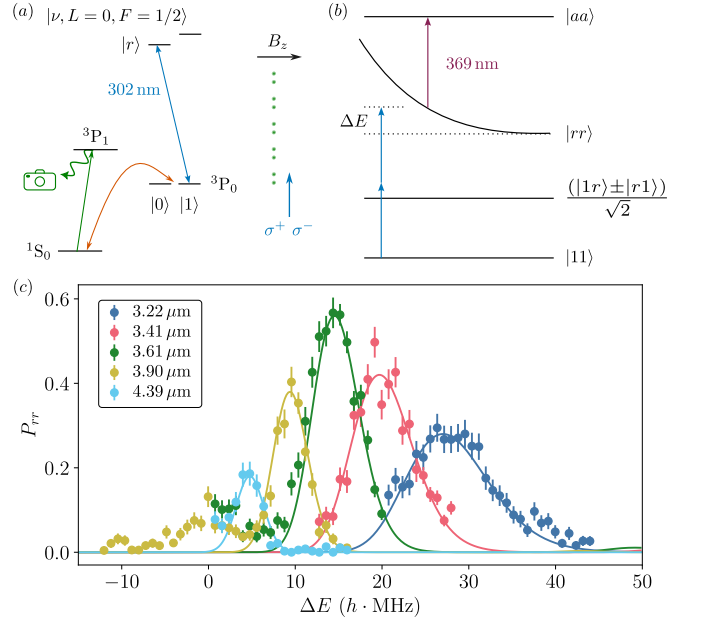


Figure 10. (a) Single-atom transition scheme for measuring interactions between pairs of Rydberg atoms in an optical tweezer setup [40]. The  ${}^{171}\text{Yb}$  atoms are prepared states in the  $|1\rangle$  sublevel of the  ${}^3P_0$  metastable state. Transitions into the  $|\nu, L = 0, F\rangle$  Rydberg state are driven by a single-photon transition (302 nm). For rearrangement and readout, the atoms are imaged by collecting the fluorescence on the  $|{}^1S_0\rangle \leftrightarrow |{}^3P_1\rangle$  transition. (b) Scheme for measuring Rydberg-Rydberg interactions between pairs of single atoms trapped in optical tweezer arrays. (c) Experimental pair-state spectra (solid dots), obtained by recording the probability of pair-wise loss from tweezers in fluorescence image as a function of two-photon detuning and tweezer separation. The experimental spectra are compared to simulated pair spectra  $S(E)$  (solid lines) obtained from Eq. (C1), as explained in the text.

resonance is affected by the gradient of the interaction potential, which increases towards shorter internuclear separations. To model the effect of fluctuating internuclear separations in the optical tweezers, we simulate the pair-state spectra  $S(E)$

$$S(E) \propto \sum_{\Phi} \mathcal{G}(E - E_{\Phi}(R), \sigma_E) \mathcal{T}(R - \tilde{R}, \sigma_R) \mathcal{O}_{\Phi, \Phi'}(R), \quad (\text{C1})$$

where the sum runs over all relevant pair state  $\Phi$  coupled to the target state  $\Phi'$ ,  $E_{\Phi}(R)$  is the internuclear-separation-dependent pair-state energy,  $\tilde{R}$  is the mean internuclear separation,  $\mathcal{G}(E - E_{\Phi}(R), \sigma_E)$  is a function describing the experimental linewidth of the spectrum in the absence of any broadening,  $\mathcal{T}(R - \tilde{R}, \sigma_R)$  is a function describing the distribution of internuclear separation around a mean separation  $\tilde{R}$ , and  $\mathcal{O}_{\Phi, \Phi'}(R)$  is the overlap coefficient.

For the case presented in Fig. 10c, the line broadening can be reproduced by assuming a normal distribution in the internuclear separations with standard deviation of

100 nm. This is close to the expected distance fluctuations of approximately 50 nm between two atoms confined in optical tweezers with radial and axial trap frequencies of  $\omega_r = 60$  kHz and  $\omega_z = 10$  kHz, respectively.

#### Appendix D: Additional spectroscopic data and models for $^{174}\text{Yb}$

In this appendix, we give additional details of the spectroscopic measurements and MQDT model development for  $^{174}\text{Yb}$ . We also make comparisons between the MQDT model and previously measured quantities, including singlet-triplet mixing in the  $^{1,3}P_1$  and  $^{1,3}D_2$  series, and diamagnetic shifts in the P series.

##### 1. $^3S_1$ and $^1S_0$

For the  $n^1S_0$  Rydberg series of  $^{174}\text{Yb}$ , we adapt the six-channel MQDT model presented in previous work [49]. We refit the MQDT model parameters of the  $^1S_0$ ,  $^{1,3}D_2$ ,  $^{1,3}P_1$  Rydberg series in a simultaneous, 42-parameter fit to the previously measured [46, 49, 50, 53–56, 58] and newly measured data presented in the supplemental material [70], leveraging the higher precision microwave measurements between S, D, and P Rydberg states. The resulting MQDT models are presented in Tab. S1, Tab. S2, and Tab. S3.

For the  $n^3S_1$  with  $n > 28$ , we adapt the single-channel quantum defect model with a Rydberg-Ritz expansion for the energy-dependent quantum defect presented in Ref. [29].

##### 2. $^1P_1$ and $^3P_1$

Here we introduce a six-channel MQDT model for the  $^{1,3}P_1$  Rydberg series of  $^{174}\text{Yb}$ . Compared to the five-channel model presented in Ref. [50], we introduce a sixth perturbing channel, which lies energetically above the first ionization limit of  $^{174}\text{Yb}$ . The addition of the sixth channel was necessary to accurately describe the energies of the high- $n$  states of this series. In addition, we introduce singlet-triplet mixing between the  $^1P_1$  and  $^3P_1$  explicitly, by introducing a rotation to the  $U_{i\alpha}$  matrix,  $\theta_{12}$  whose value is constrained by the Stark shift of the  $^1S_0$  state, as explained in Sec. II.

We extend the previously measured state energies of  $^{1,3}P_1$  [50, 56], by measuring microwave transition frequencies between  $n^{1,3}P_1$  and  $n'^{1,3}D_2$  or  $n'^1S_0$  Rydberg states in the range of  $31 \leq n \leq 43$ , as summarized in Tab. S18 and Tab. S19. We cross checked several transition frequencies reported in Ref. [50] and generally find good agreement within the stated error bars, with the exception of the  $6s45p^3P_1 \leftarrow 6s44s^1S_0$ , which deviates from our new measurement and the final theoretical prediction from the MQDT model by nearly 10 MHz. We

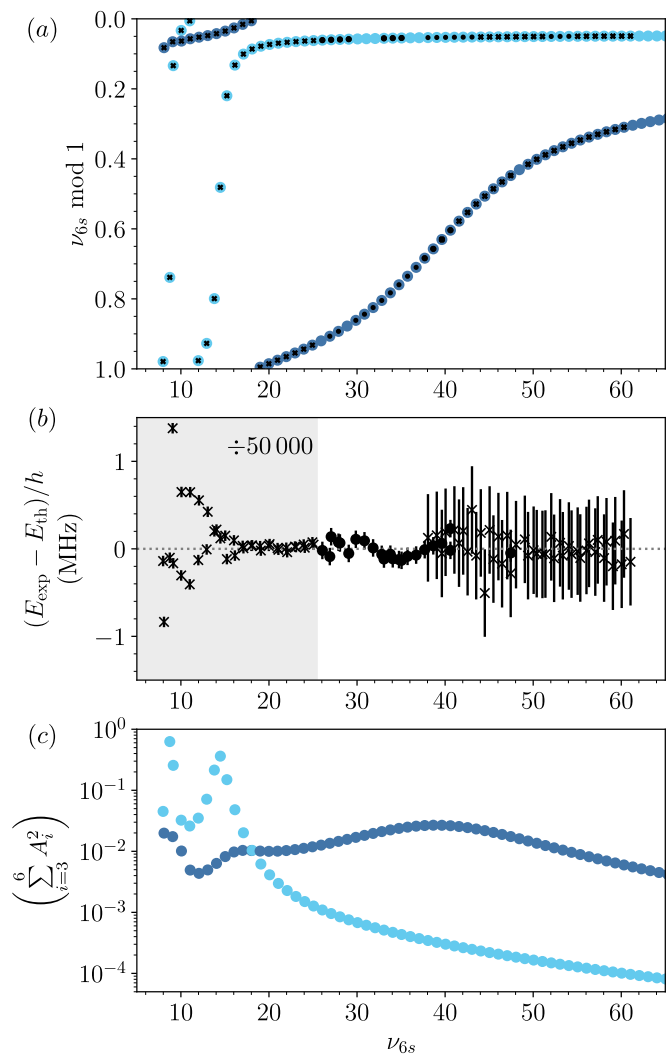


Figure 11. (a) Lu-Fano-type plot of the  $^{174}\text{Yb}$   $^{1,3}P_1$  Rydberg series. The theoretical bound states with dominant singlet and triplet character are indicated by light and dark blue dots, respectively. Experimentally observed states are indicated by black crosses (Refs.[50, 56]) and black dots (this work). (b) Deviation between experimental and theoretical state energies. The energy deviations and error bars in the gray shaded area are scaled by a factor of 50 000 to improve visibility of the much smaller errors observed on the microwave transitions. (c) Perturbing channel fraction  $\sum_{i=3}^6 A_i^2$  of the dominantly singlet (light blue) and triplet (dark blue) Rydberg states.

therefore don't include this data point in our analysis. In the fitting procedure, we optimize the 42 parameters of the  $^1S_0$ ,  $^{1,3}D_2$ ,  $^{1,3}P_1$  MQDT models in a simultaneous fit to the data presented in the supplemental material [70]. The resulting MQDT models are presented in Tab. S1, Tab. S2, and Tab. S3.

The presented MQDT model correctly predicts the energies of the highly excited  $n^{1,3}P_1$  Rydberg states (Fig. 11). However, below  $\nu < 15$ , significant deviations between the experimental and theoretical energies

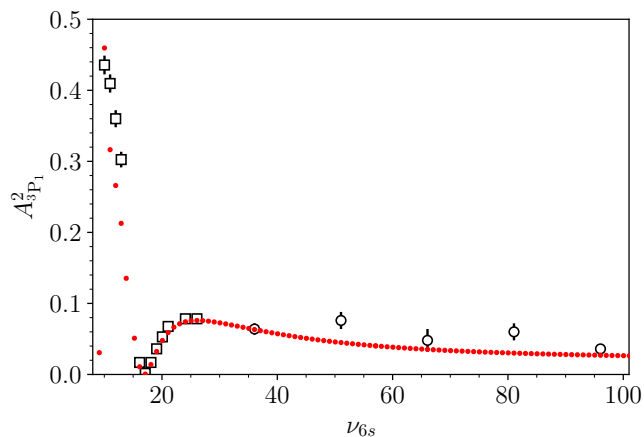


Figure 12.  $6snp^3P_1$  character ( $A_{3P_1}^2$ ) in  $6snp^1P_1$  Rydberg states of  $^{174}\text{Yb}$ . The open black squares correspond to experimental values obtained by measurements of the hyperfine-structure of  $^{171}\text{Yb}$  and  $^{173}\text{Yb}$   $1,3P_1$  Rydberg states from Ref. [82]. The open black circles correspond to experimental values obtained by measuring diamagnetic shifts taken from Ref. [57]. The full red circles correspond to theoretical values of  $A_{3P_1}^2$  as obtained from the MQDT model presented in Tab. S3.

occur. This could be due to unaccounted perturbing channels, either directly in the low- $\nu$  regime, or in the high- $\nu$  regime, with the current MQDT model parameters overcompensating trends in the quantum defects for the more accurately determined Rydberg states at high  $\nu$ .

The breakdown of pure  $LS$  coupling in the  $1,3P_1$  Rydberg channels is quantified by measuring the static dipole polarizabilities of  $n^1S_0$  Rydberg states in the vicinity of a near degeneracy with dominantly  $n^3P_1$  Rydberg states, as discussed in the main text. To obtain the best agreement between the experimental and theoretical static polarizabilities of the  $n^1S_0$  Rydberg states, an energy dependent singlet-triplet mixing angle (refer to Eq. (A10)) had to be introduced. The resulting MQDT parameters are presented in the supplemental material [70].

With the obtained  $J = 1$  (odd parity) MQDT model for  $^{174}\text{Yb}$  and using Eq. (A18), we can estimate the  $6snp^3P_1$  channel contribution into the nominally  $n^1P_1$  Rydberg states. The resulting values are presented in Fig. 12 and compared to values obtained from previous measurements of diamagnetic shifts, as presented in Ref. [57] and from previous hyperfine-structure measurements in  $^{171}\text{Yb}$  and  $^{173}\text{Yb}$ , as presented in Ref. [82]. The theoretically obtained values for the triplet contribution to the  $n^1P_1$  Rydberg states agree well with the previously reported values between  $20 \leq n \leq 100$ , but with significantly reduced uncertainties, highlighting the sensitivity of measuring matrix elements through Stark shifts close to near degeneracies.

As an additional check of the validity of the model, we compare the predicted Zeeman and diamagnetic shifts

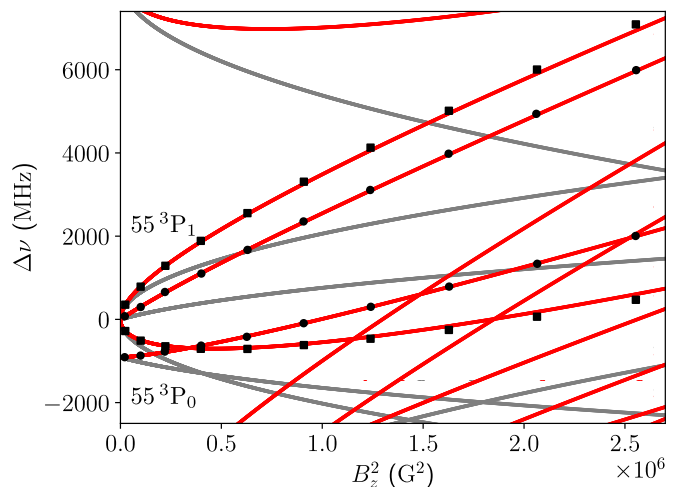


Figure 13. Zeeman shifts of  $^{174}\text{Yb}$  Rydberg states near the  $55^3P_1$  state. The red and gray curves correspond Zeeman shift calculations with and without diamagnetism, respectively. The near degeneracy of the  $55^3P_0$  and  $55^3P_1$  states, leads to a strong interaction between the  $55^3P_1(m_J = 0)$  and  $55^3P_0(m_J = 0)$  sublevels. The black circles and squares correspond to experimentally observed Zeeman shifts extracted from Fig. 3 of Ref. [57] for the  $m_J = 0$  and  $m_J = \pm 1$  sublevels, respectively. The experimental Zeeman shifts from Fig. 3 of Ref. [57] are plotted directly for the  $m_J = 0$  states, whereas the values for  $m_J \pm 1$  states are obtained from the mean experimental diamagnetic shifts and theoretical predictions for the paramagnetic contribution to the Zeeman shift.

in very large magnetic fields to a previous experimental measurement from Ref. [57]. In that work, the measured energies were fit with a phenomenological model to extract the singlet-triplet splitting for that  $n$ . In Fig. 13, we show the prediction of the MQDT model with no free parameters, finding excellent agreement.

### 3. $^3P_2$

Here, we introduce a four-channel MQDT model for  $^3P_2$  Rydberg states of  $^{174}\text{Yb}$ . In comparison to the previously presented three-channel MQDT model from Ref. [48], we introduce an additional channel with a perturbing state above the first ionization limit. The addition of the fourth channel was necessary to accurately describe the energies of the high- $n$  states of this series.

The MQDT model parameters are optimized in a weighted least-square procedure. The Rydberg state energies included in the fitting procedure include previously measured state energies of  $^3P_2$  by laser [56] and microwave spectroscopy [50], as well as newly measured microwave transition frequencies between  $n^3P_2$  and  $n'^3D_2$  Rydberg states in the range of  $31 \leq n \leq 43$ . The included Rydberg state energies and the resulting MQDT model parameters are presented in the supplemental material [70].

As depicted in Fig. 14(a) and (b), the newly intro-

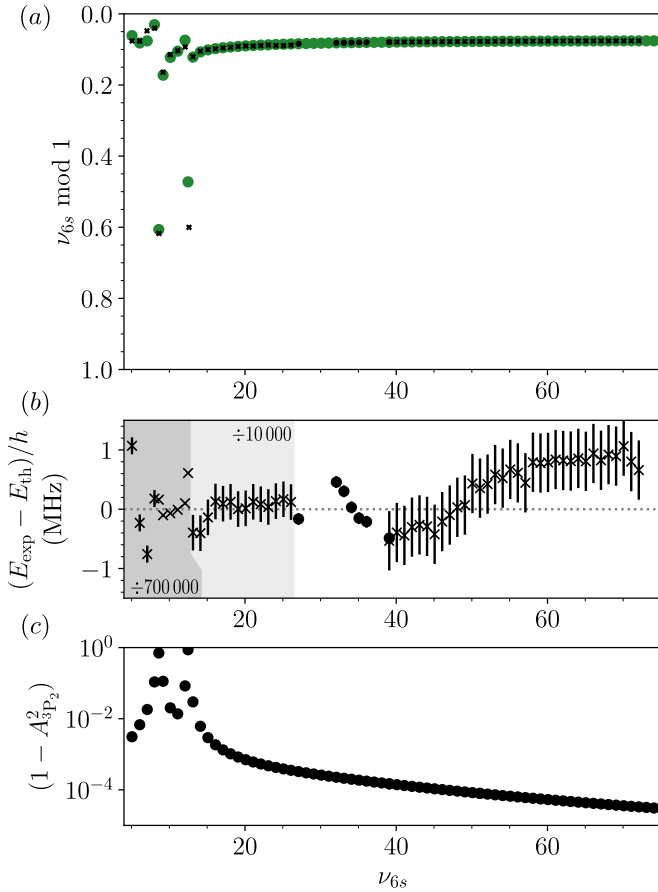


Figure 14. Lu-Fano-type plot of the  $^{174}\text{Yb } ^3P_2$  Rydberg series. The theoretical bound states are indicated by green dots. Experimentally observed states are indicated by black dots (Refs.[50, 56]) and dots (this work). (b) Deviation between experimental and theoretical state energies. The energy deviations and error bars in the light (dark) gray shaded area are scaled by a factor of 10 000 (700 000) to improve visibility of the much smaller errors observed on the microwave transitions. (c) Perturber fraction  $(1 - A_{3P_2}^2)$  of the Rydberg states in the  $(J = 2)^\circ$  Rydberg series.

duced MQDT model for  $^3P_2$  captures the energies of the highly excited  $n^3P_2$  Rydberg state quantitatively, but only qualitatively captures the energies of the states in the strongly perturbed range below  $\nu \approx 15$ .

Fig. 14c, depicts the contribution of the core excited channels, which are below  $10^{-3}$  for states with  $\nu > 20$ , confirming a mostly unperturbed  $^3P_2$  Rydberg series. Series perturbers can shorten the lifetime of Rydberg states even at high  $n$ , by introducing an additional decay channel proportional to  $\sum A_i \Gamma_i$ , where  $\Gamma_i$  is the decay rate of the perturbing states. Since  $\Gamma_i$  for low-lying atomic states can be substantially faster than for Rydberg states, even a small admixture can significantly alter the lifetime. We note that Ref. [29] measured the lifetime of the  $74^3P_2$  state to be  $83(5) \mu\text{s}$ , which is close to but slightly shorter than the lifetime predicted for a P state of  $^{87}\text{Rb}$  with a similar quantum number (approximately  $200 \mu\text{s}$  at

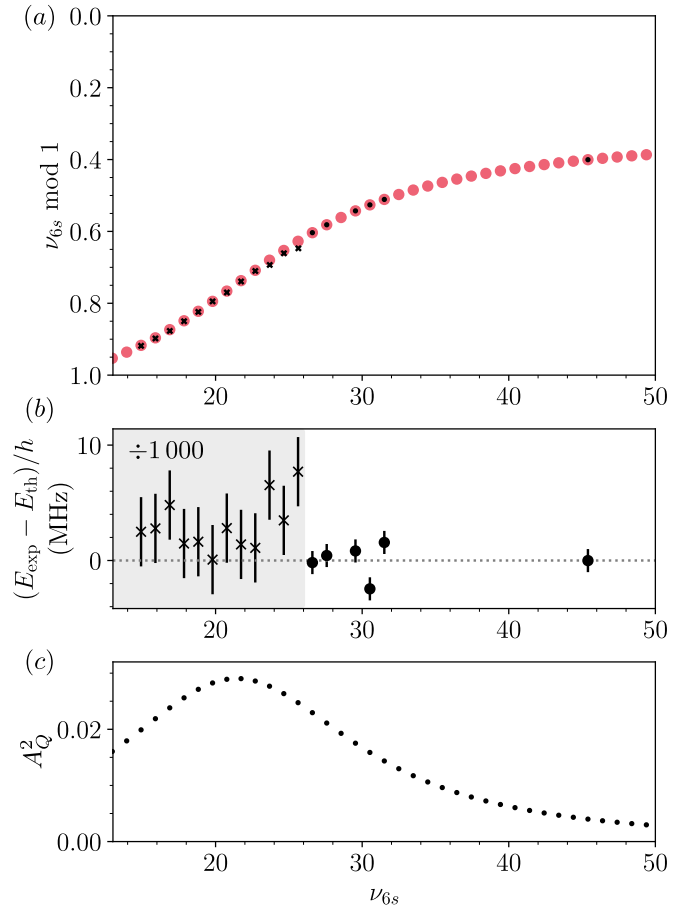


Figure 15. Lu-Fano-type plot of the  $^{174}\text{Yb } ^3P_0$  Rydberg series. The theoretical bound states are indicated by red dots. Experimentally observed states are indicated by black crosses (Ref.[56]) and dots (this work). (b) Deviation between experimental and theoretical state energies. The energy deviations and error bars in the gray shaded area are scaled by a factor of 1 000 to improve visibility of the much smaller errors observed on the microwave transitions. (c)  $Q$  channel contribution  $A_Q^2$  to the  $n^3P_0$  Rydberg states.

$T = 300 \text{ K}$  [120]). This is qualitatively consistent with the modeled small but non-zero perturbation of this series. A quantitative assessment will require predictions for matrix elements and decay rates of the perturbing states, which is a subject for future work.

#### 4. $^3P_0$

Here, we present a two-channel MQDT model for the  $n^3P_0$  Rydberg states of  $^{174}\text{Yb}$ . A two-channel model suffices to reproduce the observed states at high- $n$ , though we believe additional channels will eventually be necessary to explain the full series. We have no direct information about the nature of the perturbing series and follow Ref. [56] by assigning a perturbing channel with character  $4f^{13}5d6snd^3P_0$  (labelled  $Q$ ). The MQDT model param-

eters are optimized in a weighted least-square fit to both previously measured state energies by laser spectroscopy [56] and newly measured state energies from microwave spectroscopy, summarized in Tab. S24 and Tab. S23, respectively.

The  $n^3P_0$  Rydberg states are inaccessible by direct one-photon microwave transitions from laser accessible  $n^1S_0$  and  $n^{1,3}D_2$  Rydberg states. Instead, we perform spectroscopy on  $n^3P_0$  Rydberg states of  $^{174}\text{Yb}$ , by utilizing the Autler-Townes splitting on a probe transition. To this extent, we monitor the resonant population transfer on the two-photon  $n^3D_2 \rightarrow n'^3S_1$  microwave transition as a function of the frequency of a simultaneously applied microwave pulse coupling the  $n^3S_1 \rightarrow n''^3P_0$  transition. The observed  $n^3P_0 \leftrightarrow n'^3D_2$  intervals are summarized in Tab. S23. We recorded a total of six transitions to  $n^3P_0$  Rydberg states in the range of  $31 \leq n \leq 49$ , which were particularly necessary to determine the energy dependence of the strongly perturbed  $^3P_0$  series. The results of this measurement, together with previous three-photon laser spectroscopy [56] are presented in the supplemental material [70].

The obtained MQDT model is summarized in Tab. S5 and presented in a Lu-Fano-like plot in Fig. 15. The MQDT model represents the experimental data well within the experimental uncertainties over a range of  $18 \leq n \leq 50$ .

The contributions of perturbing channel  $Q$  into the  $n^3P_0$  Rydberg states is presented in Fig. 15c. The channel contribution is spread out over a wide range of principal quantum numbers and reaches a maximum value of approximately 3% at  $n = 26$ . This is consistent with a significantly reduced lifetime of the  $74^3P_0$  Rydberg state ( $14(4)\mu\text{s}$ ) observed in Ref. [29]. Further refinement of the MQDT model for this series at low- $n$  will be useful to understand the lifetimes of this series quantitatively.

## 5. $^1D_2$ and $^3D_2$

Here, we present a five-channel MQDT model for the  $n^{1,3}D_2$  Rydberg states of  $^{174}\text{Yb}$ . We adapt this model from Ref. [49], but we refit the MQDT model parameters of the  $^1S_0$ ,  $^{1,3}D_2$ ,  $^{1,3}P_1$  Rydberg series in a simultaneous, 42-parameter fit to the previously measured [46, 49, 50, 53–56, 58] and newly measured data presented in the supplemental material [70]. The resulting MQDT models are presented in Tab. S1, Tab. S2, and Tab. S3.

In addition, to account for singlet-triplet mixing, the model includes a rotation around the  $^1D_2$  and  $^3D_2$  channels in the  $U_{i\alpha}$  matrix. To determine the magnitude of the singlet-triplet mixing, we use the  $g$ -factors of the  $n^{1,3}D_2$  Rydberg series and its perturbers measured by Zerne and co-workers [59] to obtain a value for the singlet-triplet mixing angle between the  $^1D_2$  and  $^3D_2$  channels. To that extent, we vary the energy-dependent mixing angle  $\theta_{12}$  (Eq. (A10)), and calculate the  $g$ -factor in using Eq. (22) of Ref. [44]. In addition, we treat the  $g$ -

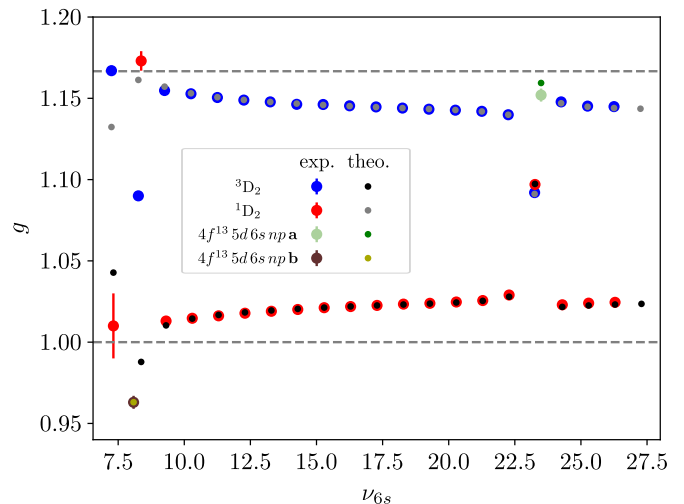


Figure 16.  $g$ -factors of the  $^{1,3}D_2$  and its perturbers as taken from Ref. [59] and calculated with the MQDT presented in Tab. S2. The gray dashed lines indicate the values for  $g$  factors in pure  $LS$  coupling.

Table I. Rydberg-Ritz expansion coefficients of the  $n^3D_1$  and  $n^3D_3$  Rydberg states of Yb, inferred from laser spectroscopy of D  $F = 3/2$  and  $F = 5/2$  Rydberg states of  $^{171}\text{Yb}$ .

	$n^3D_1$	$n^3D_3$
$\mu_0$	2.752 580 93	2.728 953 15
$\mu_2$	0.3826	-0.2065
$\mu_4$	-483.1	220.5

factors of the perturbing states with only partially known electronic configuration as parameters of our model. To obtain the best agreement between experiment and theory, we introduce an energy dependent mixing angle, as defined in Eq. (A10). The results of the fit are presented in Fig. 16 and the MQDT model is summarized in Tab. S2. From our MQDT model, we estimate a triplet character in the  $^1D_2$  series between 14.0% and 15.5% for  $30 \leq n \leq 100$ . This is in agreement with an estimated triplet admixture into the  $36^1D_2$  state of 19(6)% presented in Ref. [58].

## 6. $^3D_1$ and $^3D_3$

The  $^3D_1$  and  $^3D_3$  Rydberg states of  $^{174}\text{Yb}$  are not directly laser accessible by two-photon laser spectroscopy through the  $6s6p^1P_1$  intermediate state. A few  $^3D_1$  and  $^3D_3$  Rydberg states have been observed in Ref. [61] and Ref. [121]. For the purposes of this work, we infer the quantum defects of the  $^3D_1$  and  $^3D_3$  from laser accessible D  $F = 3/2$  and D  $F = 5/2$  Rydberg states in  $^{171}\text{Yb}$ , as discussed in App. E3.

The quantum defects of the two series are well described by a Rydberg-Ritz model

$$\mu(n) = \mu_0 + \frac{\mu_2}{(n - \mu_0)^2} + \frac{\mu_4}{(n - \mu_0)^4} \quad (\text{D1})$$

for the states studied in this work with  $\nu > 30$ . The obtained expansion coefficients for the two series are presented in Tab. I.

The inferred quantum defects for the  $n^3D_3$  Rydberg series, are consistent with the assignment of measurements in  $^{174}\text{Yb}$  presented in Ref. [61] to within the stated measurement uncertainties of 10 MHz. The inferred quantum defects for the  $n^3D_1$  Rydberg series are consistent with the assignment of measurements in  $^{174}\text{Yb}$  presented in Refs. [61, 121], but the Rydberg state energies deviate up to 40 MHz from the values presented in Ref. [61], which could be due to the limited number of D  $F = 3/2$  states with dominant  $^3D_1$  character observed in this work.

### Appendix E: Additional spectroscopic data and models for $^{171}\text{Yb}$

In this appendix, we give additional details about the spectroscopic measurements and MQDT model development for  $^{171}\text{Yb}$ .

#### 1. S $F = 1/2$ and $F = 3/2$ states

There is only a single  $F = 3/2$  series with  $L = 0$ , which converges to the  $F_c = 1$  threshold and has  $^3S_1$  character. We have measured the energy spacing between several S  $F = 3/2$  Rydberg states and S  $F = 1/2$  or D  $F = 5/2$  Rydberg states using microwave spectroscopy in an atomic beam. The experimental transition frequencies are presented in Tab. S29. Due to the small number of measured transitions to S  $F = 3/2$  Rydberg states, we model this series using the Rydberg-Ritz model introduced for  $^{174}\text{Yb}$  [29] with parameters optimized in the fit to the S  $F = 1/2$  Rydberg states (presented in Tab. S6). The experimental and theoretical energies of the S  $F = 3/2$  Rydberg series agree to within the uncertainty of the initial state energy used in the microwave spectroscopy.

In Fig. 5, we presented measurements of Stark shifts of S  $F = 1/2$  Rydberg states. Most Rydberg states exhibit a quadratic Stark shift at small electric fields, common for non-degenerate Rydberg states, and we extract a static polarizability by a quadratic fit to the observed Stark shift. However, for cases in which the Rydberg state of interest is very nearly degenerate with other Rydberg states (shaded gray in Fig. 5), the Stark shift is not quadratic even at very small electric fields. In Fig. 17, we present a field-dependent shift measurement together with a non-perturbative calculation, finding excellent agreement, highlighting the accuracy of the obtained Rydberg state energies and wavefunctions obtained by our MQDT treatment.

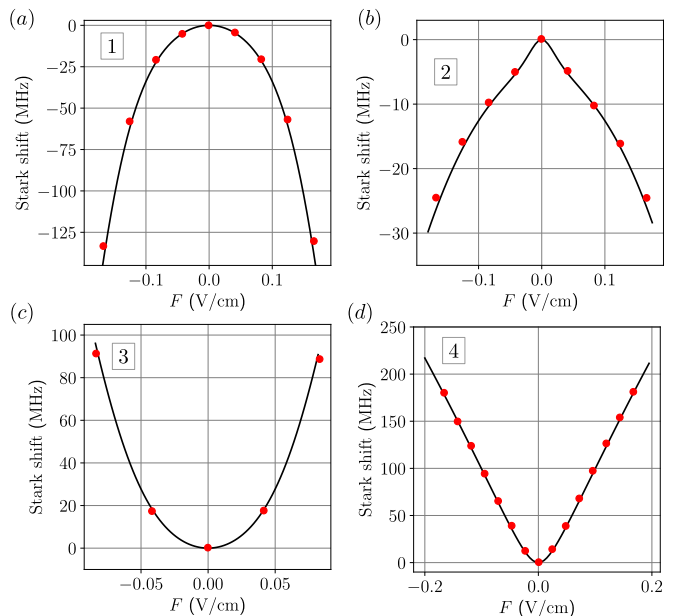


Figure 17. Experimental Stark shifts (red dots) of  $^{171}\text{Yb}$   $|\nu_{F_c=1}, L = 0, F = 1/2\rangle$  Rydberg states with (a)  $\nu_{F_c=1} \approx 65.68$ , (b)  $\nu_{F_c=1} \approx 66.68$ , (c)  $\nu_{F_c=1} \approx 67.68$ , (d)  $\nu_{F_c=1} \approx 64.09$  compared with theoretical Stark shifts (solid black line). The extracted experimental Stark shifts at low electric field are presented in subpanels Fig 5 (d) and (e) as indicated by labels 1 to 4.

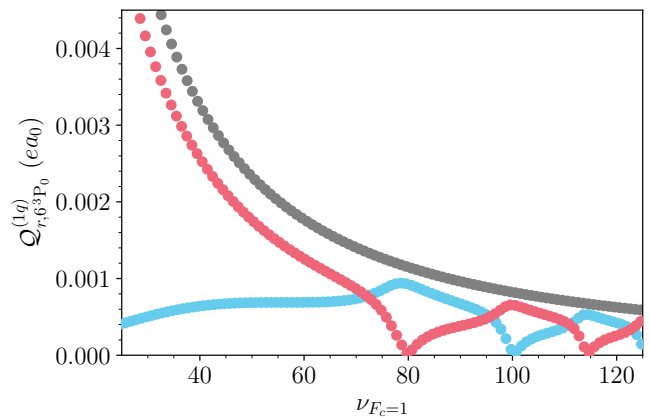


Figure 18. Transition dipole matrix elements  $Q_{r,6^3P_0}$  between the  $6s6p^3P_0(m_F = +1/2)$  metastable and Rydberg state  $r$ , where  $r = |\nu, L = 0, F = 3/2, m_F = +3/2\rangle$  (gray) and  $r = |\nu, L = 0, F = 1/2, m_F = -1/2\rangle$  (red and blue, color code as in Fig. 3).

Fig. 18 illustrates calculated transition dipole matrix elements from  $6s6p^3P_0$  metastable state into S ( $F = \{1/2, 3/2\}$ ) Rydberg states of  $^{171}\text{Yb}$ , which are computed using the single active electron approximation. The matrix elements to S ( $F = 1/2$ ) Rydberg states are generally smaller than the matrix elements to S ( $F = 3/2$ ) Rydberg states. However, at low effective principal quantum numbers, the transition dipole matrix element to one of

the two S ( $F = 1/2$ ) Rydberg series is still comparable to the S ( $F = 3/2$ ) case, due to a dominant triplet character. At larger effective principal quantum numbers, particularly close to near degeneracies between the two S ( $F = 1/2$ ) channels, the matrix elements varies strongly with the effective principal quantum number, indicating strong hyperfine-induced singlet-triplet mixing.

## 2. P $F = 1/2$ , $F = 3/2$ , and $F = 5/2$ states

Here, we introduce MQDT models for P  $F = 1/2$ ,  $F = 3/2$ , and  $F = 5/2$  Rydberg states of  $^{171}\text{Yb}$ . There are seven  $L = 1$  series in  $^{171}\text{Yb}$ . In  $LS$  coupling, they can be described as  $^3P_0(F = 1/2)$ ,  $^1P_1(F = \{1/2, 3/2\})$ ,  $^3P_1(F = \{1/2, 3/2\})$  and  $^3P_2(F = \{3/2, 5/2\})$ . As in the case of the  $|\nu, L = 0, F = 1/2\rangle$ , we use the  $^{174}\text{Yb}$  MQDT models of  $^{1,3}P_1$  and  $^3P_0$  (for  $F = 1/2$ ) and  $^{1,3}P_1$  and  $^3P_2$  (for  $F = 3/2$ ) as a basis for the  $^{171}\text{Yb}$  MQDT model and introduce the hyperfine coupling in the ion-core using a frame transformation (see App. A 2).

We optimize the MQDT model parameters for both the  $F = 1/2$  and  $F = 3/2$  series using a weighted, least-squared fitting procedure to a dataset containing Rydberg state energies obtained in this work from microwave spectroscopy (Tab. S30 and Tab. S33) and from previous laser spectroscopy reported Ref. [82] (Tab. S31 and Tab. S34). In our fitting procedure, we treat all the  $^{171}\text{Yb}$  MQDT model parameters originating from the same  $^{174}\text{Yb}$  MQDT models as a single parameter. For example, both the  $^{171}\text{Yb}$  P  $F = 1/2$  and P  $F = 3/2$  MQDT models contain a contribution from the  $^{1,3}P_1$  MQDT model developed for  $^{174}\text{Yb}$  in Appendix D 2. The resulting MQDT parameters for  $F = 1/2$  and  $F = 3/2$  are presented in the supplemental material [70].

The state energies reported in Tab. S31 and Tab. S34 are obtained from isotope shift and hyperfine splitting measurements of the  $n^1P_1$  and  $n^3P_{0,1,2}$  Rydberg states using three-photon laser spectroscopy, as presented in previous work [82] (reproduced in Tab. S36 and Tab. S37). The isotope shift and hyperfine splittings in Ref. [82] are given with respect to  $6snp^1P_1$  and  $6snp^3P_1$  Rydberg states of  $^{176}\text{Yb}$  (reproduced in Tab. S38). The absolute uncertainty of the  $^{176}\text{Yb}$  Rydberg state energies presented in Ref. [82] is stated to be 4 GHz, but we find that the stated (relative) hyperfine splittings are more precise. To remove systematic errors on the inferred absolute energies of the  $^{171}\text{Yb}$  P  $F = 1/2$  and  $F = 3/2$  Rydberg states, we introduce the following treatment.

For Rydberg states with principal quantum number  $n > 20$ , Ref. [82] reports a nearly constant isotope shift between  $^{1,3}P_1$  Rydberg states of  $^{174}\text{Yb}$  and  $^{176}\text{Yb}$ . For  $n > 20$  therefore choose to reference the hyperfine splittings against the accurate energies obtained from the  $^{174}\text{Yb}$   $^{1,3}P_1$  MQDT model presented in App. D 2. The remaining isotope shift between  $^{171}\text{Yb}$  and  $^{174}\text{Yb}$  Rydberg states are accounted for, by introducing a constant shift to inferred absolute energies in order to minimize the

deviations to absolute energies inferred from microwave intervals to the  $|\nu, L = 0, F = 1/2\rangle$  Rydberg states.

For low lying states  $^{1,3}P_1$  of  $^{174}\text{Yb}$ , we observe significant deviations between experimental and predicted energies for  $^{174}\text{Yb}$  (App. D 2). For  $n \leq 20$ , we therefore choose to infer absolute energies of the observed P Rydberg states in  $^{171}\text{Yb}$  by referencing the hyperfine splitting measurements to the observed absolute energies of  $^{176}\text{Yb}$ , as presented in Ref. [82] (reproduced in Tab. S38). When applying this treatment to Rydberg state with  $n > 20$ , we observe a systematic shift of the inferred energies compared to the more accurate absolute state energies obtained from microwave intervals to the  $|\nu, L = 0, F = 1/2\rangle$  Rydberg states. The mean deviation is approximately 1.4 GHz and is well within the 4 GHz uncertainty stated for the  $^{176}\text{Yb}$  term values reported in Ref. [82]. In an attempt to remove this systematic shift, we add a constant energy offset to all  $^{171}\text{Yb}$  P Rydberg states that were referenced to the  $^{176}\text{Yb}$  energies.

The resulting inferred absolute energies of  $|\nu, L = 1, F = 1/2\rangle$  and  $|\nu, L = 1, F = 3/2\rangle$  Rydberg states are presented in Tab. S31 and Tab. S34.

## 3. D $F = 1/2$ , $F = 3/2$ , $F = 5/2$ , and $F = 7/2$

There are eight  $L = 2$  series in  $^{171}\text{Yb}$ . In  $LS$  coupling, they can be described as  $^3D_1(F = \{1/2, 3/2\})$ ,  $^1D_2(F = \{3/2, 5/2\})$ ,  $^3D_2(F = \{3/2, 5/2\})$  and  $^3D_3(F = \{5/2, 7/2\})$ . In  $^{174}\text{Yb}$ , spin-orbit coupling mixes the two  $J = 2$  series as discussed in Section II; in  $^{171}\text{Yb}$ , hyperfine coupling additionally mixes the three  $F = 3/2$  series and the three  $F = 5/2$  series.

As in the case of the  $|\nu, L = 0, F = 1/2\rangle$  Rydberg states, we measure the energies of  $|\nu, L = 2, F = 3/2\rangle$  and  $|\nu, L = 2, F = 5/2\rangle$  Rydberg states by laser spectroscopy by a two-photon transition via the  $6s6p^1P_1(F = 3/2)$  intermediate state. Transition frequencies to all measured  $|\nu, L = 2, F = 3/2\rangle$  and  $|\nu, L = 2, F = 5/2\rangle$  states are summarized in the supplemental material [70] and plotted on a Lu-Fano-type plot in Fig. 19a.

We use a least-square procedure to obtain MQDT parameters for the  $F = 3/2$  and  $F = 5/2$  series. As in the case of the P Rydberg states, we treat the MQDT parameters that originate from the  $^{174}\text{Yb}$  models and occur in both the  $F = 3/2$  and  $F = 5/2$  MQDT models as a single parameter. The developed MQDT models describe both the Rydberg state energies and the measured  $g$ -factors (summarized in the supplemental material [70]) well over nearly the entire energy range. Significant deviations for both  $F = 3/2$  and  $F = 5/2$  occur towards low effective principal quantum numbers. These deviations could arise from unaccounted perturbers in the MQDT or from channel interactions with additional  $(F = 3/2)^e$  Rydberg series. In the case of  $F = 5/2$ , we additionally observe slight deviations between experiment and theory, that could be caused by uncompensated stray electric fields.

There is only a single D Rydberg series with  $F = 1/2$

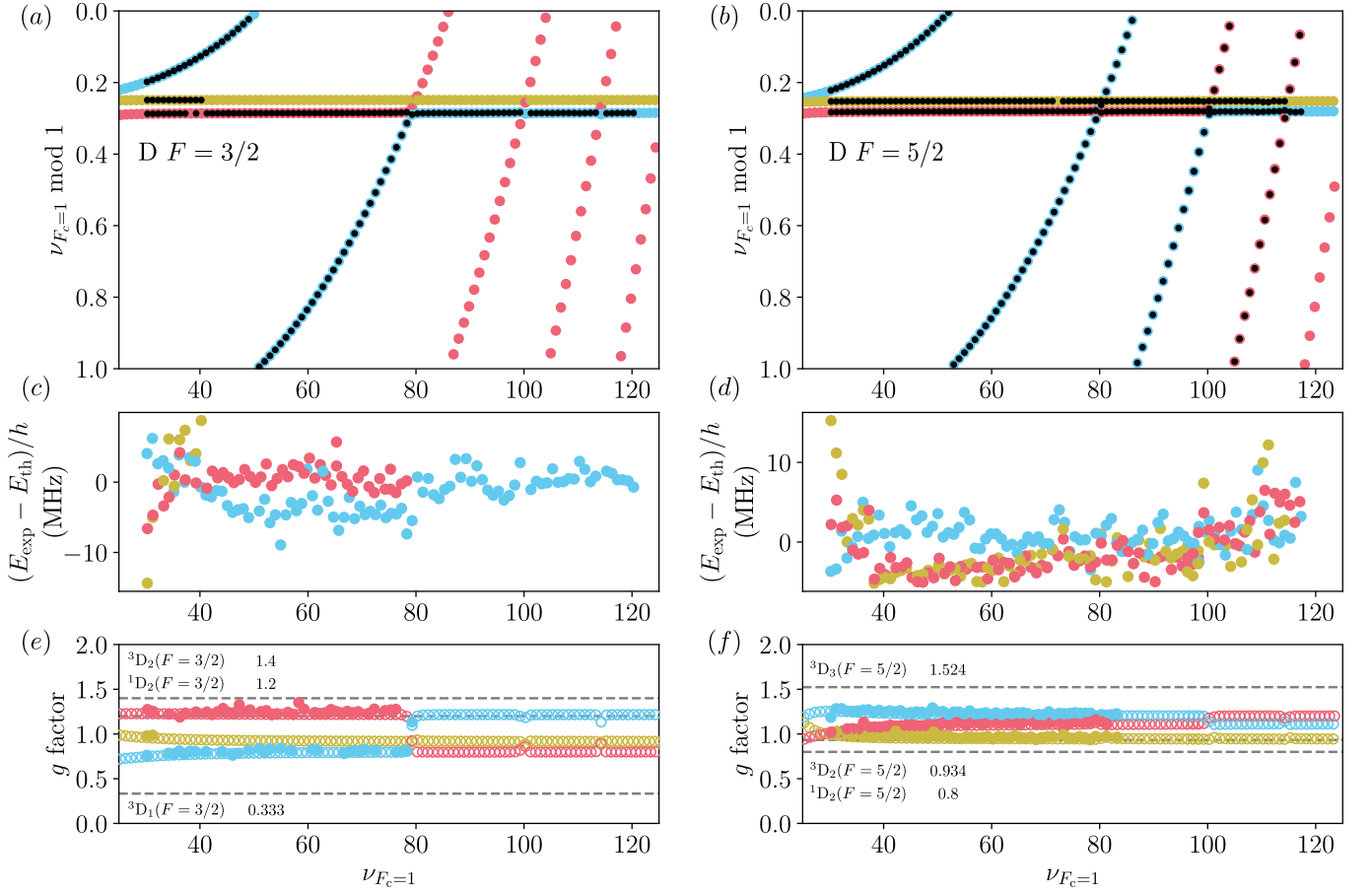


Figure 19. Lu-Fano-type plot of the  $^{171}\text{Yb}$  (a)  $|\nu, L = 2, F = 3/2\rangle$  and (b)  $|\nu, L = 2, F = 5/2\rangle$  Rydberg states. The experimentally observed Rydberg states are indicated by black dots and compared to theoretically obtained energies from the MQDT model (colored dots) presented in Tab. S9 and Tab. S10. (c) and (d) Deviations between the experimentally observed and theoretically calculated state energies. (e) and (f) Experimentally observed (full circles) and theoretically calculated  $g$ -factors of the  $|\nu, L = 2, F = 3/2\rangle$  and  $|\nu, L = 2, F = 5/2\rangle$  Rydberg states, respectively. Color coding as in (a) and (b). The gray dashed lines indicate the values of Landé  $g$  factors in pure  $LS$  coupling.

( $F = 7/2$ ), converging to the  $F_c = 1$  threshold with  $^3D_1$  ( $^3D_3$ ) character. Because we use the  $6s6p\ ^1P_1(F = 3/2)$  (dominantly singlet character) state as an intermediate state, the  $|\nu, L = 2, F = 1/2\rangle$  (dominantly triplet character) and the  $|\nu, L = 2, F = 7/2\rangle$  Rydberg states are inaccessible by direct laser spectroscopy. However, the fitted  $F = 3/2$  and  $F = 5/2$  series MQDT models include a Rydberg-Ritz model for the  $^3D_1$  and  $^3D_3$  series (Tab. S9 and Tab. S10). Therefore, we use this model to predict the positions of the  $F = 1/2$  and  $F = 7/2$  series.

#### Appendix F: Polarizability trends in $^{174}\text{Yb}$ and $^{171}\text{Yb}$ S Rydberg states

In Fig. 20 and Fig. 21 we present predicted polarizabilities for  $L = 0$  states of both  $^{174}\text{Yb}$  and  $^{171}\text{Yb}$ . We note several interesting features. First, the  $^{174}\text{Yb}$   $^3S_1$  polarizability is positive at low- $n$  and negative at high- $n$ , as the strongly perturbed  $^3P_0$  and  $^3P_1$  series cross the

$^3S_1$  series in energy. Second, the  $^{171}\text{Yb}$  polarizabilities have a much more complex behavior, with multiple sign changes resulting from a number of resonances.

#### Appendix G: Rydberg-Rydberg-interaction trends

The van der Waals coefficients  $C_6$  for the  $L = 0$  Rydberg states of  $^{174}\text{Yb}$  and  $^{171}\text{Yb}$  Rydberg states are presented in Fig. 22. In  $^{174}\text{Yb}$ , the  $C_6$  coefficients of  $6sns\ ^1S_0$  Rydberg series are unusually small, consistent with the single-channel calculations of Ref. [86] (we additionally note a Förster resonance around  $\nu \approx 50$ , which arises from the inclusion of singlet-triplet mixing in the  $^{1,3}P_1$  Rydberg series). Similar Förster resonances have also been predicted for  $^3D_2$  and  $^{1,3}F_3$  states of  $^{88}\text{Sr}$  [68]. In contrast, the  $C_6$  coefficients of  $6sns\ ^3S_1$  Rydberg states of  $^{174}\text{Yb}$  are larger, consistent with previous estimates [29] and observations [96], but calculated here for the first time. The  $C_6$  coefficients of this series are the same mag-

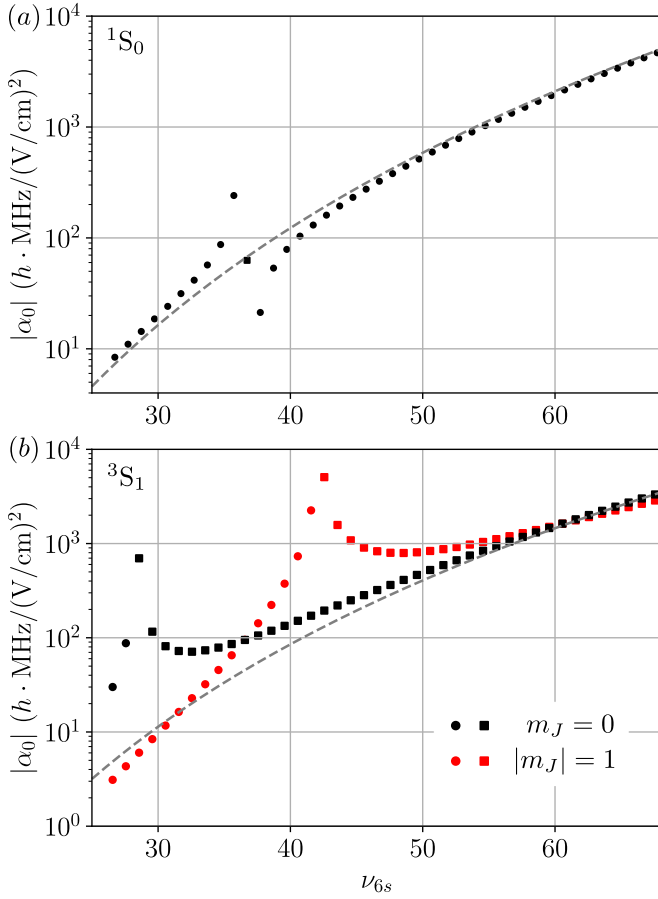


Figure 20. Predicted absolute static dipole polarizabilities of Rydberg series of  $^{174}\text{Yb}$  for (a)  $6sns\ ^1S_0$  and (b)  $6sns\ ^3S_1$ . Circles indicate positive values of  $\alpha_0$ , whereas squares indicate negative values of  $\alpha_0$ . The gray, dashed lines in (a) and (b) serve as a guide to the eye, indicating a  $\nu_{6s}^7$  scaling.

nitude as for the  $ns_{1/2}$  Rydberg states of rubidium, but with opposite sign (*i.e.*, attractive).

As in the case for  $^1S_0$  Rydberg states of  $^{174}\text{Yb}$ , the singlet connected  $|\nu, L=0, F=1/2\rangle$  Rydberg states of  $^{171}\text{Yb}$  (blue dots in Fig. 22) have small  $C_6$  coefficients in the range  $40 \leq \nu \leq 70$ . The the triplet connected  $|\nu, L=0, F=1/2, m_F\rangle$  states have  $C_6$  coefficients that are approximately half the magnitude of Rb, with the same sign (*i.e.*, repulsive).

As pointed out in Section IV,  $|\nu, L=0, F=3/2\rangle|\nu, L=0, F=3/2\rangle$  Rydberg pair states of  $^{171}\text{Yb}$  have small Förster defects over a large range of effective principal quantum number  $\nu$  (Fig. 23). It is surprising that the Förster defect is so small over such a large range of  $\nu$ , which results from a combination of series perturbors and hyperfine coupling. To calculate a meaningful asymptotic  $C_6$  coefficient, we calculate the pair potentials under a 30 G magnetic field to lift the degeneracy somewhat (Fig. 22c). The extracted  $C_6$  coefficients are not meaningful at short separations, which are dominated by resonant dipole-dipole interaction, as

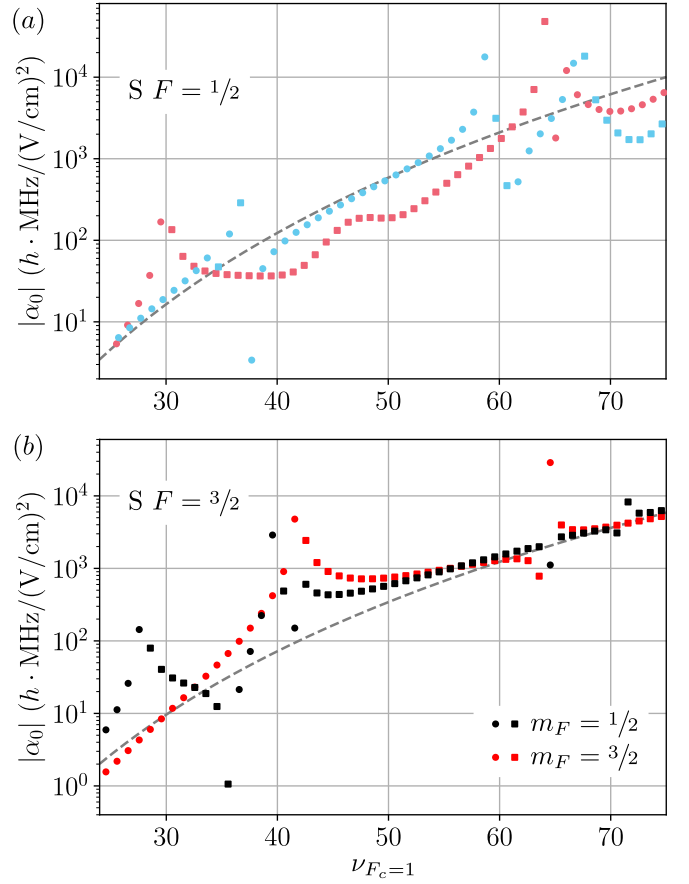


Figure 21. Predicted absolute static dipole polarizabilities of Rydberg series of  $^{171}\text{Yb}$  with (a)  $S F = 1/2$  (color code as in Fig. 3) and (b)  $S F = 3/2$ . Circles indicate positive values of  $\alpha_0$ , whereas squares indicate negative values of  $\alpha_0$ . The gray, dashed lines in (a) and (b) serve as a guide to the eye, indicating a  $\nu_{F_c=1}^7$  scaling.

shown in Fig. 7.

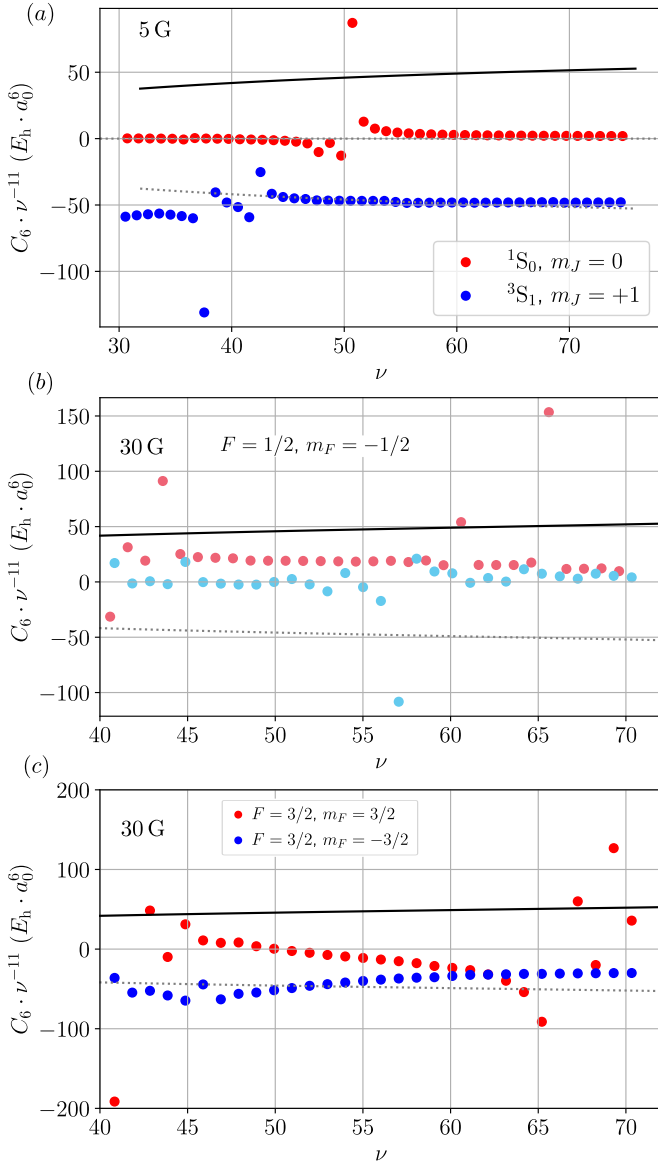


Figure 22. Predicted scaled  $C_6$  coefficients of (a)  $^{174}\text{Yb } ^1S_0$  (red dots) and  $^3S_1$  (blue dots) Rydberg states at a magnetic field of 5 G ( $\theta = \pi/2$ ), (b) and (c)  $^{171}\text{Yb } |\nu, L=0, F=1/2\rangle$  and  $|\nu, L=0, F=3/2\rangle$  Rydberg states at a magnetic field of 30 G ( $\theta = \pi/2$ ).  $\theta$  is the angle between the magnetic field and the inter-atomic axis. For comparison, the scaled  $C_6$  coefficients of  $n^2S_{1/2}$  Rydberg states of Rb are given by solid ( $C_6$ ) and dotted ( $-C_6$ ) black lines. The color code in (b) corresponds to the color code in Fig. 3.

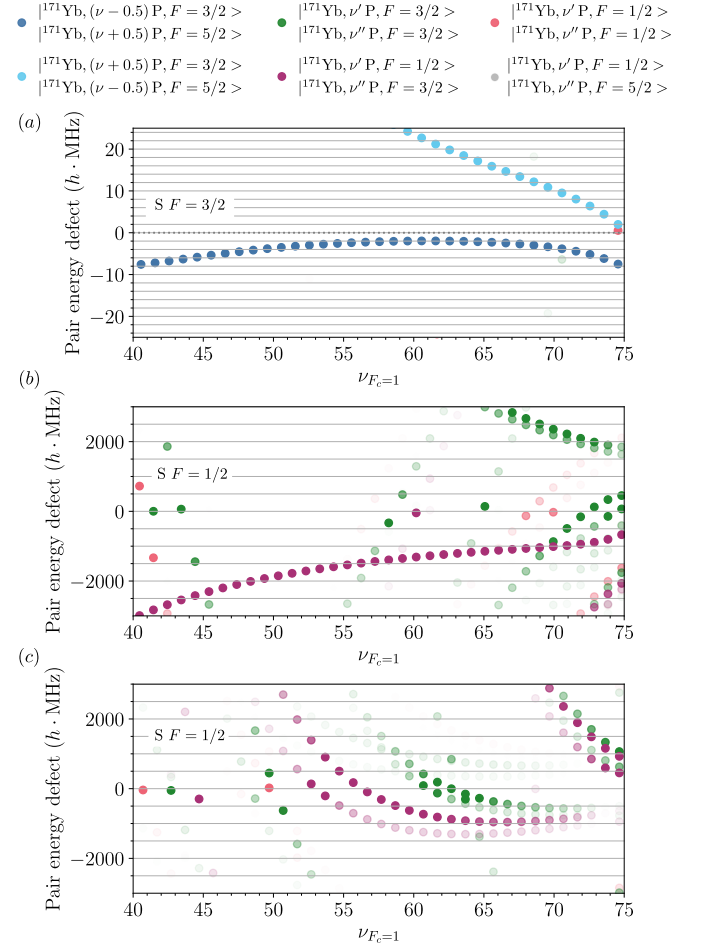


Figure 23.  $^{171}\text{Yb}$  pair energy defects between  $|\nu_{F_c=1}, L=0, F\rangle |\nu_{F_c=1}, L=0, F\rangle$  and the nearest dipole coupled  $|\nu_{F_c=1}, L=1, F\rangle |\nu_{F_c=1}, L=1, F'\rangle$  states for (a)  $F=3/2$ , and (b) and (c)  $F=1/2$ . The color of the markers indicates the combination of hyperfine states of the  $|\nu, L=1, F\rangle |\nu', L=1, F'\rangle$  pair state according to the legend. The opacity encodes  $\left(\frac{d_1 d_2}{\Delta E}\right)^2 \left(\frac{1}{\nu_{F_c=1}}\right)^8$ , where  $d_i$  are the dipole matrix elements between the involved Rydberg states and  $\Delta E$  corresponds to the pair defect.

- [1] H. Bernien, S. Schwartz, A. Keesling, H. Levine, A. Omran, H. Pichler, S. Choi, A. S. Zibrov, M. Endres, M. Greiner, V. Vuletić, and M. D. Lukin, Probing many-body dynamics on a 51-atom quantum simulator, *Nature* **551**, 579 (2017).
- [2] P. Scholl, M. Schuler, H. J. Williams, A. A. Eberharter, D. Barredo, K.-N. Schymik, V. Lienhard, L.-P. Henry, T. C. Lang, T. Lahaye, A. M. Läuchli, and A. Browaeys, Quantum simulation of 2D antiferromagnets with hundreds of Rydberg atoms, *Nature* **595**, 233 (2021).
- [3] D. Bluvstein, H. Levine, G. Semeghini, T. T. Wang, S. Ebadi, M. Kalinowski, A. Keesling, N. Maskara, H. Pichler, M. Greiner, V. Vuletić, and M. D. Lukin, A quantum processor based on coherent transport of entangled atom arrays, *Nature* **604**, 451 (2022).
- [4] W. J. Eckner, N. Darkwah Oppong, A. Cao, A. W. Young, W. R. Milner, J. M. Robinson, J. Ye, and A. M. Kaufman, Realizing spin squeezing with Rydberg interactions in an optical clock, *Nature* **621**, 734 (2023).
- [5] P. Goy, J. M. Raimond, G. Vitrant, and S. Haroche, Millimeter-wave spectroscopy in cesium Rydberg states. Quantum defects, fine- and hyperfine-structure measurements, *Phys. Rev. A* **26**, 2733 (1982).
- [6] K.-H. Weber and C. J. Sansonetti, Accurate energies of  $nS$ ,  $nP$ ,  $nD$ ,  $nF$ , and  $nG$  levels of neutral cesium, *Phys. Rev. A* **35**, 4650 (1987).
- [7] W. Li, I. Mourachko, M. W. Noel, and T. F. Gallagher, Millimeter-wave spectroscopy of cold Rb Rydberg atoms in a magneto-optical trap: Quantum defects of the  $ns$ ,  $np$ , and  $nd$  series, *Phys. Rev. A* **67**, 052502 (2003).
- [8] M. Mack, F. Karlewski, H. Hattermann, S. Höckh, F. Jessen, D. Cano, and J. Fortágh, Measurement of absolute transition frequencies of  $^{87}\text{Rb}$  to  $nS$  and  $nD$  Rydberg states by means of electromagnetically induced transparency, *Phys. Rev. A* **83**, 052515 (2011).
- [9] J. Han, Y. Jamil, D. V. L. Norum, P. J. Tanner, and T. F. Gallagher, Rb  $nf$  quantum defects from millimeter-wave spectroscopy of cold  $^{85}\text{Rb}$  Rydberg atoms, *Phys. Rev. A* **74**, 054502 (2006).
- [10] J. Deiglmayr, H. Herburger, H. Saßmannshausen, P. Jansen, H. Schmutz, and F. Merkt, Precision measurement of the ionization energy of Cs I, *Phys. Rev. A* **93**, 013424 (2016).
- [11] M. Peper, F. Helmrich, J. Butscher, J. A. Agner, H. Schmutz, F. Merkt, and J. Deiglmayr, Precision measurement of the ionization energy and quantum defects of  $^{39}\text{K}$  I, *Phys. Rev. A* **100**, 012501 (2019).
- [12] M. L. Zimmerman, M. G. Littman, M. M. Kash, and D. Kleppner, Stark structure of the Rydberg states of alkali-metal atoms, *Phys. Rev. A* **20**, 2251 (1979).
- [13] C. E. Theodosiou, Lifetimes of alkali-metal—atom Rydberg states, *Phys. Rev. A* **30**, 2881 (1984).
- [14] J. Deiglmayr, Long-range interactions between Rydberg atoms, *Phys. Scr.* **91**, 104007 (2016).
- [15] L. Béguin, A. Vernier, R. Chicireanu, T. Lahaye, and A. Browaeys, Direct Measurement of the van der Waals Interaction between Two Rydberg Atoms, *Phys. Rev. Lett.* **110**, 263201 (2013).
- [16] S. Ravets, H. Labuhn, D. Barredo, T. Lahaye, and A. Browaeys, Measurement of the angular dependence of the dipole-dipole interaction between two individual Rydberg atoms at a Förster resonance, *Phys. Rev. A* **92**, 020701(R) (2015).
- [17] S. Anand, C. E. Bradley, R. White, V. Ramesh, K. Singh, and H. Bernien, A dual-species Rydberg array (2024), arXiv:2401.10325 [quant-ph].
- [18] W. P. Spencer, A. G. Vaidyanathan, D. Kleppner, and T. W. Ducas, Measurements of lifetimes of sodium Rydberg states in a cooled environment, *Phys. Rev. A* **24**, 2513 (1981).
- [19] W. P. Spencer, A. G. Vaidyanathan, D. Kleppner, and T. W. Ducas, Temperature dependence of blackbody-radiation-induced transfer among highly excited states of sodium, *Phys. Rev. A* **25**, 380 (1982).
- [20] H. Bergström, C. Levinson, and H. Lundberg, Natural radiative lifetimes in the  $5snd\ ^1D_2$  series of Sr I, *Z. Phys. D* **2**, 127 (1986).
- [21] C. Boisseau, I. Simbotin, and R. Côté, Macrodimers: Ultralong Range Rydberg Molecules, *Phys. Rev. Lett.* **88**, 133004 (2002).
- [22] K. R. Overstreet, A. Schwettmann, J. Tallant, D. Booth, and J. P. Shaffer, Observation of electric-field-induced Cs Rydberg atom macrodimers, *Nat. Phys* **5**, 581 (2009).
- [23] H. Saßmannshausen and J. Deiglmayr, Observation of Rydberg-Atom Macrodimers: Micrometer-Sized Diatomic Molecules, *Phys. Rev. Lett.* **117**, 083401 (2016).
- [24] S. Hollerith, J. Zeiher, J. Rui, A. Rubio-Abadal, V. Walther, T. Pohl, D. M. Stamper-Kurn, I. Bloch, and C. Gross, Quantum gas microscopy of Rydberg macrodimers, *Science* **364**, 664 (2019).
- [25] A. Cooper, J. P. Covey, I. S. Madjarov, S. G. Porsev, M. S. Safronova, and M. Endres, Alkaline-Earth Atoms in Optical Tweezers, *Phys. Rev. X* **8**, 041055 (2018).
- [26] M. A. Norcia, A. W. Young, and A. M. Kaufman, Microscopic Control and Detection of Ultracold Strontium in Optical-Tweezer Arrays, *Phys. Rev. X* **8**, 041054 (2018).
- [27] R. C. Teixeira, A. Larrouy, A. Muni, L. Lachaud, J.-M. Raimond, S. Gleyzes, and M. Brune, Preparation of Long-Lived, Non-Autoionizing Circular Rydberg States of Strontium, *Phys. Rev. Lett.* **125**, 263001 (2020).
- [28] C. Hölzl, A. Götzelmann, E. Pultinevicius, M. Wirth, and F. Meinert, Long-Lived Circular Rydberg Qubits of Alkaline-Earth Atoms in Optical Tweezers (2024), arXiv:2401.10625 [physics.atom-ph].
- [29] J. T. Wilson, S. Saskin, Y. Meng, S. Ma, R. Dilip, A. P. Burgers, and J. D. Thompson, Trapping Alkaline Earth Rydberg Atoms Optical Tweezer Arrays, *Phys. Rev. Lett.* **128**, 033201 (2022).
- [30] A. Jenkins, J. W. Lis, A. Senoo, W. F. McGrew, and A. M. Kaufman, Ytterbium Nuclear-Spin Qubits in an Optical Tweezer Array, *Phys. Rev. X* **12**, 021027 (2022).
- [31] S. Ma, A. P. Burgers, G. Liu, J. Wilson, B. Zhang, and J. D. Thompson, Universal Gate Operations on Nuclear Spin Qubits in an Optical Tweezer Array of  $^{171}\text{Yb}$  Atoms, *Phys. Rev. X* **12**, 021028 (2022).
- [32] W. Huie, L. Li, N. Chen, X. Hu, Z. Jia, W. K. C. Sun, and J. P. Covey, Repetitive Readout and Real-Time Control of Nuclear Spin Qubits in  $^{171}\text{Yb}$  Atoms, *PRX Quantum* **4**, 030337 (2023).
- [33] P. Scholl, A. L. Shaw, R. B.-S. Tsai, R. Finkelstein, J. Choi, and M. Endres, Erasure conversion in a high-fidelity Rydberg quantum simulator, *Nature* **622**, 273

- (2023).
- [34] A. L. Shaw, Z. Chen, J. Choi, D. K. Mark, P. Scholl, R. Finkelstein, A. Elben, S. Choi, and M. Endres, Benchmarking highly entangled states on a 60-atom analogue quantum simulator, *Nature* **628**, 71 (2024).
- [35] R. Finkelstein, R. B.-S. Tsai, X. Sun, P. Scholl, S. Direkci, T. Gefen, J. Choi, A. L. Shaw, and M. Endres, Universal quantum operations and ancilla-based readout for tweezer clocks (2024), arXiv:2402.16220 [quant-ph].
- [36] A. Cao, W. J. Eckner, T. Lukin Yelin, A. W. Young, S. Jandura, L. Yan, K. Kim, G. Pupillo, J. Ye, N. Darkwah Oppong, and A. M. Kaufman, Multi-qubit gates and 'Schrödinger cat' states in an optical clock (2024), arXiv:2402.16289 [quant-ph].
- [37] J. W. Lis, A. Senoo, W. F. McGrew, F. Rönchen, A. Jenkins, and A. M. Kaufman, Midcircuit Operations Using the *omg* Architecture in Neutral Atom Arrays, *Phys. Rev. X* **13**, 041035 (2023).
- [38] M. A. Norcia, W. B. Cairncross, K. Barnes, P. Battaglino, A. Brown, M. O. Brown, K. Cassella, C.-A. Chen, R. Coxe, D. Crow, J. Epstein, C. Griger, A. M. W. Jones, H. Kim, J. M. Kindem, J. King, S. S. Kondov, K. Kotru, J. Lauigan, M. Li, M. Lu, E. Megidish, J. Marjanovic, M. McDonald, T. Mittiga, J. A. Mumiz, S. Narayanaswami, C. Nishiguchi, R. Notermans, T. Paule, K. A. Pawlak, L. S. Peng, A. Ryou, A. Smull, D. Stack, M. Stone, A. Sucich, M. Urbanek, R. J. M. van de Veerdonk, Z. Vendeiro, T. Wilkason, T.-Y. Wu, X. Xie, X. Zhang, and B. J. Bloom, Midcircuit Qubit Measurement and Rearrangement in a  $^{171}\text{Yb}$  Atomic Array, *Phys. Rev. X* **13**, 041034 (2023).
- [39] Y. Wu, S. Kolkowitz, S. Puri, and J. D. Thompson, Erasure conversion for fault-tolerant quantum computing in alkaline earth Rydberg atom arrays, *Nat. Commun.* **13**, 4657 (2022).
- [40] S. Ma, G. Liu, P. Peng, B. Zhang, S. Jandura, J. Claes, A. P. Burgers, G. Pupillo, S. Puri, and J. D. Thompson, High-fidelity gates and mid-circuit erasure conversion in an atomic qubit, *Nature* **622**, 279 (2023).
- [41] M. J. Seaton, Quantum defect theory I. General formulation, *Proc. Phys. Soc. (London)* **88**, 801 (1966).
- [42] U. Fano, Quantum Defect Theory of  $l$  Uncoupling in  $\text{H}_2$  as an Example of Channel-Interaction Treatment, *Phys. Rev. A* **2**, 353 (1970).
- [43] C. L. Vaillant, M. P. A. Jones, and R. M. Potvliege, Multichannel quantum defect theory of strontium bound Rydberg states, *J. Phys. B: At., Mol. Opt. Phys.* **47**, 155001 (2014).
- [44] F. Robicheaux, D. W. Booth, and M. Saffman, Theory of long-range interactions for Rydberg states attached to hyperfine-split cores, *Phys. Rev. A* **97**, 022508 (2018).
- [45] E. Robertson, N. Šibalić, R. Potvliege, and M. Jones, ARC 3.0: An expanded Python toolbox for atomic physics calculations, *Comput. Phys. Commun.* **261**, 107814 (2021).
- [46] M. Aymar, A. Débarre, and O. Robaux, Highly excited levels of neutral ytterbium. II. Multichannel quantum defect analysis of odd- and even-parity spectra, *J. Phys. B: At. Mol. Phys.* **13**, 1089 (1980).
- [47] M. Aymar, Multichannel-quantum-defect theory wave functions of Ba tested or improved by laser measurements, *J. Opt. Soc. Am. B* **1**, 239 (1984).
- [48] R. Ali, M. Yaseen, A. Nadeem, S. A. Bhatti, and M. A. Baig, Two-colour three-photon excitation of the  $6snp$   $^1P_1$ ,  $^3P_{1,2}$  Rydberg levels of Yb I, *J. Phys. B: At., Mol. Opt. Phys.* **32**, 953 (1999).
- [49] H. Lehec, A. Zuliani, W. Mainault, E. Luc-Koenig, P. Pillet, P. Cheinet, F. Niyaz, and T. F. Gallagher, Laser and microwave spectroscopy of even-parity Rydberg states of neutral ytterbium and multichannel-quantum-defect-theory analysis, *Phys. Rev. A* **98**, 062506 (2018).
- [50] H. Lehec, *Spectroscopie Rydberg et excitation du coeur isolé d'atomes d'ytterbium ultra-froids*, Ph.D. thesis, Université Paris Saclay (COMUE) (2017).
- [51] R. Ding, J. D. Whalen, S. K. Kanungo, T. C. Killian, F. B. Dunning, S. Yoshida, and J. Burgdörfer, Spectroscopy of  $^{87}\text{Sr}$  triplet Rydberg states, *Phys. Rev. A* **98**, 042505 (2018).
- [52] F. Robicheaux, Calculations of long range interactions for  $^{87}\text{Sr}$  Rydberg states, *J. Phys. B: At., Mol. Opt. Phys.* **52**, 244001 (2019).
- [53] P. Camus and F. S. Tomkins, Spectre d'absorption de Yb I, *J. Physique* **30**, 545 (1969).
- [54] W. F. Meggers and J. L. Tech, The First Spectrum of Ytterbium (Yb I), *J. Res. NBS* **83**, 13 (1977).
- [55] P. Camus, A. Débarre, and C. Morillon, Highly excited levels of neutral ytterbium. I. Two-photon and two-step spectroscopy of even spectra, *J. Phys. B: At. Mol. Phys.* **13**, 1073 (1980).
- [56] M. Aymar, R. J. Champeau, C. Delsart, and O. Robaux, Three-step laser spectroscopy and multichannel quantum defect analysis of odd-parity Rydberg states of neutral ytterbium, *J. Phys. B: At. Mol. Phys.* **17**, 3645 (1984).
- [57] J. Neukammer, H. Rinneberg, and U. Majewski, Diamagnetic shift and singlet-triplet mixing of  $6snp$  Yb Rydberg states with large radial extent, *Phys. Rev. A* **30**, 1142 (1984).
- [58] H. Maeda, Y. Matsuo, M. Takami, and A. Suzuki, Optical-microwave double-resonance spectroscopy of highly excited Rydberg states of ytterbium, *Phys. Rev. A* **45**, 1732 (1992).
- [59] R. Zerne, L. Caiyan, J. Zhankui, and J. Larsson, Landé  $g_J$  factor measurements in the  $6snd$   $^{1,3}D_2$  sequences of Yb I, *Z. Phys. D* **37**, 259 (1996).
- [60] F. Niyaz, J. Nunkaew, and T. F. Gallagher, Microwave spectroscopy of the Yb  $6s(n+3)d \rightarrow 6sng$ ,  $6snh$ , and  $6sni$  transitions, *Phys. Rev. A* **99**, 042507 (2019).
- [61] D. Okuno, Y. Nakamura, T. Kusano, Y. Takasu, N. Takei, H. Konishi, and Y. Takahashi, High-resolution Spectroscopy and Single-photon Rydberg Excitation of Reconfigurable Ytterbium Atom Tweezer Arrays Utilizing a Metastable State, *J. Phys. Soc. Japan* **91**, 084301 (2022).
- [62] K. T. Lu, Spectroscopy and Collision Theory. The Xe Absorption Spectrum, *Phys. Rev. A* **4**, 579 (1971).
- [63] K. Barnes, P. Battaglino, B. J. Bloom, K. Cassella, R. Coxe, N. Crisosto, J. P. King, S. S. Kondov, K. Kotru, S. C. Larsen, J. Lauigan, B. J. Lester, M. McDonald, E. Megidish, S. Narayanaswami, C. Nishiguchi, R. Notermans, L. S. Peng, A. Ryou, T.-Y. Wu, and M. Yarwood, Assembly and coherent control of a register of nuclear spin qubits, *Nat. Commun.* **13**, 2779 (2022).
- [64] J. Hostetter, J. D. Pritchard, J. E. Lawler, and M. Saffman, Measurement of holmium Rydberg series through magneto-optical trap depletion spectroscopy, *Phys. Rev. A* **91**, 012507 (2015).
- [65] A. Trautmann, M. J. Mark, P. Ilzhöfer, H. Edri, A. E. Arach, J. G. Maloberti, C. H. Greene, F. Robicheaux, and

- F. Ferlino, Spectroscopy of Rydberg states in erbium using electromagnetically induced transparency, *Phys. Rev. Res.* **3**, 033165 (2021).
- [66] M. J. Seaton, Quantum defect theory, *Rep. Prog. Phys.* **46**, 167 (1983).
- [67] W. E. Cooke and C. L. Cromer, Multichannel quantum-defect theory and an equivalent N-level system, *Phys. Rev. A* **32**, 2725 (1985).
- [68] C. L. Vaillant, R. M. Potvliege, and M. P. A. Jones, Intercombination effects in resonant energy transfer, *Phys. Rev. A* **92**, 042705 (2015).
- [69] T. F. Gallagher, *Rydberg Atoms*, Cambridge Monographs on Atomic, Molecular and Chemical Physics (Cambridge University Press, 1994).
- [70] See Supplemental Material at [URL will be inserted by publisher] for tables of the developed MQDT models and tables of previous [12, 46, 48–50, 53–56, 58, 59, 82, 122–124] and new spectroscopic data used in the fitting and testing of the MQDT models.
- [71] R. Beigang, W. Makat, A. Timmermann, and P. J. West, Hyperfine-Induced  $n$  Mixing in High Rydberg States of  $^{87}\text{Sr}$ , *Phys. Rev. Lett.* **51**, 771 (1983).
- [72] J.-Q. Sun and K. T. Lu, Hyperfine structure of extremely high Rydberg  $msns$   $^1S_0$  and  $msns$   $^3S_1$  series in odd alkaline-earth isotopes, *J. Phys. B: At., Mol. Opt. Phys.* **21**, 1957 (1988).
- [73] H. J. Wörner, U. Hollenstein, and F. Merkt, Multichannel quantum defect theory and high-resolution spectroscopy of the hyperfine structure of high Rydberg states of  $^{83}\text{Kr}$ , *Phys. Rev. A* **68**, 032510 (2003).
- [74] M. Saffman, Quantum computing with atomic qubits and Rydberg interactions: progress and challenges, *J. Phys. B: At., Mol. Opt. Phys.* **49**, 202001 (2016).
- [75] R. Blatt, H. Schnatz, and G. Werth, Precise Determination of the  $^{171}\text{Yb}^+$  Ground State Hyperfine Separation, *Z. Phys. A - Atoms and Nuclei* **312**, 143 (1983).
- [76] P. Liao, R. Freeman, R. Panock, and L. Humphrey, Hyperfine-induced singlet-triplet mixing in  $^3\text{He}$ , *Opt. Commun.* **34**, 195 (1980).
- [77] J.-Q. Sun, Multichannel quantum defect theory of the hyperfine structure of high Rydberg states, *Phys. Rev. A* **40**, 7355 (1989).
- [78] J.-Q. Sun, K. T. Lu, and R. Beigang, Hyperfine structure of extremely high Rydberg  $msnd$   $^1D_2$ ,  $^3D_1$ ,  $^3D_2$  and  $^3D_3$  series in odd alkaline-earth isotopes, *J. Phys. B: At., Mol. Opt. Phys.* **22**, 2887 (1989).
- [79] J. Neukammer and H. Rinneberg, Hyperfine structure of perturbed  $6sns$   $^3S_1$  Rydberg states of barium, *J. Phys. B: At. Mol. Phys.* **15**, L425 (1982).
- [80] L. Barbier and R.-J. Champeau, Very high resolution study of high Rydberg levels of the configurations  $4f^{14}6snd$  of Yb I, *J. Physique* **41**, 947 (1980).
- [81] U. Majewski, J. Neukammer, and H. Rinneberg, High-Resolution Three-Photon Spectroscopy of  $6s15p^{1,3}P_1$  Rydberg States of Yb, *Phys. Rev. Lett.* **51**, 1340 (1983).
- [82] U. Majewski, *"Hochauflösende Laserspektroskopie von Ytterbium-Rydbergzuständen"*, Diploma thesis, Freie Universität Berlin (1985).
- [83] S. Weber, C. Tresp, H. Menke, A. Urvoy, O. Firstenberg, H. P. Büchler, and S. Hofferberth, Calculation of Rydberg interaction potentials, *J. Phys. B: At., Mol. Opt. Phys.* **50**, 133001 (2017).
- [84] N. Šibalić, J. Pritchard, C. Adams, and K. Weatherill, ARC: An open-source library for calculating properties of alkali Rydberg atoms, *Comput. Phys. Commun.* **220**, 319 (2017).
- [85] B. Vermersch, Anisotropy and state mixing in the interactions between Rydberg states, *Eur. Phys. J.: Spec. Top.* **225**, 2977 (2016).
- [86] C. L. Vaillant, M. P. A. Jones, and R. M. Potvliege, Long-range Rydberg–Rydberg interactions in calcium, strontium and ytterbium, *J. Phys. B: At., Mol. Opt. Phys.* **45**, 135004 (2012).
- [87] I. I. Beterov and M. Saffman, Rydberg blockade, Förster resonances, and quantum state measurements with different atomic species, *Phys. Rev. A* **92**, 042710 (2015).
- [88] J. T. Young, P. Bienias, R. Belyansky, A. M. Kaufman, and A. V. Gorshkov, Asymmetric Blockade and Multiqubit Gates via Dipole-Dipole Interactions, *Phys. Rev. Lett.* **127**, 120501 (2021).
- [89] A. Derevianko, P. Kómár, T. Topcu, R. M. Kroeze, and M. D. Lukin, Effects of molecular resonances on Rydberg blockade, *Phys. Rev. A* **92**, 063419 (2015).
- [90] H. Levine, A. Keesling, G. Semeghini, A. Omran, T. T. Wang, S. Ebadi, H. Bernien, M. Greiner, V. Vuletić, H. Pichler, and M. D. Lukin, Parallel Implementation of High-Fidelity Multiqubit Gates with Neutral Atoms, *Phys. Rev. Lett.* **123**, 170503 (2019).
- [91] S. Jandura and G. Pupillo, Time-Optimal Two- and Three-Qubit Gates for Rydberg Atoms, *Quantum* **6**, 712 (2022).
- [92] S. J. Evered, D. Bluvstein, M. Kalinowski, S. Ebadi, T. Manovitz, H. Zhou, S. H. Li, A. A. Geim, T. T. Wang, N. Maskara, H. Levine, G. Semeghini, G. Greiner, G. Vuletić, and M. D. Lukin, High-fidelity parallel entangling gates on a neutral atom quantum computer, *Nature* **622**, 268 (2023).
- [93] E. Knill, D. Leibfried, R. Reichle, J. Britton, R. B. Blakestad, J. D. Jost, C. Langer, R. Ozeri, S. Seidelin, and D. J. Wineland, Randomized benchmarking of quantum gates, *Phys. Rev. A* **77**, 012307 (2008).
- [94] G. Lochead, D. Boddy, D. P. Sadler, C. S. Adams, and M. P. A. Jones, Number-resolved imaging of excited-state atoms using a scanning autoionization microscope, *Phys. Rev. A* **87**, 053409 (2013).
- [95] I. S. Madjarov, J. P. Covey, A. L. Shaw, J. Choi, A. Kale, A. Cooper, H. Pichler, V. Schkolnik, J. R. Williams, and M. Endres, High-fidelity entanglement and detection of alkaline-earth Rydberg atoms, *Nat. Phys.* **16**, 857 (2020).
- [96] A. P. Burgers, S. Ma, S. Saskin, J. Wilson, M. A. Alarcón, C. H. Greene, and J. D. Thompson, Controlling Rydberg Excitations Using Ion-Core Transitions in Alkaline-Earth Atom-Tweezer Arrays, *PRX Quantum* **3**, 020326 (2022).
- [97] K.-L. Pham, T. F. Gallagher, P. Pillet, S. Lepoutre, and P. Cheinet, Coherent Light Shift on Alkaline-Earth Rydberg Atoms from Isolated Core Excitation without Autoionization, *PRX Quantum* **3**, 020327 (2022).
- [98] A. D. Ludlow, M. M. Boyd, J. Ye, E. Peik, and P. O. Schmidt, Optical atomic clocks, *Rev. Mod. Phys.* **87**, 637 (2015).
- [99] V. D. Ovsiannikov, A. Derevianko, and K. Gibble, Rydberg Spectroscopy in an Optical Lattice: Blackbody Thermometry for Atomic Clocks, *Phys. Rev. Lett.* **107**, 093003 (2011).
- [100] C.-M. Lee and K. T. Lu, Spectroscopy and Collision Theory. II. the Ar Absorption Spectrum, *Phys. Rev. A* **8**, 1241 (1973).
- [101] M. Aymar, O. Robaux, and C. Thomas, Theoretical in-

- vestigations on the bound odd-parity spectrum of neutral krypton, *J. Phys. B: At. Mol. Phys.* **14**, 4255 (1981).
- [102] M. Schäfer, M. Raunhardt, and F. Merkt, Millimeter-wave spectroscopy and multichannel quantum-defect-theory analysis of high Rydberg states of xenon: The hyperfine structure of  $^{129}\text{Xe}^+$  and  $^{131}\text{Xe}^+$ , *Phys. Rev. A* **81**, 032514 (2010).
- [103] R. Beigang, K. Lücke, D. Schmidt, A. Timmermann, and P. West, One-photon laser spectroscopy of Rydberg series from metastable levels in calcium and strontium, *Phys. Scr.* **26**, 183 (1982).
- [104] H. Rinneberg and J. Neukammer, Hyperfine structure and three-channel quantum-defect theory of  $6snd^1D_2$  Rydberg states of Ba, *Phys. Rev. A* **27**, 1779 (1983).
- [105] M. Aymar, Rydberg series of alkaline-earth atoms Ca through Ba. the interplay of laser spectroscopy and multichannel quantum defect analysis, *Phys. Rep.* **110**, 163 (1984).
- [106] S. Bhattacharyya, M. A. N. Razvi, S. Cohen, and S. G. Nakhate, Odd-parity  $J = 11/2$  autoionizing Rydberg series of europium below the  $5d^9D_4$  threshold: Spectroscopy and multichannel quantum-defect-theory analysis, *Phys. Rev. A* **76**, 012502 (2007).
- [107] A. Osterwalder, A. Wüest, F. Merkt, and C. Jungen, High-resolution millimeter wave spectroscopy and multichannel quantum defect theory of the hyperfine structure in high Rydberg states of molecular hydrogen  $\text{H}_2$ , *J. Chem. Phys.* **121**, 11810 (2004).
- [108] D. Sprecher, C. Jungen, and F. Merkt, Determination of the binding energies of the  $np$  Rydberg states of  $\text{H}_2$ , HD, and  $\text{D}_2$  from high-resolution spectroscopic data by multichannel quantum-defect theory, *J. Chem. Phys.* **140**, 104303 (2014).
- [109] rydcalc, <https://github.com/ThompsonLabPrinceton/rydcalc>.
- [110] C. H. Greene and M. Aymar, Spin-orbit effects in the heavy alkaline-earth atoms, *Phys. Rev. A* **44**, 1773 (1991).
- [111] A. R. Edmonds, *Angular momentum in quantum mechanics*, 4th ed. (Princeton University Press, Princeton, 1996).
- [112] O. Robaux and M. Aymar, A program for analysing the Rydberg series of highly excited discrete spectra by M.Q.D.T., *Comput. Phys. Commun.* **25**, 223 (1982).
- [113] R. R. Freeman and D. Kleppner, Core polarization and quantum defects in high-angular-momentum states of alkali atoms, *Phys. Rev. A* **14**, 1614 (1976).
- [114] S. A. Bhatti, C. L. Cromer, and W. E. Cooke, Analysis of the Rydberg character of the  $5d7d^1D_2$  state of barium, *Phys. Rev. A* **24**, 161 (1981).
- [115] F. A. Jenkins and E. Segrè, The Quadratic Zeeman Effect, *Phys. Rev.* **55**, 52 (1939).
- [116] K. Singer, M. Reetz-Lamour, T. Amthor, S. Fölling, M. Tschernack, and M. Weidemüller, Spectroscopy of an ultracold Rydberg gas and signatures of Rydberg–Rydberg interactions, *J. Phys. B: At., Mol. Opt. Phys.* **38**, S321 (2005).
- [117] M. E. Rose, The electrostatic interaction of two arbitrary charge distributions, *J. Math. and Phys.* **37** (1958).
- [118] A. Dalgarno and W. Davison, *The Calculation of Van Der Waals Interactions* (Academic Press, 1966) pp. 1–32.
- [119] M. Kleinert, M. E. Gold Dahl, and S. Bergeson, Measurement of the Yb I  $^1S_0-^1P_1$  transition frequency at 399 nm using an optical frequency comb, *Phys. Rev. A* **94**, 052511 (2016).
- [120] I. I. Beterov, I. I. Ryabtsev, D. B. Tretyakov, and V. M. Entin, Quasiclassical calculations of blackbody-radiation-induced depopulation rates and effective lifetimes of Rydberg  $ns$ ,  $np$ , and  $nd$  alkali-metal atoms with  $n \leq 80$ , *Phys. Rev. A* **79**, 052504 (2009).
- [121] J. T. Wilson, *New tools for quantum science in Yb Rydberg atom arrays*, Ph.D. thesis, Princeton University (2022).
- [122] W. C. Martin, R. Zalubas, and L. Hagan, Atomic Energy Levels: The Rare Earth Elements, *Nat. Stand. Ref. Data Ser., NSRDS-NBS* **60**, 10.6028/NBS.NSRDS.60 (1978).
- [123] W. Bi-ru, Z. You-feng, X. Yun-fei, P. Li-gang, L. Ji, and Z. Jian-wei, The  $6snp^3P_{0,2}$  Rydberg series of neutral ytterbium, *J. Phys. B: At., Mol. Opt. Phys.* **24**, 49 (1991).
- [124] J.-F. Wyart and P. Camus, Extended Analysis of the Emission Spectrum of Neutral Ytterbium (Yb I), *Phys. Scr.* **20**, 43 (1979).

## Supplemental Material

### SI: MQDT model parameters

#### A. $^{174}\text{Yb}$

Table S1. Six-channel MQDT model parameters for the  $6sns^1S_0$  series of  $^{174}\text{Yb}$  obtained from fit to spectroscopic data presented in Tabs. S11 to S13 and S16 to S20. The electronic configuration of the perturbing Rydberg channels  $4f^{13}5d6snp$  is abbreviated as  $5d$ . The rotations  $\mathcal{R}(\theta_{ij})$  are applied in the order  $\mathcal{R}(\theta_{12})\mathcal{R}(\theta_{13})\mathcal{R}(\theta_{14})\mathcal{R}(\theta_{34})\mathcal{R}(\theta_{35})\mathcal{R}(\theta_{16})$ .

$i, \bar{\alpha}, \alpha$	1	2	3	4	5	6
$ i\rangle$	$(6s_{1/2})(ns_{1/2})$	$5d \mathbf{a}$	$(6p_{3/2})(np_{3/2})$	$5d \mathbf{b}$	$(6p_{1/2})(np_{1/2})$	$5d \mathbf{c}$
$I_i$ ( $\text{cm}^{-1}$ )	50 443.070393	83 967.7	80 835.39	83 967.7	77 504.98	83 967.7
$ \bar{\alpha}\rangle$	$6sns^1S_0$	$5d \mathbf{a}$	$6pnp^1S_0$	$5d \mathbf{b}$	$6pnp^3P_0$	$5d \mathbf{c}$
$\mu_\alpha^{(0)}$	0.355097325	0.204537279	0.116394359	0.295432196	0.25765161	0.155807042
$\mu_\alpha^{(2)}$	0.278368431	0.0	0.0	0.0	0.0	0.0
$V_{\bar{\alpha}\alpha}$	$\theta_{12} = 0.12654859$	$\theta_{13} = 0.30010744$	$\theta_{14} = 0.05703381$	$\theta_{34} = 0.11439805$	$\theta_{35} = 0.09864375$	$\theta_{16} = 0.14248210$
$U_{i\bar{\alpha}}$	1	0	0	0	0	0
	0	1	0	0	0	0
	0	0	$-\sqrt{2/3}$	0	$\sqrt{1/3}$	0
	0	0	0	1	0	0
	0	0	$\sqrt{1/3}$	0	$\sqrt{2/3}$	0
	0	0	0	0	0	1

Table S2. Five-channel MQDT model parameters for the  $6snd^{1,3}D_2$  series of  $^{174}\text{Yb}$  obtained from a global fit to spectroscopic data presented in Tabs. S11 to S13 and S16 to S20. The electronic configuration of the perturbing Rydberg channels  $4f^{13}5d6snp$  is abbreviated as  $5d$ . The rotations  $\mathcal{R}(\theta_{ij})$  are applied in the order  $\mathcal{R}(\theta_{12}(\epsilon))\mathcal{R}(\theta_{13})\mathcal{R}(\theta_{14})\mathcal{R}(\theta_{24})\mathcal{R}(\theta_{15})\mathcal{R}(\theta_{25})$ . The channel- $g$ -factors  $g^*$  are obtained in  $LS$  coupling for channels 1 and 2, and by a fit to experimentally observed  $g$  factors [S1] for the remaining channels.

$i, \bar{\alpha}, \alpha$	1	2	3	4	5
$ i\rangle$	$(6s_{1/2})(nd_{5/2})$	$(6s_{1/2})(nd_{3/2})$	$5d \mathbf{a}$	$5d \mathbf{b}$	$(6p)(np)$
$I_i$ ( $\text{cm}^{-1}$ )	50 443.070393	50 443.070393	83 967.7	83 967.7	79 725.35
$ \bar{\alpha}\rangle$	$6snd^1D_2$	$6snd^3D_2$	$5d \mathbf{a}$	$5d \mathbf{b}$	$6pnp^1D_2$
$\mu_\alpha^{(0)}$	0.729500971	0.75229161	0.196120406	0.233821165	0.152890218
$\mu_\alpha^{(2)}$	-0.0284447537	0.0967044398	0.0	0.0	0.0
$V_{\bar{\alpha}\alpha}$	$\theta_{12}^{(0)} = 0.21157531$ $\theta_{12}^{(2)} = -15.3844$	$\theta_{13} = 0.00522534111$ $\theta_{25} = 0.0721775002$	$\theta_{14} = 0.0398754262$	$\theta_{24} = -0.00720265975$	$\theta_{15} = 0.104784389$
$g^*$	1	1.1670	1.1846	0.9390	1.2376
$U_{i\bar{\alpha}}$	$\sqrt{3/5}$	$\sqrt{2/5}$	0	0	0
	$-\sqrt{2/5}$	$\sqrt{3/5}$	0	0	0
	0	0	1	0	0
	0	0	0	1	0
	0	0	0	0	1

Table S3. Six-channel MQDT model parameters for the  $6snp^{1,3}P_1$  series of  $^{174}\text{Yb}$  obtained from fit to spectroscopic data presented in Tabs. S11 to S13 and S16 to S20. The electronic configuration of the perturbing Rydberg channels  $4f^{13}5d6snd$  is abbreviated as  $5d$ . The rotations  $\mathcal{R}(\theta_{ij})$  are applied in the order  $\mathcal{R}(\theta_{12}(\epsilon))\mathcal{R}(\theta_{13})\mathcal{R}(\theta_{14})\mathcal{R}(\theta_{15})\mathcal{R}(\theta_{16})\mathcal{R}(\theta_{23})\mathcal{R}(\theta_{24})\mathcal{R}(\theta_{25})\mathcal{R}(\theta_{26})$ .

$i, \bar{\alpha}, \alpha$	1	2	3	4	5	6
$ i\rangle$	$(6s_{1/2})(np_{3/2})$	$(6s_{1/2})(np_{1/2})$	$5d \mathbf{a}$	$5d \mathbf{b}$	$5d \mathbf{c}$	$5d \mathbf{d}$
$I_i$ ( $\text{cm}^{-1}$ )	50 443.070393	50 443.070393	83 967.7	83 967.7	83 967.7	83 967.7
$ \bar{\alpha}\rangle$	$6snp^1P_1$	$6snp^3P_1$	$5d \mathbf{a}$	$5d \mathbf{b}$	$5d \mathbf{c}$	$5d \mathbf{d}$
$\mu_\alpha^{(0)}$	0.92271098	0.98208719	0.22851720	0.20607759	0.19352751	0.18153094
$\mu_\alpha^{(2)}$	2.6036257	-5.4562725	0.0	0.0	0.0	0.0
$V_{\bar{\alpha}\alpha}$	$\theta_{12}^{(0)} = -0.08410871$ $\theta_{16} = -0.10451698$	$\theta_{12}^{(2)} = 120.37555$ $\theta_{23} = 0.02477048$	$\theta_{12}^{(4)} = -9314.23$ $\theta_{24} = 0.05765807$	$\theta_{13} = -0.07318156$ $\theta_{25} = 0.08606276$	$\theta_{14} = -0.06651977$ $\theta_{26} = 0.04994363$	$\theta_{15} = -0.02210989$
$U_{i\bar{\alpha}}$	$\sqrt{2/3}$ $-\sqrt{1/3}$ 0 0 0 0	$\sqrt{1/3}$ $\sqrt{2/3}$ 0 0 0 0	0 0 1 0 0 0	0 0 0 1 0 0	0 0 0 0 1 0	0 0 0 0 0 1

Table S4. Four-channel MQDT model parameters for the  $6snp^3P_2$  series of  $^{174}\text{Yb}$  obtained from fit to spectroscopic data presented in Tabs. S21 and S22. The electronic configuration of the perturbing Rydberg channels  $4f^{13}5d6snd$  is abbreviated as  $5d$ . The rotations  $\mathcal{R}(\theta_{ij})$  are applied in the order  $\mathcal{R}(\theta_{12})\mathcal{R}(\theta_{13})\mathcal{R}(\theta_{14})$

$i, \bar{\alpha}, \alpha$	1	2	3	4
$ i\rangle$	$(6s_{1/2})(np_{3/2})$	$5d \mathbf{a}$	$5d \mathbf{b}$	$5d \mathbf{c}$
$I_i$ ( $\text{cm}^{-1}$ )	50 443.070393	83 967.7	83 967.7	83 967.7
$ \bar{\alpha}\rangle$	$6snp^3P_2$	$5d \mathbf{a}$	$5d \mathbf{b}$	$5d \mathbf{c}$
$\mu_\alpha^{(0)}$	0.925121305	0.230133261	0.209638118	0.186228192
$\mu_\alpha^{(2)}$	-2.73247165	0.0	0.0	0.0
$\mu_\alpha^{(4)}$	74.664989	0.0	0.0	0.0
$V_{\bar{\alpha}\alpha}$	$\theta_{12} = 0.0706666127$	$\theta_{13} = 0.0232711158$	$\theta_{14} = -0.0292153659$	
$U_{i\bar{\alpha}}$	1 0 0 0	0 1 0 0	0 0 1 0	0 0 0 1

Table S5. Two-channel MQDT model parameters for the  $6snp^3P_0$  series of  $^{174}\text{Yb}$  obtained from fit to spectroscopic data presented in Tabs. S23 and S24. We follow Ref. [S2] and presume a perturbing channel of character  $4f^{13}5d6snd^3P_0$  (labelled  $Q$ ) with an ionization limit of as  $83\,967.7\text{cm}^{-1}$ .

$i, \bar{\alpha}, \alpha$	1	2
$ i\rangle$	$(6s_{1/2})(np_{1/2})$	$4f^{13}5d6snd$
$I_i$ ( $\text{cm}^{-1}$ )	50 443.070393	83 967.7
$ \bar{\alpha}\rangle$	$6snp^3P_0$	$Q$
$\mu_\alpha^{(0)}$	0.95356884	0.19845903
$\mu_\alpha^{(2)}$	-0.28602498	0.0
$V_{\bar{\alpha}\alpha}$	$\theta_{12} = 0.16328854$	
$U_{i\bar{\alpha}}$	1 0	0 1

**B.  $^{171}\text{Yb}$**

Table S6. Seven-channel MQDT model parameters for the  $|\nu, L = 0, F = 1/2\rangle$  series of  $^{171}\text{Yb}$  obtained from fit to spectroscopic data presented in Tab. S25. The electronic configuration of the perturbing Rydberg channels  $4f^{13}5d6snp$  is abbreviated as  $5d$ . The rotations  $\mathcal{R}(\theta_{ij})$  are applied in the order  $\mathcal{R}(\theta_{12})\mathcal{R}(\theta_{13})\mathcal{R}(\theta_{14})\mathcal{R}(\theta_{34})\mathcal{R}(\theta_{35})\mathcal{R}(\theta_{16})$ .

$i, \bar{\alpha}, \alpha$	1 ( $F_c = 0$ )	2	3	4	5	6	7 ( $F_c = 1$ )
$ i_F\rangle$	$(6s_{1/2})(ns_{1/2})$	$5d \mathbf{a}$	$(6p_{3/2})(np_{3/2})$	$5d \mathbf{b}$	$(6p_{1/2})(np_{1/2})$	$5d \mathbf{c}$	$(6s_{1/2})(ns_{1/2})$
$I_i$ ( $\text{cm}^{-1}$ )	50442.795744	83967.7	80835.39	83967.7	77504.98	83967.7	50443.217463
$ \bar{\alpha}\rangle$	$6sns \ ^1S_0$	$5d \mathbf{a}$	$6pnp \ ^1S_0$	$5d \mathbf{b}$	$6pnp \ ^3P_0$	$5d \mathbf{c}$	$6sns \ ^3S_1$
$\mu_{\alpha}^{(0)}$	0.357519763	0.203907536	0.116803536	0.286731074	0.248113946	0.148678953	$\mu_{3S_1}^{3S_1}$
$\mu_{\alpha}^{(2)}$	0.298712849	0.0	0.0	0.0	0.0	0.0	
$\mu_{3S_1}^{3S_1}$	$\mu_{3S_1}^{(0)} = 0.438426851$	$\mu_{3S_1}^{(2)} = 3.91762642$	$\mu_{3S_1}^{(4)} = -10612.6828$	$\mu_{3S_1}^{(6)} = 8017432.38$	$\mu_{3S_1}^{(8)} = -2582622910.0$		
$V_{\bar{\alpha}\alpha}$	$\theta_{12} = 0.131810463$	$\theta_{13} = 0.297612147$	$\theta_{14} = 0.055508821$	$\theta_{34} = 0.101030515$	$\theta_{35} = 0.102911159$	$\theta_{16} = 0.137723736$	
$U_{i\bar{\alpha}}$	$1/2$	0	0	0	0	0	$\sqrt{3}/2$
	0	1	0	0	0	0	0
	0	0	$-\sqrt{2}/3$	0	$\sqrt{1}/3$	0	0
	0	0	0	1	0	0	0
	0	0	$\sqrt{1}/3$	0	$\sqrt{2}/3$	0	0
	0	0	0	0	0	1	0
	$\sqrt{3}/2$	0	0	0	0	0	$-1/2$





Table S9. Six-channel MQDT model parameters for the  $|\nu, L = 2, F = 3/2\rangle$  series of  $^{171}\text{Yb}$  obtained from fit to spectroscopic data presented in Tab. S39 and S41. The electronic configuration of the perturbing Rydberg channels  $4f^{13}5d6snp$  is abbreviated as  $5d$ . The rotations  $\mathcal{R}(\theta_{ij})$  are applied in the order  $\mathcal{R}(\theta_{12})\mathcal{R}(\theta_{13})\mathcal{R}(\theta_{14})\mathcal{R}(\theta_{24})\mathcal{R}(\theta_{15})\mathcal{R}(\theta_{25})$ .

$i, \bar{\alpha}, \alpha$	1 ( $F_c = 1$ )	2 ( $F_c = 1$ )	3	4	5	6 ( $F_c = 0$ )
$ i\rangle$	$(6s_{1/2})(nd_{5/2})$	$(6s_{1/2})(nd_{3/2})$	$5d \mathbf{a}$	$5d \mathbf{b}$	$(6p)(np)$	$(6s_{1/2})(nd_{3/2})$
$I_i$ ( $\text{cm}^{-1}$ )	50 443.217463	50 443.217463	83 967.7	83 967.7	79 725.35	50 442.795744
$ \bar{\alpha}\rangle$	$6snd^1 D_2$	$6snd^3 D_2$	$5d \mathbf{a}$	$5d \mathbf{b}$	$6pnp^1 D_2$	$6snd^3 D_1$
$\mu_{\alpha}^{(0)}$	0.730537124	0.751591782	0.196120394	0.233742396	0.152905343	$\mu_{3D_1}^{3T}$
$\mu_{\alpha}^{(2)}$	-0.000186828866	-0.00114049637	0.0	0.0	0.0	
$\mu_{3D_1}^{3T}$	$\mu_{3D_1}^{(0)} = 0.75258093$	$\mu_{3D_1}^{(2)} = 0.382628525$	$\mu_{3D_1}^{(4)} = -483.120633$			
$V_{\bar{\alpha}\alpha}$	$\theta_{12} = 0.205496654$	$\theta_{13} = 0.00522401624$	$\theta_{14} = 0.0409502343$	$\theta_{24} = -0.00378075773$	$\theta_{15} = 0.108563952$	$\theta_{25} = 0.0665700438$
$U_{i\bar{\alpha}}$	$-\sqrt{3/5}$	$-\sqrt{2/5}$	0	0	0	0
	$\sqrt{3/5}/2$	$-3/(2\sqrt{10})$	0	0	0	$\sqrt{5/2}/2$
	0	0	1	0	0	0
	0	0	0	1	0	0
	0	0	0	0	1	0
	-1/2	$\sqrt{3/2}/2$	0	0	0	$\sqrt{3/2}/2$

Table S10. Six-channel MQDT model parameters for the  $|\nu, L = 2, F = 5/2\rangle$  series of  $^{171}\text{Yb}$  obtained from fit to spectroscopic data presented in Tab. S39 and S41. The electronic configuration of the perturbing Rydberg channels  $4f^{13}5d6snp$  is abbreviated as  $5d$ . The rotations  $\mathcal{R}(\theta_{ij})$  are applied in the order  $\mathcal{R}(\theta_{12})\mathcal{R}(\theta_{13})\mathcal{R}(\theta_{14})\mathcal{R}(\theta_{24})\mathcal{R}(\theta_{15})\mathcal{R}(\theta_{25})$ .

$i, \bar{\alpha}, \alpha$	1 ( $F_c = 1$ )	2 ( $F_c = 1$ )	3	4	5	6 ( $F_c = 0$ )
$ i\rangle$	$(6s_{1/2})(nd_{5/2})$	$(6s_{1/2})(nd_{3/2})$	5d <b>a</b>	5d <b>b</b>	$(6p)(np)$	$(6s_{1/2})(nd_{5/2})$
$I_i$ ( $\text{cm}^{-1}$ )	50 443.217463	50 443.217463	83 967.7	83 967.7	79 725.35	50 442.795744
$ \bar{\alpha}\rangle$	$6snd^1D_2$	$6snd^3D_2$	5d <b>a</b>	5d <b>b</b>	$6pnp^1D_2$	$6snd^3D_3$
$\mu_{\alpha}^{(0)}$	0.730537124	0.751591782	0.196120394	0.233742396	0.152905343	$\mu_{3D_3}^{nr}$
$\mu_{\alpha}^{(2)}$	-0.000186828866	-0.00114049637	0.0	0.0	0.0	
$\mu_{3D_3}^{nr}$	$\mu_{3D_3}^{(0)} = 0.72895315$	$\mu_{3D_3}^{(2)} = -0.20653489$	$\mu_{3D_3}^{(4)} = 220.484722$			
$V_{\alpha\alpha}$	$\theta_{12} = 0.205496654$	$\theta_{13} = 0.00522401624$	$\theta_{14} = 0.0409502343$	$\theta_{24} = -0.00378075773$	$\theta_{15} = 0.108563952$	$\theta_{25} = 0.0665700438$
$U_{i\bar{\alpha}}$	$\sqrt{7/5/2}$	$\sqrt{7/30}$	0	0	0	$-\sqrt{5/3/2}$
	$-\sqrt{2/5}$	$\sqrt{3/5}$	0	0	0	0
	0	0	1	0	0	0
	0	0	0	1	0	0
	0	0	0	0	1	0
	1/2	$\sqrt{1/6}$	0	0	0	$\sqrt{7/3/2}$

## SII: Table of spectroscopic results

This is a compilation of the previous [S2–S14] and new spectroscopic data used for the development of the MQDT models presented in this article. The dataset is available for download at the Harvard Dataverse [S15].

### A. $^{174}\text{Yb } ^1S_0$

Table S11: Laser spectroscopic data of the  $6sns \ ^1S_0$  Rydberg series included in the determination of the MQDT models. The state energies and the respective uncertainties are taken from Refs. [S3, S4] as compiled in [S5], and from Ref. [S6]. As in Ref. [S6], the observed wavenumbers from Ref. [S5] are reduced by  $0.1 \text{ cm}^{-1}$ .

State label	$\tilde{\nu}_{\text{exp.}} \text{ (cm}^{-1}\text{)}$	$\tilde{\nu}_{\text{th.}} \text{ (cm}^{-1}\text{)}$	$E_{\text{exp.}} - E_{\text{th.}}$ ( $h \cdot \text{MHz}$ )	Ref.
$6s7s \ ^1S_0$	34 350.55(10)	34 349.227 809	39 638	[S5]
$6s8s \ ^1S_0$	41 939.78(10)	41 939.687 015	2788	[S5]
$6p^2 \ ^3P_0$	42 436.84(10)	42 436.901 198	-1835	[S5]
$4f^{13}5d6s6p \ B$	46 081.44(10)	46 081.618 520	-5352	[S5]
$6s10s \ ^1S_0$	46 893.14(10)	46 893.135 082	147	[S5]
$6s11s \ ^1S_0$	47 808.39(10)	47 808.418 289	-848	[S5]
$6p^2 \ ^1S_0$	48 344.28(10)	48 344.184 498	2863	[S5]
$6s12s \ ^1S_0$	48 723.39(10)	48 723.404 543	-436	[S5]
$6s13s \ ^1S_0$	49 046.33(10)	49 046.326 912	93	[S5]
$6s14s \ ^1S_0$	49 302.44(10)	49 302.594 518	-4632	[S5]
$6s15s \ ^1S_0$	49 499.14(10)	49 498.896 317	7305	[S5]
$6s16s \ ^1S_0$	49 649.95(10)	49 649.937 316	380	[S5]
$6s17s \ ^1S_0$	49 767.75(10)	49 767.683 212	2002	[S5]
$6s18s \ ^1S_0$	49 859.41(10)	49 859.328 215	2452	[S5]
$4f^{13}5d6s6p \ A$	49 897.22(10)	49 897.247 483	-824	[S5]
$6s19s \ ^1S_0$	49 940.64(10)	49 940.693 054	-1591	[S5]
$6s20s \ ^1S_0$	50 001.25(10)	50 001.050 710	5975	[S5]
$6s21s \ ^1S_0$	50 051.82(10)	50 051.872 944	-1587	[S5]
$6s22s \ ^1S_0$	50 094.61(10)	50 094.534 502	2263	[S5]
$6s23s \ ^1S_0$	50 130.625 48(10)	50 130.625 177	9.20	[S6]
$6s24s \ ^1S_0$	50 161.409 31(10)	50 161.409 005	9.27	[S6]
$6s25s \ ^1S_0$	50 187.870 22(10)	50 187.869 988	6.96	[S6]
$6s26s \ ^1S_0$	50 210.777 67(10)	50 210.777 495	5.15	[S6]
$6s27s \ ^1S_0$	50 230.738 54(10)	50 230.738 437	3.19	[S6]
$6s28s \ ^1S_0$	50 248.236 25(10)	50 248.236 135	3.38	[S6]
$6s29s \ ^1S_0$	50 263.659 05(10)	50 263.659 083	-0.96	[S6]
$6s30s \ ^1S_0$	50 277.322 24(10)	50 277.322 301	-1.91	[S6]
$6s31s \ ^1S_0$	50 289.483 45(10)	50 289.483 338	3.36	[S6]
$6s32s \ ^1S_0$	50 300.354 17(10)	50 300.354 369	-5.96	[S6]
$6s33s \ ^1S_0$	50 310.111 32(10)	50 310.111 439	-3.58	[S6]
$6s34s \ ^1S_0$	50 318.901 54(10)	50 318.901 593	-1.72	[S6]
$6s35s \ ^1S_0$	50 326.848 50(10)	50 326.848 409	2.69	[S6]
$6s36s \ ^1S_0$	50 334.056 42(10)	50 334.056 356	1.90	[S6]
$6s37s \ ^1S_0$	50 340.614 22(10)	50 340.614 223	0.00	[S6]
$6s38s \ ^1S_0$	50 346.597 83(10)	50 346.597 860	-0.94	[S6]
$6s39s \ ^1S_0$	50 352.072 42(10)	50 352.072 378	1.15	[S6]
$6s40s \ ^1S_0$	50 357.093 89(10)	50 357.093 914	-0.73	[S6]
$6s41s \ ^1S_0$	50 361.711 02(10)	50 361.711 085	-2.03	[S6]
$6s42s \ ^1S_0$	50 365.966 16(10)	50 365.966 154	0.21	[S6]
$6s43s \ ^1S_0$	50 369.896 15(10)	50 369.896 009	4.15	[S6]
$6s44s \ ^1S_0$	50 373.533 00(10)	50 373.532 957	1.17	[S6]
$6s45s \ ^1S_0$	50 376.905 46(10)	50 376.905 393	2.06	[S6]
$6s46s \ ^1S_0$	50 380.038 43(10)	50 380.038 354	2.28	[S6]
$6s47s \ ^1S_0$	50 382.953 98(10)	50 382.953 983	-0.08	[S6]
$6s48s \ ^1S_0$	50 385.671 79(10)	50 385.671 922	-3.84	[S6]
$6s49s \ ^1S_0$	50 388.209 68(10)	50 388.209 646	1.12	[S6]

Table S11 (*continued*)

State label	$\tilde{\nu}_{\text{exp.}}$ ( $\text{cm}^{-1}$ )	$\tilde{\nu}_{\text{th.}}$ ( $\text{cm}^{-1}$ )	$E_{\text{exp.}} - E_{\text{th.}}$ ( $h \cdot \text{MHz}$ )	Ref.
$6s50s^1S_0$	50 390.582 79(10)	50 390.582 738	1.59	[S6]
$6s51s^1S_0$	50 392.805 06(10)	50 392.805 135	-2.20	[S6]
$6s52s^1S_0$	50 394.889 10(10)	50 394.889 330	-6.78	[S6]
$6s53s^1S_0$	50 396.846 52(10)	50 396.846 547	-0.68	[S6]
$6s54s^1S_0$	50 398.686 86(10)	50 398.686 893	-0.88	[S6]
$6s55s^1S_0$	50 400.419 33(10)	50 400.419 491	-4.87	[S6]
$6s56s^1S_0$	50 402.052 46(10)	50 402.052 590	-3.93	[S6]
$6s57s^1S_0$	50 403.593 72(10)	50 403.593 664	1.82	[S6]
$6s58s^1S_0$	50 405.049 40(10)	50 405.049 499	-3.01	[S6]
$6s59s^1S_0$	50 406.426 28(10)	50 406.426 267	0.53	[S6]
$6s60s^1S_0$	50 407.729 59(10)	50 407.729 591	-0.12	[S6]
$6s61s^1S_0$	50 408.964 44(10)	50 408.964 603	-4.85	[S6]
$6s62s^1S_0$	50 410.135 85(10)	50 410.135 994	-4.29	[S6]
$6s63s^1S_0$	50 411.248 02(10)	50 411.248 060	-1.18	[S6]
$6s64s^1S_0$	50 412.304 82(10)	50 412.304 741	2.34	[S6]
$6s65s^1S_0$	50 413.309 65(10)	50 413.309 653	-0.19	[S6]
$6s66s^1S_0$	50 414.266 24(10)	50 414.266 124	3.52	[S6]
$6s67s^1S_0$	50 415.177 21(10)	50 415.177 218	-0.37	[S6]
$6s68s^1S_0$	50 416.045 81(10)	50 416.045 760	1.40	[S6]
$6s69s^1S_0$	50 416.874 38(10)	50 416.874 360	0.61	[S6]
$6s70s^1S_0$	50 417.665 46(10)	50 417.665 428	0.96	[S6]
$6s71s^1S_0$	50 418.421 25(10)	50 418.421 198	1.55	[S6]
$6s72s^1S_0$	50 419.143 75(10)	50 419.143 740	0.30	[S6]
$6s73s^1S_0$	50 419.835 03(10)	50 419.834 972	1.67	[S6]
$6s74s^1S_0$	50 420.496 62(10)	50 420.496 678	-1.78	[S6]
$6s75s^1S_0$	50 421.130 46(10)	50 421.130 516	-1.75	[S6]
$6s76s^1S_0$	50 421.737 94(10)	50 421.738 029	-2.55	[S6]
$6s77s^1S_0$	50 422.320 81(10)	50 422.320 655	4.78	[S6]
$6s78s^1S_0$	50 422.879 73(10)	50 422.879 734	0.00	[S6]
$6s79s^1S_0$	50 423.416 44(10)	50 423.416 519	-2.40	[S6]
$6s80s^1S_0$	50 423.932 20(10)	50 423.932 179	0.50	[S6]

Table S12: Spectroscopic data of  $n^1S_0 \leftrightarrow n'^1S_0$  Rydberg-Rydberg transitions obtained by microwave spectroscopy, as presented in Ref. [S7] and Ref. [S6].

$f$	$i$	$\Delta E_{f \leftarrow i}^{\text{exp.}}$ ( $h \cdot \text{MHz}$ )	$\Delta E_{f \leftarrow i}^{\text{theo.}}$ ( $h \cdot \text{MHz}$ )	$E_{\text{exp.}} - E_{\text{th.}}$ ( $h \cdot \text{MHz}$ )	Ref.
$6s35s^1S_0$	$6s34s^1S_0$	238 239.32(12)	238 239.57	-0.25	[S6]
$6s36s^1S_0$	$6s35s^1S_0$	216 088.70(14)	216 088.80	-0.10	[S6]
$6s37s^1S_0$	$6s36s^1S_0$	196 599.98(12)	196 599.91	0.07	[S6]
$6s38s^1S_0$	$6s37s^1S_0$	179 384.72(12)	179 384.94	-0.22	[S6]
$6s39s^1S_0$	$6s38s^1S_0$	164 121.48(12)	164 121.90	-0.42	[S6]
$6s40s^1S_0$	$6s39s^1S_0$	150 540.64(10)	150 541.89	-1.25	[S6]
$6s41s^1S_0$	$6s40s^1S_0$	138 420.36(80)	138 419.28	1.08	[S7]
$6s42s^1S_0$	$6s41s^1S_0$	127 563.40(80)	127 563.77	-0.37	[S7]
$6s43s^1S_0$	$6s42s^1S_0$	117 814.16(12)	117 814.08	0.08	[S6]
$6s44s^1S_0$	$6s43s^1S_0$	109 032.84(80)	109 032.97	-0.13	[S7]
$6s45s^1S_0$	$6s44s^1S_0$	101 103.00(80)	101 103.09	-0.09	[S7]
$6s46s^1S_0$	$6s45s^1S_0$	93 924.12(80)	93 923.80	0.32	[S7]
$6s47s^1S_0$	$6s46s^1S_0$	87 408.62(80)	87 408.35	0.27	[S7]
$6s48s^1S_0$	$6s47s^1S_0$	81 481.92(80)	81 481.78	0.14	[S7]
$6s49s^1S_0$	$6s48s^1S_0$	76 079.14(80)	76 079.04	0.10	[S7]
$6s50s^1S_0$	$6s49s^1S_0$	71 143.62(80)	71 143.52	0.10	[S7]
$6s51s^1S_0$	$6s50s^1S_0$	66 625.94(80)	66 625.79	0.15	[S7]
$6s52s^1S_0$	$6s51s^1S_0$	62 482.74(80)	62 482.59	0.15	[S7]

Table S12 (*continued*)

$f$	$i$	$\Delta E_{f \leftarrow i}^{\text{exp.}} (h \cdot \text{MHz})$	$\Delta E_{f \leftarrow i}^{\text{theo.}} (h \cdot \text{MHz})$	$E_{\text{exp.}} - E_{\text{th.}} (h \cdot \text{MHz})$	Ref.
$6s53s^1S_0$	$6s52s^1S_0$	58 675.66(80)	58 675.88	-0.22	[S7]

Table S13: Spectroscopic data of  $n^1S_0 \leftrightarrow n'^1S_0$  Rydberg-Rydberg transitions obtained by microwave spectroscopy, as presented in Ref. [S7] and Ref. [S6].

$f$	$i$	$\Delta E_{f \leftarrow i}^{\text{exp.}} (h \cdot \text{MHz})$	$\Delta E_{f \leftarrow i}^{\text{theo.}} (h \cdot \text{MHz})$	$E_{\text{exp.}} - E_{\text{th.}} (h \cdot \text{MHz})$	Ref.
$6s29s^1S_0$	$6s28d^1D_2$	-235 548.18(22)	-235 549.07	0.89	[S6]
$6s30s^1S_0$	$6s29d^1D_2$	-209 275.16(22)	-209 275.15	-0.01	[S6]
$6s31s^1S_0$	$6s30d^1D_2$	-186 918.48(12)	-186 918.43	-0.05	[S6]
$6s32s^1S_0$	$6s31d^1D_2$	-167 680.52(16)	-167 679.89	-0.63	[S6]
$6s33s^1S_0$	$6s32d^1D_2$	-151 009.20(14)	-151 008.75	-0.45	[S6]
$6s34s^1S_0$	$6s33d^1D_2$	-136 482.22(10)	-136 481.90	-0.32	[S6]
$6s35s^1S_0$	$6s34d^1D_2$	-123 762.40(16)	-123 761.92	-0.48	[S6]
$6s36s^1S_0$	$6s35d^1D_2$	-112 576.06(18)	-112 574.97	-1.09	[S6]
$6s37s^1S_0$	$6s36d^1D_2$	-102 697.06(14)	-102 696.27	-0.79	[S6]
$6s38s^1S_0$	$6s37d^1D_2$	-93 940.32(10)	-93 939.81	-0.51	[S6]
$6s39s^1S_0$	$6s38d^1D_2$	-86 151.10(16)	-86 150.54	-0.56	[S6]
$6s40s^1S_0$	$6s39d^1D_2$	-79 199.54(18)	-79 198.53	-1.01	[S6]
$6s41s^1S_0$	$6s40d^1D_2$	-72 974.18(80)	-72 974.26	0.08	[S7]
$6s42s^1S_0$	$6s41d^1D_2$	-67 385.66(80)	-67 385.00	-0.66	[S7]
$6s43s^1S_0$	$6s42d^1D_2$	-62 351.88(12)	-62 351.81	-0.07	[S6]
$6s44s^1S_0$	$6s43d^1D_2$	-57 807.28(10)	-57 807.27	-0.01	[S6]
$6s45s^1S_0$	$6s44d^1D_2$	-53 693.84(80)	-53 693.53	-0.31	[S7]
$6s46s^1S_0$	$6s45d^1D_2$	-49 961.68(80)	-49 960.75	-0.93	[S7]
$6s47s^1S_0$	$6s46d^1D_2$	-46 566.70(80)	-46 565.88	-0.82	[S7]
$6s48s^1S_0$	$6s47d^1D_2$	-43 472.26(80)	-43 471.53	-0.73	[S7]
$6s49s^1S_0$	$6s48d^1D_2$	-40 645.06(80)	-40 645.20	0.14	[S7]

Table S14: Experimental ( $\alpha_{0,\text{exp.}}$ ) and predicted ( $\alpha_{0,\text{theo.}}$ ) static dipole polarizabilities of  $6sns^1S_0$  Rydberg states of  $^{174}\text{Yb}$ . The experimental values for  $\alpha_{0,\text{exp.}}$  are obtained by measurement of quadratic Stark shifts as described in App. B of the main text. Prediction for the static dipole polarizability  $\alpha_{0,\text{theo.}}$  are obtained from a non-perturbative diagonalization of the atomic Hamiltonian including electric fields [S16].

State label	$\alpha_{0,\text{exp.}} (h \cdot \text{MHz}/(\text{V}/\text{cm})^2)$	$\alpha_{0,\text{theo.}} (h \cdot \text{MHz}/(\text{V}/\text{cm})^2)$
$6s35s^1S_0$	22.6(7)	24.2
$6s36s^1S_0$	32.3(7)	31.5
$6s37s^1S_0$	42.7(11)	41.6
$6s38s^1S_0$	57.1(6)	57.0
$6s39s^1S_0$	87.1(9)	87.2
$6s40s^1S_0$	231.4(11)	241.1
$6s41s^1S_0$	-62.5(5)	-62.8
$6s42s^1S_0$	21.2(9)	21.3
$6s43s^1S_0$	54.3(7)	53.4
$6s44s^1S_0$	78.1(8)	78.8
$6s45s^1S_0$	103.4(5)	103.8
$6s46s^1S_0$	130.3(9)	130.6
$6s47s^1S_0$	160.1(10)	160.4
$6s48s^1S_0$	192.7(5)	194.0
$6s49s^1S_0$	231.3(11)	232.0
$6s50s^1S_0$	276.7(8)	275.3

**B.  $^{174}\text{Yb } ^3S_1$**

Table S15: Experimental ( $\alpha_{0,\text{exp.}}$ ) and predicted ( $\alpha_{0,\text{theo.}}$ ) static dipole polarizabilities of  $6sns^3S_1(m_J = 0, \pm 1)$  Rydberg states of  $^{174}\text{Yb}$ . The experimental values for  $\alpha_{0,\text{exp.}}$  are obtained by measurement of quadratic Stark shifts as described in App. B of the main text. Prediction for the static dipole polarizability  $\alpha_{0,\text{theo.}}$  are obtained from a non-perturbative diagonalization of the atomic Hamiltonian including electric fields [S16].

State label	$\alpha_{0,\text{exp.}}^{(m_J=0)}$ ( $h \cdot \text{MHz}/(\text{V}/\text{cm})^2$ )	$\alpha_{0,\text{theo.}}^{(m_J=0)}$ ( $h \cdot \text{MHz}/(\text{V}/\text{cm})^2$ )	$\alpha_{0,\text{exp.}}^{(m_J=\pm 1)}$ ( $h \cdot \text{MHz}/(\text{V}/\text{cm})^2$ )	$\alpha_{0,\text{theo.}}^{(m_J=\pm 1)}$ ( $h \cdot \text{MHz}/(\text{V}/\text{cm})^2$ )
$6s31s^3S_1$	29.9(8)	30.0	4.7(1)	3.1
$6s32s^3S_1$	83.4(2)	87.6	3.8(1)	4.3
$6s33s^3S_1$	-751(3)	-697.5	6.9(1)	6.0
$6s34s^3S_1$	-113.4(3)	-116.0	9.2(3)	8.4
$6s35s^3S_1$	-79.2(2)	-81.4	11.3(2)	11.7
$6s36s^3S_1$	-69.3(10)	-72.4	15.5(2)	16.3
$6s39s^3S_1$	-78.5(14)	-78.7	38.9(3)	45.5
$6s40s^3S_1$	-85.8(13)	-85.8	62.8(3)	65.2

C.  $^{174}\text{Yb } 1,3D_2$ 

Table S16: Laser spectroscopic data of the  $6snd^{1,3}D_2$  Rydberg series included in the determination of the MQDT models. The state energies and the respective uncertainties are taken from Refs. [S3, S4] as compiled in [S5], and from Ref. [S6].

State label	$\tilde{\nu}_{\text{exp.}}$ ( $\text{cm}^{-1}$ )	$\tilde{\nu}_{\text{th.}}$ ( $\text{cm}^{-1}$ )	$E_{\text{exp.}} - E_{\text{th.}}$ ( $h \cdot \text{MHz}$ )	Ref.
$6s8d^1D_2$	46 405.62(10)	46 403.272 104	70 388	[S5]
$6s8d^3D_2$	46 467.69(10)	46 468.043 298	-10 592	[S5]
$6p^2^1D_2$	47 420.97(10)	47 421.132 756	-4879	[S5]
$6s9d^3D_2$	47 634.40(10)	47 634.131 975	8035	[S5]
$6s9d^1D_2$	47 821.74(10)	47 822.162 808	-12 675	[S5]
$6s10d^3D_2$	48 357.63(10)	48 353.002 109	138 741	[S5]
$6s10d^1D_2$	48 403.49(10)	48 394.683 988	263 998	[S5]
$4f^{13}5d6s6p B$	48 762.52(10)	48 760.869 520	49 480	[S5]
$6s11d^3D_2$	48 838.14(10)	48 835.934 045	66 133	[S5]
$6s11d^1D_2$	48 883.12(10)	48 875.940 853	215 225	[S5]
$6s12d^3D_2$	49 161.12(10)	49 161.781 360	-19 827	[S5]
$6s12d^1D_2$	49 176.00(10)	49 177.241 316	-37 214	[S5]
$6s13d^3D_2$	49 399.10(10)	49 399.198 912	-2965	[S5]
$6s13d^1D_2$	49 408.58(10)	49 409.028 480	-13 445	[S5]
$6s14d^3D_2$	49 576.36(10)	49 576.392 356	-970	[S5]
$6s14d^1D_2$	49 583.28(10)	49 583.267 177	384	[S5]
$6s15d^3D_2$	49 712.11(10)	49 712.052 181	1733	[S5]
$6s15d^1D_2$	49 717.15(10)	49 717.113 078	1107	[S5]
$6s16d^3D_2$	49 818.19(10)	49 818.196 204	-186	[S5]
$6s16d^1D_2$	49 822.08(10)	49 822.053 662	790	[S5]
$6s17d^3D_2$	49 902.78(10)	49 902.799 738	-592	[S5]
$6s17d^1D_2$	49 905.79(10)	49 905.817 418	-822	[S5]
$6s18d^3D_2$	49 971.34(10)	49 971.318 220	653	[S5]
$6s18d^1D_2$	49 973.69(10)	49 973.727 776	-1132	[S5]
$6s19d^3D_2$	50 027.66(10)	50 027.584 183	2273	[S5]
$6s19d^1D_2$	50 029.61(10)	50 029.540 314	2089	[S5]
$6s20d^3D_2$	50 074.44(10)	50 074.353 479	2594	[S5]
$6s20d^1D_2$	50 076.05(10)	50 075.963 231	2601	[S5]
$6s21d^3D_2$	50 113.67(10)	50 113.648 731	638	[S5]
$6s21d^1D_2$	50 115.18(10)	50 114.988 113	5753	[S5]
$6s22d^3D_2$	50 147.03(10)	50 146.981 443	1456	[S5]
$6s22d^1D_2$	50 148.59(10)	50 148.105 296	14 531	[S5]
$6s23d^3D_2$	50 175.499 46(10)	50 175.499 483	-0.62	[S6]
$6s23d^1D_2$	50 176.447 18(10)	50 176.447 102	2.46	[S6]
$6s24d^3D_2$	50 200.087 07(10)	50 200.087 073	-0.04	[S6]
$6s24d^1D_2$	50 200.884 09(10)	50 200.883 990	3.00	[S6]
$6s25d^3D_2$	50 221.433 57(10)	50 221.433 594	-0.64	[S6]
$6s25d^1D_2$	50 222.082 36(10)	50 222.082 084	8.12	[S6]
$6s26d^3D_2$	50 240.035 78(10)	50 240.036 096	-9.62	[S6]
$6s26d^1D_2$	50 240.290 62(10)	50 240.290 082	16.08	[S6]
$4f^{13}5d6s6p A$	50 244.240 35(10)	50 244.240 186	4.92	[S6]
$6s27d^3D_2$	50 256.489 82(10)	50 256.489 876	-1.52	[S6]
$6s27d^1D_2$	50 257.162 36(10)	50 257.162 250	3.21	[S6]
$6s28d^3D_2$	50 270.973 04(10)	50 270.972 964	2.41	[S6]
$6s28d^1D_2$	50 271.516 35(10)	50 271.516 154	5.95	[S6]
$6s29d^3D_2$	50 283.833 88(10)	50 283.833 996	-3.62	[S6]
$6s29d^1D_2$	50 284.302 93(10)	50 284.302 968	-1.06	[S6]
$6s30d^3D_2$	50 295.305 74(10)	50 295.305 673	2.13	[S6]
$6s30d^1D_2$	50 295.718 23(10)	50 295.718 265	-1.06	[S6]
$6s31d^3D_2$	50 305.580 85(10)	50 305.581 001	-4.42	[S6]
$6s31d^1D_2$	50 305.947 57(10)	50 305.947 568	0.15	[S6]
$6s32d^3D_2$	50 314.820 78(10)	50 314.820 687	2.72	[S6]

Table S16 (*continued*)

State label	$\tilde{\nu}_{\text{exp.}}$ ( $\text{cm}^{-1}$ )	$\tilde{\nu}_{\text{th.}}$ ( $\text{cm}^{-1}$ )	$E_{\text{exp.}} - E_{\text{th.}}$ ( $h \cdot \text{MHz}$ )	Ref.
6s32d <sup>1</sup> D <sub>2</sub>	50 315.148 60(10)	50 315.148 549	1.68	[S6]
6s33d <sup>3</sup> D <sub>2</sub>	50 323.159 28(10)	50 323.159 355	-2.26	[S6]
6s33d <sup>1</sup> D <sub>2</sub>	50 323.454 15(10)	50 323.454 139	0.37	[S6]
6s34d <sup>3</sup> D <sub>2</sub>	50 330.710 37(10)	50 330.710 452	-2.42	[S6]
6s34d <sup>1</sup> D <sub>2</sub>	50 330.976 69(10)	50 330.976 663	0.79	[S6]
6s35d <sup>3</sup> D <sub>2</sub>	50 337.570 18(10)	50 337.570 117	1.99	[S6]
6s35d <sup>1</sup> D <sub>2</sub>	50 337.811 62(10)	50 337.811 453	4.92	[S6]
6s36d <sup>3</sup> D <sub>2</sub>	50 343.820 31(10)	50 343.820 258	1.46	[S6]
6s36d <sup>1</sup> D <sub>2</sub>	50 344.039 79(10)	50 344.039 802	-0.29	[S6]
6s37d <sup>3</sup> D <sub>2</sub>	50 349.530 86(10)	50 349.531 006	-4.44	[S6]
6s37d <sup>1</sup> D <sub>2</sub>	50 349.731 40(10)	50 349.731 355	1.26	[S6]
6s38d <sup>3</sup> D <sub>2</sub>	50 354.762 54(10)	50 354.762 686	-4.26	[S6]
6s38d <sup>1</sup> D <sub>2</sub>	50 354.946 00(10)	50 354.946 050	-1.39	[S6]
6s39d <sup>3</sup> D <sub>2</sub>	50 359.567 54(10)	50 359.567 422	3.40	[S6]
6s39d <sup>1</sup> D <sub>2</sub>	50 359.735 65(10)	50 359.735 693	-1.27	[S6]
6s40d <sup>3</sup> D <sub>2</sub>	50 363.990 46(10)	50 363.990 436	0.76	[S6]
6s40d <sup>1</sup> D <sub>2</sub>	50 364.145 30(10)	50 364.145 244	1.70	[S6]
6s41d <sup>3</sup> D <sub>2</sub>	50 368.071 08(10)	50 368.071 117	-1.00	[S6]
6s41d <sup>1</sup> D <sub>2</sub>	50 368.213 92(10)	50 368.213 876	1.21	[S6]
6s42d <sup>3</sup> D <sub>2</sub>	50 371.843 89(10)	50 371.843 904	-0.30	[S6]
6s42d <sup>1</sup> D <sub>2</sub>	50 371.975 78(10)	50 371.975 841	-1.69	[S6]
6s43d <sup>3</sup> D <sub>2</sub>	50 375.338 98(10)	50 375.339 009	-0.91	[S6]
6s43d <sup>1</sup> D <sub>2</sub>	50 375.461 13(10)	50 375.461 200	-2.10	[S6]
6s44d <sup>3</sup> D <sub>2</sub>	50 378.583 09(10)	50 378.583 029	1.83	[S6]
6s44d <sup>1</sup> D <sub>2</sub>	50 378.696 44(10)	50 378.696 417	0.55	[S6]
6s45d <sup>3</sup> D <sub>2</sub>	50 381.599 38(10)	50 381.599 450	-2.23	[S6]
6s45d <sup>1</sup> D <sub>2</sub>	50 381.704 92(10)	50 381.704 865	1.52	[S6]
6s46d <sup>3</sup> D <sub>2</sub>	50 384.409 12(10)	50 384.409 077	1.30	[S6]
6s46d <sup>1</sup> D <sub>2</sub>	50 384.507 12(10)	50 384.507 253	-3.96	[S6]
6s47d <sup>3</sup> D <sub>2</sub>	50 387.030 40(10)	50 387.030 387	0.38	[S6]
6s47d <sup>1</sup> D <sub>2</sub>	50 387.121 93(10)	50 387.121 976	-1.38	[S6]
6s48d <sup>3</sup> D <sub>2</sub>	50 389.479 83(10)	50 389.479 843	-0.45	[S6]
6s48d <sup>1</sup> D <sub>2</sub>	50 389.565 35(10)	50 389.565 424	-2.08	[S6]
6s49d <sup>3</sup> D <sub>2</sub>	50 391.772 08(10)	50 391.772 145	-1.91	[S6]
6s49d <sup>1</sup> D <sub>2</sub>	50 391.852 20(10)	50 391.852 233	-0.91	[S6]
6s50d <sup>3</sup> D <sub>2</sub>	50 393.920 37(10)	50 393.920 454	-2.61	[S6]
6s50d <sup>1</sup> D <sub>2</sub>	50 393.995 48(10)	50 393.995 512	-0.82	[S6]
6s51d <sup>3</sup> D <sub>2</sub>	50 395.936 56(10)	50 395.936 583	-0.63	[S6]
6s51d <sup>1</sup> D <sub>2</sub>	50 396.006 94(10)	50 396.007 025	-2.44	[S6]
6s52d <sup>3</sup> D <sub>2</sub>	50 397.831 14(10)	50 397.831 157	-0.55	[S6]
6s52d <sup>1</sup> D <sub>2</sub>	50 397.897 32(10)	50 397.897 355	-1.12	[S6]
6s53d <sup>3</sup> D <sub>2</sub>	50 399.613 77(10)	50 399.613 755	0.50	[S6]
6s53d <sup>1</sup> D <sub>2</sub>	50 399.676 02(10)	50 399.676 045	-0.89	[S6]
6s54d <sup>3</sup> D <sub>2</sub>	50 401.292 93(10)	50 401.293 031	-2.90	[S6]
6s54d <sup>1</sup> D <sub>2</sub>	50 401.351 71(10)	50 401.351 714	-0.18	[S6]
6s55d <sup>3</sup> D <sub>2</sub>	50 402.876 70(10)	50 402.876 817	-3.62	[S6]
6s55d <sup>1</sup> D <sub>2</sub>	50 402.932 00(10)	50 402.932 168	-5.00	[S6]
6s56d <sup>3</sup> D <sub>2</sub>	50 404.372 20(10)	50 404.372 219	-0.65	[S6]
6s56d <sup>1</sup> D <sub>2</sub>	50 404.424 37(10)	50 404.424 486	-3.56	[S6]
6s57d <sup>3</sup> D <sub>2</sub>	50 405.785 64(10)	50 405.785 692	-1.51	[S6]
6s57d <sup>1</sup> D <sub>2</sub>	50 405.835 01(10)	50 405.835 101	-2.75	[S6]
6s58d <sup>3</sup> D <sub>2</sub>	50 407.123 10(10)	50 407.123 115	-0.45	[S6]
6s58d <sup>1</sup> D <sub>2</sub>	50 407.169 80(10)	50 407.169 870	-2.13	[S6]
6s59d <sup>3</sup> D <sub>2</sub>	50 408.389 84(10)	50 408.389 847	-0.11	[S6]
6s59d <sup>1</sup> D <sub>2</sub>	50 408.434 01(10)	50 408.434 135	-3.85	[S6]
6s60d <sup>3</sup> D <sub>2</sub>	50 409.590 67(10)	50 409.590 782	-3.25	[S6]
6s60d <sup>1</sup> D <sub>2</sub>	50 409.632 64(10)	50 409.632 776	-4.15	[S6]

Table S16 (*continued*)

State label	$\tilde{\nu}_{\text{exp.}}$ ( $\text{cm}^{-1}$ )	$\tilde{\nu}_{\text{th.}}$ ( $\text{cm}^{-1}$ )	$E_{\text{exp.}} - E_{\text{th.}}$ ( $h \cdot \text{MHz}$ )	Ref.
6s61d <sup>3</sup> D <sub>2</sub>	50 410.730 33(10)	50 410.730 401	-2.17	[S6]
6s61d <sup>1</sup> D <sub>2</sub>	50 410.770 16(10)	50 410.770 255	-2.95	[S6]
6s62d <sup>3</sup> D <sub>2</sub>	50 411.812 74(10)	50 411.812 808	-1.89	[S6]
6s62d <sup>1</sup> D <sub>2</sub>	50 411.850 64(10)	50 411.850 666	-0.83	[S6]
6s63d <sup>3</sup> D <sub>2</sub>	50 412.841 59(10)	50 412.841 769	-5.35	[S6]
6s63d <sup>1</sup> D <sub>2</sub>	50 412.877 75(10)	50 412.877 762	-0.41	[S6]
6s64d <sup>3</sup> D <sub>2</sub>	50 413.820 73(10)	50 413.820 745	-0.33	[S6]
6s64d <sup>1</sup> D <sub>2</sub>	50 413.854 96(10)	50 413.854 994	-1.08	[S6]
6s65d <sup>3</sup> D <sub>2</sub>	50 414.752 98(10)	50 414.752 923	1.68	[S6]
6s65d <sup>1</sup> D <sub>2</sub>	50 414.785 47(10)	50 414.785 539	-2.12	[S6]
6s66d <sup>3</sup> D <sub>2</sub>	50 415.641 26(10)	50 415.641 238	0.65	[S6]
6s66d <sup>1</sup> D <sub>2</sub>	50 415.672 42(10)	50 415.672 324	2.74	[S6]
6s67d <sup>3</sup> D <sub>2</sub>	50 416.488 38(10)	50 416.488 400	-0.64	[S6]
6s67d <sup>1</sup> D <sub>2</sub>	50 416.518 07(10)	50 416.518 050	0.52	[S6]
6s68d <sup>3</sup> D <sub>2</sub>	50 417.296 94(10)	50 417.296 913	0.78	[S6]
6s68d <sup>1</sup> D <sub>2</sub>	50 417.325 29(10)	50 417.325 213	2.37	[S6]
6s69d <sup>3</sup> D <sub>2</sub>	50 418.069 21(10)	50 418.069 091	3.44	[S6]
6s69d <sup>1</sup> D <sub>2</sub>	50 418.096 09(10)	50 418.096 123	-0.93	[S6]
6s70d <sup>3</sup> D <sub>2</sub>	50 418.807 12(10)	50 418.807 080	1.10	[S6]
6s70d <sup>1</sup> D <sub>2</sub>	50 418.833 00(10)	50 418.832 919	2.46	[S6]
6s71d <sup>3</sup> D <sub>2</sub>	50 419.512 87(10)	50 419.512 869	0.08	[S6]
6s71d <sup>1</sup> D <sub>2</sub>	50 419.537 69(10)	50 419.537 584	3.15	[S6]
6s72d <sup>3</sup> D <sub>2</sub>	50 420.188 34(10)	50 420.188 305	1.02	[S6]
6s72d <sup>1</sup> D <sub>2</sub>	50 420.212 02(10)	50 420.211 959	1.88	[S6]
6s73d <sup>3</sup> D <sub>2</sub>	50 420.835 12(10)	50 420.835 102	0.53	[S6]
6s73d <sup>1</sup> D <sub>2</sub>	50 420.857 74(10)	50 420.857 757	-0.63	[S6]
6s74d <sup>3</sup> D <sub>2</sub>	50 421.455 12(10)	50 421.454 858	7.69	[S6]
6s74d <sup>1</sup> D <sub>2</sub>	50 421.476 50(10)	50 421.476 569	-2.15	[S6]
6s75d <sup>3</sup> D <sub>2</sub>	50 422.049 16(10)	50 422.049 060	3.01	[S6]
6s75d <sup>1</sup> D <sub>2</sub>	50 422.069 91(10)	50 422.069 877	0.89	[S6]
6s76d <sup>3</sup> D <sub>2</sub>	50 422.619 15(10)	50 422.619 092	1.86	[S6]
6s76d <sup>1</sup> D <sub>2</sub>	50 422.639 24(10)	50 422.639 066	5.08	[S6]
6s77d <sup>3</sup> D <sub>2</sub>	50 423.166 27(10)	50 423.166 249	0.52	[S6]
6s77d <sup>1</sup> D <sub>2</sub>	50 423.185 41(10)	50 423.185 423	-0.33	[S6]
6s78d <sup>3</sup> D <sub>2</sub>	50 423.691 83(10)	50 423.691 737	2.74	[S6]
6s78d <sup>1</sup> D <sub>2</sub>	50 423.710 18(10)	50 423.710 155	0.63	[S6]
6s79d <sup>3</sup> D <sub>2</sub>	50 424.196 85(10)	50 424.196 688	4.75	[S6]
6s79d <sup>1</sup> D <sub>2</sub>	50 424.214 46(10)	50 424.214 387	2.12	[S6]
6s80d <sup>3</sup> D <sub>2</sub>	50 424.682 12(10)	50 424.682 155	-1.21	[S6]
6s80d <sup>1</sup> D <sub>2</sub>	50 424.699 26(10)	50 424.699 174	2.56	[S6]

Table S17: Spectroscopic data of  $n^1D_2 \leftrightarrow n'^1D_2$  Rydberg-Rydberg transitions obtained by microwave spectroscopy, as presented in Ref. [S7] and Ref. [S6].

$f$	$i$	$\Delta E_{f \leftarrow i}^{\text{exp.}}$ ( $h \cdot \text{MHz}$ )	$\Delta E_{f \leftarrow i}^{\text{theo.}}$ ( $h \cdot \text{MHz}$ )	$E_{\text{exp.}} - E_{\text{th.}}$ ( $h \cdot \text{MHz}$ )	Ref.
6s33d <sup>1</sup> D <sub>2</sub>	6s32d <sup>1</sup> D <sub>2</sub>	248 996.64(28)	248 995.32	1.32	[S6]
6s34d <sup>1</sup> D <sub>2</sub>	6s33d <sup>1</sup> D <sub>2</sub>	225 519.66(12)	225 519.59	0.07	[S6]
6s35d <sup>1</sup> D <sub>2</sub>	6s34d <sup>1</sup> D <sub>2</sub>	204 902.10(12)	204 901.85	0.25	[S6]
6s36d <sup>1</sup> D <sub>2</sub>	6s35d <sup>1</sup> D <sub>2</sub>	186 721.48(12)	186 721.21	0.27	[S6]
6s37d <sup>1</sup> D <sub>2</sub>	6s36d <sup>1</sup> D <sub>2</sub>	170 628.56(14)	170 628.47	0.09	[S6]
6s38d <sup>1</sup> D <sub>2</sub>	6s37d <sup>1</sup> D <sub>2</sub>	156 333.20(14)	156 332.64	0.56	[S6]
6s39d <sup>1</sup> D <sub>2</sub>	6s38d <sup>1</sup> D <sub>2</sub>	143 589.46(8)	143 589.88	-0.42	[S6]
6s40d <sup>1</sup> D <sub>2</sub>	6s39d <sup>1</sup> D <sub>2</sub>	132 194.90(80)	132 195.01	-0.11	[S7]
6s41d <sup>1</sup> D <sub>2</sub>	6s40d <sup>1</sup> D <sub>2</sub>	121 974.42(80)	121 974.51	-0.09	[S7]

Table S17 (continued)

$f$	$i$	$\Delta E_{f \leftarrow i}^{\text{exp.}} (h \cdot \text{MHz})$	$\Delta E_{f \leftarrow i}^{\text{theo.}} (h \cdot \text{MHz})$	$E_{\text{exp.}} - E_{\text{th.}}$ ( $h \cdot \text{MHz}$ )	Ref.
$6s42d^1D_2$	$6s41d^1D_2$	112 780.92(80)	112 780.89	0.03	[S7]
$6s43d^1D_2$	$6s42d^1D_2$	104 488.90(80)	104 488.42	0.48	[S7]
$6s44d^1D_2$	$6s43d^1D_2$	96 989.66(80)	96 989.35	0.31	[S7]
$6s45d^1D_2$	$6s44d^1D_2$	90 191.26(80)	90 191.02	0.24	[S7]
$6s46d^1D_2$	$6s45d^1D_2$	84 013.80(80)	84 013.47	0.33	[S7]
$6s47d^1D_2$	$6s46d^1D_2$	78 387.84(80)	78 387.43	0.41	[S7]
$6s48d^1D_2$	$6s47d^1D_2$	73 253.24(80)	73 252.71	0.53	[S7]
$6s49d^1D_2$	$6s48d^1D_2$	68 557.18(80)	68 556.83	0.35	[S7]
$6s50d^1D_2$	$6s49d^1D_2$	64 254.32(80)	64 253.89	0.43	[S7]
$6s51d^1D_2$	$6s50d^1D_2$	60 303.62(80)	60 303.64	-0.02	[S7]
$6s52d^1D_2$	$6s51d^1D_2$	56 670.98(80)	56 670.67	0.31	[S7]
$6s53d^1D_2$	$6s52d^1D_2$	53 324.24(80)	53 323.76	0.48	[S7]
$6s54d^1D_2$	$6s53d^1D_2$	50 235.96(80)	50 235.30	0.66	[S7]
$6s55d^1D_2$	$6s54d^1D_2$	47 381.44(80)	47 380.81	0.63	[S7]
$6s56d^1D_2$	$6s55d^1D_2$	44 739.32(80)	44 738.56	0.76	[S7]

D.  $^{174}\text{Yb } 1,3P_1$ Table S18: Spectroscopic data of  $n^{1,3}P_1 \leftrightarrow n'^1S_0$  Rydberg-Rydberg transitions obtained by microwave spectroscopy in an atomic beam setup as described in App. B of the main text and from Ref. [S8].

$f$	$i$	$\nu_{f \leftarrow i}$ (MHz)	$\tilde{\nu}_{\text{exp.}}$ ( $\text{cm}^{-1}$ )	$\tilde{\nu}_{\text{th.}}$ ( $\text{cm}^{-1}$ )	$E_{\text{exp.}} - E_{\text{th.}}$ ( $h \cdot \text{MHz}$ )	Ref.
$6s30p^1P_1$	$6s30s^1S_0$	125 083.25(10)	50 281.494 629	50 281.494 630	-0.02	This work
$6s31p^1P_1$	$6s31s^1S_0$	111 552.79(10)	50 293.204 338	50 293.204 334	0.14	This work
$6s32p^1P_1$	$6s32s^1S_0$	99 908.78(10)	50 303.686 967	50 303.686 965	0.07	This work
$6s33p^1P_1$	$6s33s^1S_0$	89 832.20(10)	50 313.107 919	50 313.107 921	-0.05	This work
$6s37p^1P_1$	$6s38s^1S_0$	-118 631.36(10)	50 342.640 744	50 342.640 748	-0.12	This work
$6s38p^1P_1$	$6s39s^1S_0$	-108 614.16(10)	50 348.449 399	50 348.449 403	-0.11	This work
$6s39p^1P_1$	$6s40s^1S_0$	-99 693.21(10)	50 353.768 507	50 353.768 511	-0.13	This work
$6s42p^3P_1$	$6s41s^1S_0$	122 420.24(10)	50 365.794 584	50 365.794 585	-0.01	This work
$6s43p^3P_1$	$6s42s^1S_0$	110 051.61(10)	50 369.637 081	50 369.637 080	0.03	This work
$6s44p^3P_1$	$6s43s^1S_0$	99 037.2(5)	50 373.199 534	50 373.199 536	-0.05	[S8]
$6s44p^3P_1$	$6s43s^1S_0$	99 037.32(10)	50 373.199 538	50 373.199 536	0.06	This work
$6s45p^3P_1$	$6s44s^1S_0$	89 241.46(10)	50 376.509 732	50 376.509 732	-0.02	This work
$6s46p^3P_1$	$6s45s^1S_0$	80 542.0(5)	50 379.591 985	50 379.591 983	0.07	[S8]
$6s47p^3P_1$	$6s46s^1S_0$	72 826.1(5)	50 382.467 571	50 382.467 572	-0.03	[S8]
$6s48p^3P_1$	$6s47s^1S_0$	65 989.5(5)	50 385.155 155	50 385.155 158	-0.08	[S8]
$6s48p^1P_1$	$6s47s^1S_0$	106 947.8(5)	50 386.521 377	50 386.521 371	0.18	[S8]
$6s49p^3P_1$	$6s48s^1S_0$	59 934.5(5)	50 387.671 122	50 387.671 139	-0.51	[S8]
$6s49p^1P_1$	$6s48s^1S_0$	99 874.4(5)	50 389.003 373	50 389.003 366	0.22	[S8]
$6s50p^3P_1$	$6s49s^1S_0$	54 572.3(5)	50 390.029 982	50 390.029 985	-0.12	[S8]
$6s50p^1P_1$	$6s49s^1S_0$	93 411.1(5)	50 391.325 504	50 391.325 500	0.14	[S8]
$6s51p^3P_1$	$6s50s^1S_0$	49 819.2(5)	50 392.244 528	50 392.244 533	-0.17	[S8]
$6s51p^1P_1$	$6s50s^1S_0$	87 493.7(5)	50 393.501 214	50 393.501 209	0.15	[S8]
$6s52p^3P_1$	$6s51s^1S_0$	45 601.0(5)	50 394.326 221	50 394.326 230	-0.28	[S8]
$6s52p^1P_1$	$6s51s^1S_0$	82 065.6(5)	50 395.542 549	50 395.542 548	0.05	[S8]
$6s53p^1P_1$	$6s52s^1S_0$	77 077.5(5)	50 397.460 359	50 397.460 355	0.11	[S8]
$6s54p^3P_1$	$6s52s^1S_0$	97 186.4(5)	50 398.131 119	50 398.131 122	-0.08	[S8]
$6s54p^1P_1$	$6s53s^1S_0$	72 485.4(5)	50 399.264 399	50 399.264 400	-0.02	[S8]
$6s55p^3P_1$	$6s53s^1S_0$	90 699.2(5)	50 399.871 946	50 399.871 948	-0.06	[S8]
$6s55p^1P_1$	$6s54s^1S_0$	68 251.0(5)	50 400.963 502	50 400.963 504	-0.06	[S8]
$6s56p^3P_1$	$6s54s^1S_0$	84 797.5(5)	50 401.515 433	50 401.515 435	-0.06	[S8]
$6s57p^3P_1$	$6s55s^1S_0$	79 415.9(5)	50 403.068 521	50 403.068 524	-0.11	[S8]
$6s58p^3P_1$	$6s56s^1S_0$	74 497.4(5)	50 404.537 556	50 404.537 558	-0.08	[S8]
$6s59p^3P_1$	$6s57s^1S_0$	69 992.0(5)	50 405.928 346	50 405.928 348	-0.06	[S8]
$6s59p^1P_1$	$6s57s^1S_0$	97 906.5(5)	50 406.859 474	50 406.859 474	-0.03	[S8]
$6s60p^3P_1$	$6s58s^1S_0$	65 856.0(5)	50 407.246 219	50 407.246 223	-0.10	[S8]
$6s60p^1P_1$	$6s58s^1S_0$	92 647.5(5)	50 408.139 887	50 408.139 888	-0.02	[S8]
$6s61p^3P_1$	$6s58s^1S_0$	103 325.9(5)	50 408.496 080	50 408.496 078	0.06	[S8]
$6s61p^1P_1$	$6s59s^1S_0$	87 758.5(5)	50 409.353 576	50 409.353 577	-0.04	[S8]
$6s62p^3P_1$	$6s59s^1S_0$	97 617.1(5)	50 409.682 423	50 409.682 420	0.10	[S8]
$6s62p^1P_1$	$6s60s^1S_0$	83 207.5(5)	50 410.505 095	50 410.505 098	-0.11	[S8]
$6s63p^3P_1$	$6s60s^1S_0$	92 330.3(5)	50 410.809 398	50 410.809 396	0.08	[S8]
$6s63p^1P_1$	$6s61s^1S_0$	78 965.8(5)	50 411.598 618	50 411.598 625	-0.20	[S8]
$6s64p^3P_1$	$6s61s^1S_0$	87 426.4(5)	50 411.880 834	50 411.880 831	0.09	[S8]
$6s64p^1P_1$	$6s62s^1S_0$	75 007.7(5)	50 412.637 982	50 412.637 988	-0.18	[S8]
$6s65p^3P_1$	$6s62s^1S_0$	82 870.6(5)	50 412.900 260	50 412.900 254	0.17	[S8]
$6s65p^1P_1$	$6s63s^1S_0$	71 309.8(5)	50 413.626 699	50 413.626 704	-0.15	[S8]

Table S19: Spectroscopic data of  $n^{1,3}P_1 \leftrightarrow n'^{1,3}D_2$  Rydberg-Rydberg transitions obtained by microwave spectroscopy in an atomic beam setup as described in App. B of the main text and from Ref. [S8].

$f$	$i$	$\nu_{f \leftarrow i}$ (MHz)	$\tilde{\nu}_{\text{exp.}}$ ( $\text{cm}^{-1}$ )	$\tilde{\nu}_{\text{th.}}$ ( $\text{cm}^{-1}$ )	$E_{\text{exp.}} - E_{\text{th.}}$ ( $h \cdot \text{MHz}$ )	Ref.
$6s31p^1P_1$	$6s30d^3D_2$	-114 223.63(10)	50 291.495 583	50 291.495 586	-0.09	This work
$6s32p^1P_1$	$6s31d^3D_2$	-106 695.56(10)	50 302.022 020	50 302.022 017	0.08	This work
$6s34p^1P_1$	$6s33d^3D_2$	-94 535.43(10)	50 320.005 993	50 320.005 989	0.11	This work
$6s35p^1P_1$	$6s34d^3D_2$	-89 631.26(10)	50 327.720 675	50 327.720 672	0.09	This work
$6s36p^1P_1$	$6s35d^3D_2$	-85 360.87(10)	50 334.722 784	50 334.722 784	0.01	This work
$6s37p^1P_1$	$6s36d^3D_2$	-81 628.49(10)	50 341.097 425	50 341.097 427	-0.06	This work
$6s38p^1P_1$	$6s37d^3D_2$	-78 347.73(10)	50 346.917 607	50 346.917 609	-0.06	This work
$6s39p^1P_1$	$6s38d^3D_2$	-75 439.74(10)	50 352.246 287	50 352.246 291	-0.12	This work
$6s40p^1P_1$	$6s39d^3D_2$	-72 831.25(10)	50 357.138 033	50 357.138 035	-0.09	This work
$6s41p^1P_1$	$6s40d^3D_2$	-70 454.79(10)	50 361.640 317	50 361.640 319	-0.07	This work
$6s42p^1P_1$	$6s40d^1D_2$	94 245.3(5)	50 367.288 929	50 367.288 925	0.13	[S8]
$6s43p^1P_1$	$6s41d^1D_2$	87 090.9(5)	50 371.118 916	50 371.118 910	0.15	[S8]
$6s44p^1P_1$	$6s42d^1D_2$	80 642.9(5)	50 374.665 799	50 374.665 793	0.19	[S8]
$6s45p^1P_1$	$6s43d^1D_2$	74 816.2(5)	50 377.956 800	50 377.956 793	0.22	[S8]
$6s45p^1P_1$	$6s42d^3D_2$	139 878.25(10)	50 376.509 740	50 376.509 732	0.23	This work
$6s46p^1P_1$	$6s44d^1D_2$	69 537.7(5)	50 381.015 945	50 381.015 938	0.20	[S8]
$6s47p^1P_1$	$6s45d^1D_2$	64 744.7(5)	50 383.864 516	50 383.864 501	0.44	[S8]
$6s52p^1P_1$	$6s49d^3D_2$	76 569.51(10)	50 394.326 229	50 394.326 230	-0.05	This work
$6s56p^1P_1$	$6s53d^1D_2$	86 628.3(5)	50 402.565 654	50 402.565 649	0.14	[S8]
$6s57p^1P_1$	$6s54d^1D_2$	81 734.3(5)	50 404.078 077	50 404.078 075	0.07	[S8]
$6s58p^1P_1$	$6s55d^1D_2$	77 202.2(5)	50 405.507 356	50 405.507 355	0.03	[S8]

Table S20: Laser spectroscopic data of the  $6snp^{1,3}P_1$  Rydberg series included in the determination of the MQDT models. The state energies and the respective uncertainties are taken from Refs. [S2, S9].

State label	$\tilde{\nu}_{\text{exp.}}$ ( $\text{cm}^{-1}$ )	$\tilde{\nu}_{\text{th.}}$ ( $\text{cm}^{-1}$ )	$E_{\text{exp.}} - E_{\text{th.}}$ ( $h \cdot \text{MHz}$ )	Ref.
$6s12p^1P_1$	48 719.18(10)	48 719.416 230	-6954	[S9]
$6s12p^3P_1$	48 761.81(10)	48 763.202 662	-41 756	[S9]
$4f^{13}5d^26s A$	49 005.89(10)	49 006.059 508	-5082	[S9]
$6s13p^3P_1$	49 110.07(10)	49 107.770 988	68 918	[S9]
$6s13p^1P_1$	49 127.40(10)	49 127.675 624	-8263	[S9]
$6s14p^1P_1$	49 352.44(10)	49 352.942 891	-15 206	[S9]
$6s14p^3P_1$	49 360.60(10)	49 359.516 364	32 481	[S9]
$6s15p^1P_1$	49 536.42(10)	49 537.093 278	-20 296	[S9]
$6s15p^3P_1$	49 546.55(10)	49 545.470 131	32 369	[S9]
$6s16p^1P_1$	49 677.79(10)	49 678.008 399	-6425	[S9]
$6s16p^3P_1$	49 688.55(10)	49 687.624 822	27 731	[S9]
$6s17p^1P_1$	49 786.40(10)	49 786.407 461	-347	[S9]
$6s17p^3P_1$	49 799.20(10)	49 798.493 431	21 177	[S9]
$6s18p^1P_1$	49 867.12(10)	49 866.780 676	10 025	[S9]
$6s18p^3P_1$	49 886.92(10)	49 886.553 028	10 997	[S9]
$4f^{13}5d^26s B$	49 920.00(10)	49 919.800 148	5991	[S2]
$6s19p^3P_1$	49 957.87(10)	49 957.619 220	7513	[S2]
$6s19p^1P_1$	49 969.14(10)	49 969.330 880	-5853	[S2]
$6s20p^3P_1$	50 015.96(10)	50 015.798 337	4842	[S2]
$6s20p^1P_1$	50 021.28(10)	50 021.406 997	-3856	[S2]
$6s21p^3P_1$	50 064.12(10)	50 064.064 042	1672	[S2]
$6s21p^1P_1$	50 067.83(10)	50 067.818 312	368	[S2]
$6s22p^3P_1$	50 104.64(10)	50 104.582 172	1728	[S2]
$6s22p^1P_1$	50 107.66(10)	50 107.598 166	1998	[S2]
$6s23p^3P_1$	50 138.99(10)	50 138.939 066	1522	[S2]
$6s23p^1P_1$	50 141.54(10)	50 141.577 594	-979	[S2]
$6s24p^3P_1$	50 168.38(10)	50 168.323 080	1701	[S2]

Table S20 (*continued*)

State label	$\tilde{\nu}_{\text{exp.}}$ ( $\text{cm}^{-1}$ )	$\tilde{\nu}_{\text{th.}}$ ( $\text{cm}^{-1}$ )	$E_{\text{exp.}} - E_{\text{th.}}$ ( $h \cdot \text{MHz}$ )	Ref.
$6s24p^1P_1$	50 170.82(10)	50 170.724 685	2713	[S2]
$6s25p^3P_1$	50 193.66(10)	50 193.645 993	415	[S2]
$6s25p^1P_1$	50 195.86(10)	50 195.876 945	-533	[S2]
$6s26p^3P_1$	50 215.64(10)	50 215.619 621	606	[S2]
$6s26p^1P_1$	50 217.65(10)	50 217.717 500	-1896	[S2]
$6s27p^3P_1$	50 234.85(10)	50 234.806 844	1289	[S2]
$6s27p^1P_1$	50 236.83(10)	50 236.796 508	1029	[S2]
$6s28p^3P_1$	50 251.74(10)	50 251.657 502	2468	[S2]
$6s28p^1P_1$	50 253.58(10)	50 253.557 333	652	[S2]
$6s29p^3P_1$	50 266.66(10)	50 266.534 501	3758	[S2]
$6s29p^1P_1$	50 268.44(10)	50 268.359 101	2407	[S2]

E.  $^{174}\text{Yb } ^3P_2$ Table S21: Spectroscopic data of the  $n^3P_2$  Rydberg series obtained by microwave spectroscopy in an atomic beam setup as described in App. B of the main text and from Ref. [S8].

$f$	$i$	$\nu_{f \leftarrow i}$ (MHz)	$\tilde{\nu}_{\text{exp.}}$ ( $\text{cm}^{-1}$ )	$\tilde{\nu}_{\text{th.}}$ ( $\text{cm}^{-1}$ )	$E_{\text{exp.}} - E_{\text{th.}}$ ( $h \cdot \text{MHz}$ )	Ref.
$6s31p^3P_2$	$6s30d^3D_2$	-54 957.40(10)	50 293.472 491	50 293.472 497	-0.16	This work
$6s36p^3P_2$	$6s34d^3D_2$	172 078.74(10)	50 336.450 381	50 336.450 366	0.46	This work
$6s37p^3P_2$	$6s35d^3D_2$	156 685.04(10)	50 342.796 567	50 342.796 557	0.30	This work
$6s38p^3P_2$	$6s36d^3D_2$	143 074.41(10)	50 348.592 707	50 348.592 706	0.03	This work
$6s39p^3P_2$	$6s37d^3D_2$	130 996.14(10)	50 353.900 567	50 353.900 572	-0.15	This work
$6s40p^3P_2$	$6s38d^3D_2$	120 240.54(10)	50 358.773 479	50 358.773 486	-0.21	This work
$6s43p^3P_2$	$6s41d^3D_2$	94 279.05(10)	50 371.215 928	50 371.215 944	-0.49	This work
$6s43p^3P_2$	$6s41d^3D_2$	94 279.0(5)	50 371.215 926	50 371.215 944	-0.53	[S8]
$6s44p^3P_2$	$6s42d^3D_2$	87 302.7(5)	50 374.756 008	50 374.756 022	-0.39	[S8]
$6s45p^3P_2$	$6s43d^3D_2$	80 998.1(5)	50 378.040 815	50 378.040 830	-0.44	[S8]
$6s46p^3P_2$	$6s44d^3D_2$	75 286.6(5)	50 381.094 320	50 381.094 330	-0.30	[S8]
$6s47p^3P_2$	$6s45d^3D_2$	70 099.8(5)	50 383.937 728	50 383.937 737	-0.26	[S8]
$6s48p^3P_2$	$6s46d^3D_2$	65 378.8(5)	50 386.589 879	50 386.589 888	-0.29	[S8]
$6s49p^3P_2$	$6s47d^3D_2$	61 072.4(5)	50 389.067 543	50 389.067 557	-0.42	[S8]
$6s50p^3P_2$	$6s48d^3D_2$	57 136.5(5)	50 391.385 711	50 391.385 718	-0.21	[S8]
$6s51p^3P_2$	$6s49d^3D_2$	53 531.7(5)	50 393.557 770	50 393.557 773	-0.10	[S8]
$6s52p^3P_2$	$6s50d^3D_2$	50 224.0(5)	50 395.595 746	50 395.595 745	0.03	[S8]
$6s53p^3P_2$	$6s51d^3D_2$	47 183.3(5)	50 397.510 448	50 397.510 446	0.07	[S8]
$6s54p^3P_2$	$6s51d^3D_2$	101 181.5(5)	50 399.311 634	50 399.311 620	0.43	[S8]
$6s55p^3P_2$	$6s52d^3D_2$	95 241.7(5)	50 401.008 078	50 401.008 067	0.36	[S8]
$6s56p^3P_2$	$6s53d^3D_2$	89 758.1(5)	50 402.607 763	50 402.607 749	0.42	[S8]
$6s57p^3P_2$	$6s54d^3D_2$	84 687.7(5)	50 404.117 908	50 404.117 889	0.58	[S8]
$6s58p^3P_2$	$6s55d^3D_2$	79 992.0(5)	50 405.545 063	50 405.545 045	0.52	[S8]
$6s59p^3P_2$	$6s56d^3D_2$	75 637.4(5)	50 406.895 211	50 406.895 188	0.67	[S8]
$6s60p^3P_2$	$6s57d^3D_2$	71 593.1(5)	50 408.173 781	50 408.173 761	0.61	[S8]
$6s61p^3P_2$	$6s58d^3D_2$	67 832.0(5)	50 409.385 747	50 409.385 732	0.45	[S8]
$6s62p^3P_2$	$6s58d^3D_2$	102 306.0(5)	50 410.535 676	50 410.535 650	0.79	[S8]
$6s63p^3P_2$	$6s59d^3D_2$	97 068.5(5)	50 411.627 703	50 411.627 677	0.78	[S8]
$6s64p^3P_2$	$6s60d^3D_2$	92 182.6(5)	50 412.665 663	50 412.665 637	0.79	[S8]
$6s65p^3P_2$	$6s61d^3D_2$	87 619.3(5)	50 413.653 067	50 413.653 039	0.84	[S8]
$6s66p^3P_2$	$6s62d^3D_2$	83 352.3(5)	50 414.593 141	50 414.593 114	0.82	[S8]
$6s67p^3P_2$	$6s63d^3D_2$	79 358.0(5)	50 415.488 867	50 415.488 839	0.81	[S8]
$6s68p^3P_2$	$6s64d^3D_2$	75 615.0(5)	50 416.342 990	50 416.342 961	0.86	[S8]
$6s69p^3P_2$	$6s65d^3D_2$	72 103.7(5)	50 417.158 043	50 417.158 016	0.81	[S8]
$6s70p^3P_2$	$6s66d^3D_2$	68 806.7(5)	50 417.936 383	50 417.936 351	0.94	[S8]
$6s71p^3P_2$	$6s67d^3D_2$	65 707.5(5)	50 418.680 167	50 418.680 139	0.83	[S8]
$6s72p^3P_2$	$6s68d^3D_2$	62 791.9(5)	50 419.391 425	50 419.391 394	0.92	[S8]
$6s73p^3P_2$	$6s69d^3D_2$	60 046.2(5)	50 420.072 017	50 420.071 987	0.90	[S8]
$6s74p^3P_2$	$6s70d^3D_2$	57 458.5(5)	50 420.723 690	50 420.723 654	1.06	[S8]
$6s75p^3P_2$	$6s71d^3D_2$	55 017.0(5)	50 421.348 039	50 421.348 012	0.80	[S8]
$6s76p^3P_2$	$6s72d^3D_2$	52 712.0(5)	50 421.946 588	50 421.946 566	0.66	[S8]

Table S22: Laser spectroscopic data of the  $6sn p^3 P_2$  Rydberg series included in the determination of the MQDT model. The state energies and the respective uncertainties are taken from Ref. [S2].

State label	$\tilde{\nu}_{\text{exp.}}$ ( $\text{cm}^{-1}$ )	$\tilde{\nu}_{\text{th.}}$ ( $\text{cm}^{-1}$ )	$E_{\text{exp.}} - E_{\text{th.}}$ ( $h \cdot \text{MHz}$ )	Ref.
$6s9p^3 P_2$	46 184.15	46 159.155 515	749 316	[S10]
$6s10p^3 P_2$	47 471.10	47 476.475 100	-161 141	[S10]
$6s11p^3 P_2$	48 233.7(5)	48 251.376 961	-529 942	[S11]
$6s12p^3 P_2$	48 745.6(5)	48 741.398 200	125 967	[S12]
$4f^{13}6s5d^2^3 P_2$	48 965.15	48 961.554 736	112 280	[S13]
$6s13p^3 P_2$	49 136.4(5)	49 138.766 072	-70 933	[S12]
$6s14p^3 P_2$	49 370.5(5)	49 372.087 230	-47 584	[S12]
$6s15p^3 P_2$	49 553.0(5)	49 553.219 876	-6592	[S12]
$6s16p^3 P_2$	49 692.7(5)	49 690.324 708	71 209	[S12]
$4f^{13}6s5d^2^1 D_2$	49 751.89	49 737.646 161	427 319	[S13]
$6s17p^3 P_2$	49 805.6(5)	49 805.731 817	-3952	[S12]
$6s18p^3 P_2$	49 891.51(10)	49 891.644 895	-4044	[S2]
$6s19p^3 P_2$	49 961.83(10)	49 961.875 954	-1378	[S2]
$6s20p^3 P_2$	50 019.65(10)	50 019.606 364	1308	[S2]
$6s21p^3 P_2$	50 067.61(10)	50 067.578 929	931	[S2]
$6s22p^3 P_2$	50 107.90(10)	50 107.858 387	1248	[S2]
$6s23p^3 P_2$	50 142.00(10)	50 141.999 179	25	[S2]
$6s24p^3 P_2$	50 171.19(10)	50 171.184 915	152	[S2]
$6s25p^3 P_2$	50 196.37(10)	50 196.328 275	1251	[S2]
$6s26p^3 P_2$	50 218.17(10)	50 218.141 668	849	[S2]
$6s27p^3 P_2$	50 237.20(10)	50 237.187 508	374	[S2]
$6s28p^3 P_2$	50 253.96(10)	50 253.914 481	1365	[S2]
$6s29p^3 P_2$	50 268.74(10)	50 268.683 999	1679	[S2]
$6s30p^3 P_2$	50 281.83(10)	50 281.789 781	1206	[S2]

F.  $^{174}\text{Yb } ^3P_0$ Table S23: Spectroscopic data of the  $n^3P_0$  Rydberg series obtained by microwave spectroscopy in an atomic beam setup as described in App. B of the main text and from Ref. [S8].

$f$	$i$	$\Delta E_{f \leftarrow i}^{\text{exp}} (h \cdot \text{MHz})$	$\tilde{\nu}_{\text{exp.}} (\text{cm}^{-1})$	$\tilde{\nu}_{\text{th.}} (\text{cm}^{-1})$	$E_{\text{exp.}} - E_{\text{th.}} (h \cdot \text{MHz})$	Ref.
$6s31p^3P_0$	$6s30d^3D_2$	-218 431.0(10)	50 288.019 600	50 288.019 606	-0.18	This work
$6s32p^3P_0$	$6s31d^3D_2$	-202 698.6(10)	50 298.819 704	50 298.819 689	0.43	This work
$6s34p^3P_0$	$6s33d^3D_2$	-174 533.8(10)	50 317.337 535	50 317.337 507	0.83	This work
$6s35p^3P_0$	$6s34d^3D_2$	-161 992.9(10)	50 325.306 952	50 325.307 034	-2.48	This work
$6s36p^3P_0$	$6s35d^3D_2$	-150 399.2(10)	50 332.553 339	50 332.553 286	1.56	This work
$6s50p^3P_0$	$6s47d^3D_2$	83 958.5(10)	50 389.830 942	50 389.830 943	-0.01	This work

Table S24: Laser spectroscopic data of the  $6snp^3P_0$  Rydberg series included in the determination of the MQDT model. The state energies and the respective uncertainties are taken from Ref. [S2].

State label	$\tilde{\nu}_{\text{exp.}} (\text{cm}^{-1})$	$\tilde{\nu}_{\text{th.}} (\text{cm}^{-1})$	$E_{\text{exp.}} - E_{\text{th.}} (h \cdot \text{MHz})$	Ref.
$6s19p^3P_0$	49 950.00(10)	49 949.916 956	2490	[S2]
$6s20p^3P_0$	50 008.89(10)	50 008.797 212	2782	[S2]
$6s21p^3P_0$	50 057.80(10)	50 057.639 704	4806	[S2]
$6s22p^3P_0$	50 098.66(10)	50 098.610 920	1471	[S2]
$6s23p^3P_0$	50 133.38(10)	50 133.325 703	1628	[S2]
$6s24p^3P_0$	50 163.01(10)	50 163.007 489	75	[S2]
$6s25p^3P_0$	50 188.69(10)	50 188.596 367	2807	[S2]
$6s26p^3P_0$	50 210.87(10)	50 210.823 496	1394	[S2]
$6s27p^3P_0$	50 230.30(10)	50 230.263 498	1094	[S2]
$6s28p^3P_0$	50 247.59(10)	50 247.372 132	6532	[S2]
$6s29p^3P_0$	50 262.63(10)	50 262.514 002	3478	[S2]
$6s30p^3P_0$	50 276.24(10)	50 275.983 317	7695	[S2]

G.  $^{171}\text{Yb S } F = 1/2$ Table S25: Laser spectroscopic data of the  $|\nu, L = 0, F = 1/2\rangle$  Rydberg series obtained from laser spectroscopy in an atomic beam setup as described in App. B of the main text.

$\nu_{F_c=1}$	$\tilde{\nu}_{\text{exp.}} \text{ (cm}^{-1}\text{)}$	$\tilde{\nu}_{\text{th.}} \text{ (cm}^{-1}\text{)}$	$E_{\text{exp.}} - E_{\text{th.}} \text{ (} \hbar \cdot \text{MHz)}$
26.722 072 4	50 289.539 00(10)	50 289.539 148	-4.31
27.532 673 7	50 298.454 85(10)	50 298.454 960	-3.24
27.720 640 6	50 300.411 47(10)	50 300.411 503	-0.92
28.528 458 0	50 308.384 57(10)	50 308.384 445	3.70
28.719 255 7	50 310.170 00(10)	50 310.170 033	-0.98
29.524 054 2	50 317.324 69(10)	50 317.324 673	0.50
29.717 908 2	50 318.961 81(10)	50 318.961 749	1.92
30.519 412 0	50 325.402 48(10)	50 325.402 483	-0.13
30.716 591 2	50 326.910 28(10)	50 326.910 209	2.17
31.514 494 8	50 332.725 04(10)	50 332.725 133	-2.75
31.715 299 7	50 334.119 94(10)	50 334.119 864	2.14
32.509 273 8	50 339.383 70(10)	50 339.383 773	-2.06
32.714 030 4	50 340.679 43(10)	50 340.679 492	-1.96
33.503 725 4	50 345.456 21(10)	50 345.456 242	-1.01
33.712 781 1	50 346.664 91(10)	50 346.664 934	-0.57
34.497 829 0	50 351.009 28(10)	50 351.009 319	-1.17
34.711 550 2	50 352.141 20(10)	50 352.141 286	-2.70
35.491 566 2	50 356.100 60(10)	50 356.100 551	1.34
35.710 337 2	50 357.164 62(10)	50 357.164 684	-1.77
36.484 919 9	50 360.779 73(10)	50 360.779 737	-0.14
36.709 141 5	50 361.783 67(10)	50 361.783 731	-1.92
37.477 873 9	50 365.090 20(10)	50 365.090 148	1.48
37.707 963 3	50 366.040 69(10)	50 366.040 686	0.17
38.470 412 8	50 369.069 63(10)	50 369.069 523	3.22
38.706 802 7	50 369.972 30(10)	50 369.972 430	-3.93
39.462 522 0	50 372.750 98(10)	50 372.750 899	2.47
39.705 659 8	50 373.611 19(10)	50 373.611 261	-2.16
40.454 187 1	50 376.163 30(10)	50 376.163 291	0.23
40.704 535 0	50 376.985 57(10)	50 376.985 570	0.10
41.445 394 6	50 379.332 38(10)	50 379.332 272	3.36
41.703 428 3	50 380.120 43(10)	50 380.120 387	1.37
42.436 131 0	50 382.280 51(10)	50 382.280 447	1.89
42.702 339 7	50 383.037 80(10)	50 383.037 848	-1.43
43.426 383 7	50 385.027 95(10)	50 385.027 858	2.87
43.701 269 2	50 385.757 62(10)	50 385.757 594	0.76
44.416 140 2	50 387.592 29(10)	50 387.592 326	-1.12
44.700 216 3	50 388.297 13(10)	50 388.297 090	1.27
45.405 388 5	50 389.989 73(10)	50 389.989 735	-0.05
45.699 180 6	50 390.672 04(10)	50 390.671 919	3.48
46.394 117 2	50 392.234 27(10)	50 392.234 288	-0.45
46.698 161 3	50 392.895 97(10)	50 392.896 013	-1.18
47.382 315 0	50 394.338 76(10)	50 394.338 707	1.67
47.697 157 4	50 394.981 85(10)	50 394.981 861	-0.32
48.369 971 1	50 396.314 42(10)	50 396.314 419	-0.09
48.696 167 8	50 396.940 68(10)	50 396.940 685	-0.28
49.357 075 1	50 398.171 66(10)	50 398.171 710	-1.60
49.695 190 8	50 398.782 48(10)	50 398.782 589	-3.29
50.343 617 0	50 399.919 75(10)	50 399.919 862	-3.25
50.694 224 9	50 400.516 61(10)	50 400.516 695	-2.46
51.329 587 0	50 401.567 26(10)	50 401.567 261	-0.13
51.693 267 9	50 402.151 23(10)	50 402.151 248	-0.53
52.692 317 5	50 403.693 68(10)	50 403.693 722	-1.35
53.691 371 2	50 405.150 97(10)	50 405.150 902	1.89
57.232 905 3	50 409.716 13(10)	50 409.716 214	-2.40
58.214 635 5	50 410.836 48(10)	50 410.836 615	-4.10

Table S25 (continued)

$\nu_{F_c=1}$	$\tilde{\nu}_{\text{exp.}} \text{ (cm}^{-1}\text{)}$	$\tilde{\nu}_{\text{th.}} \text{ (cm}^{-1}\text{)}$	$E_{\text{exp.}} - E_{\text{th.}}$ ( $h \cdot \text{MHz}$ )
58.686 577 2	50 411.355 26(10)	50 411.355 318	-1.61
59.195 732 5	50 411.900 92(10)	50 411.901 068	-4.57
59.685 573 4	50 412.412 94(10)	50 412.412 988	-1.35
60.176 191 8	50 412.913 07(10)	50 412.913 240	-5.14
60.684 539 9	50 413.418 74(10)	50 413.418 825	-2.49
61.156 009 8	50 413.876 37(10)	50 413.876 507	-4.06
61.683 468 0	50 414.376 06(10)	50 414.376 154	-2.80
62.135 184 7	50 414.793 79(10)	50 414.793 977	-5.52
62.682 346 9	50 415.288 01(10)	50 415.288 036	-0.84
63.113 716 5	50 415.668 30(10)	50 415.668 516	-6.33
63.681 163 4	50 416.157 22(10)	50 416.157 293	-2.29
64.091 608 0	50 416.502 64(10)	50 416.502 771	-4.08
64.679 901 1	50 416.986 54(10)	50 416.986 526	0.41
65.068 865 1	50 417.299 09(10)	50 417.299 192	-2.98
65.678 538 9	50 417.778 03(10)	50 417.778 142	-3.33
66.045 498 3	50 418.059 89(10)	50 418.060 047	-4.73
66.677 049 5	50 418.534 22(10)	50 418.534 362	-4.24
67.021 524 8	50 418.787 35(10)	50 418.787 441	-2.87
67.675 396 4	50 419.257 30(10)	50 419.257 241	1.69
67.996 970 2	50 419.483 46(10)	50 419.483 333	3.84
68.673 530 9	50 419.948 65(10)	50 419.948 679	-1.01
68.971 873 5	50 420.149 51(10)	50 420.149 546	-0.93
69.671 385 0	50 420.610 50(10)	50 420.610 432	2.16
69.946 291 9	50 420.787 74(10)	50 420.787 786	-1.28
70.668 862 8	50 421.244 15(10)	50 421.244 117	1.06
70.920 311 3	50 421.399 65(10)	50 421.399 654	-0.13
71.665 825 2	50 421.851 10(10)	50 421.851 219	-3.51
71.894 060 6	50 421.986 72(10)	50 421.986 663	1.59
72.662 066 6	50 422.432 96(10)	50 422.433 092	-3.92
72.867 735 2	50 422.550 30(10)	50 422.550 254	1.35
73.657 277 9	50 422.990 90(10)	50 422.990 949	-1.57
73.841 634 0	50 423.091 79(10)	50 423.091 820	-0.80
74.650 995 6	50 423.525 84(10)	50 423.525 857	-0.39
74.816 210 4	50 423.612 77(10)	50 423.612 730	1.12
75.642 548 8	50 424.038 67(10)	50 424.038 725	-1.80
75.792 125 2	50 424.114 33(10)	50 424.114 350	-0.55
76.631 062 4	50 424.530 34(10)	50 424.530 333	0.19
76.770 243 3	50 424.598 07(10)	50 424.598 029	1.30
77.615 632 4	50 425.001 37(10)	50 425.001 426	-1.74
77.751 458 8	50 425.065 04(10)	50 425.065 015	0.81
78.595 708 9	50 425.452 78(10)	50 425.452 897	-3.49
78.736 311 3	50 425.516 38(10)	50 425.516 286	2.75
79.724 690 7	50 425.952 51(10)	50 425.952 463	1.38
80.715 971 8	50 426.373 93(10)	50 426.373 926	0.04
81.512 172 4	50 426.701 20(10)	50 426.701 371	-5.01
81.709 393 3	50 426.781 11(10)	50 426.781 004	3.15
82.478 656 0	50 427.086 06(10)	50 427.086 174	-3.52
82.704 310 0	50 427.174 17(10)	50 427.174 081	2.70
83.443 205 7	50 427.456 82(10)	50 427.456 954	-4.02
83.700 251 6	50 427.553 68(10)	50 427.553 608	2.08
84.406 134 7	50 427.814 45(10)	50 427.814 504	-1.70
84.696 894 3	50 427.920 22(10)	50 427.920 078	4.38
85.367 654 0	50 428.159 50(10)	50 428.159 526	-0.90
85.694 015 0	50 428.274 04(10)	50 428.274 003	1.08
86.327 908 4	50 428.492 54(10)	50 428.492 653	-3.28
86.691 456 4	50 428.615 83(10)	50 428.615 894	-1.85
87.287 001 4	50 428.814 50(10)	50 428.814 463	1.21
87.689 101 3	50 428.946 27(10)	50 428.946 250	0.61
88.245 011 2	50 429.125 51(10)	50 429.125 491	0.62

Table S25 (*continued*)

$\nu_{F_c=1}$	$\tilde{\nu}_{\text{exp.}} \text{ (cm}^{-1}\text{)}$	$\tilde{\nu}_{\text{th.}} \text{ (cm}^{-1}\text{)}$	$E_{\text{exp.}} - E_{\text{th.}}$ ( $h \cdot \text{MHz}$ )
88.686 855 4	50 429.265 48(10)	50 429.265 556	-2.12
89.202 003 3	50 429.426 33(10)	50 429.426 237	2.86
89.684 634 7	50 429.574 30(10)	50 429.574 271	0.82
90.158 039 1	50 429.717 11(10)	50 429.717 171	-1.92
90.682 353 3	50 429.872 68(10)	50 429.872 834	-4.58
91.113 185 8	50 429.998 69(10)	50 429.998 737	-1.36
91.679 911 4	50 430.161 68(10)	50 430.161 658	0.61
92.067 527 4	50 430.271 35(10)	50 430.271 360	-0.27
92.677 176 2	50 430.441 20(10)	50 430.441 124	2.23
93.021 182 8	50 430.535 48(10)	50 430.535 447	0.99
93.673 950 4	50 430.711 57(10)	50 430.711 581	-0.37
93.974 336 4	50 430.791 46(10)	50 430.791 403	1.73
94.669 911 9	50 430.973 36(10)	50 430.973 330	0.88
94.927 298 5	50 431.039 65(10)	50 431.039 638	0.43
95.664 490 5	50 431.226 62(10)	50 431.226 600	0.54
95.880 627 8	50 431.280 49(10)	50 431.280 600	-3.43
96.656 611 3	50 431.471 53(10)	50 431.471 495	1.17
96.835 388 2	50 431.514 90(10)	50 431.514 826	2.15
97.644 233 1	50 431.707 95(10)	50 431.707 903	1.44
97.793 610 3	50 431.743 09(10)	50 431.743 037	1.44
98.624 046 8	50 431.935 51(10)	50 431.935 459	1.49
98.758 592 1	50 431.966 23(10)	50 431.966 178	1.44
99.733 293 0	50 432.185 08(10)	50 432.185 023	1.73
100.717 156 5	50 432.399 53(10)	50 432.399 514	0.38
101.707 046 1	50 432.609 14(10)	50 432.609 066	2.25
102.700 291 2	50 432.813 37(10)	50 432.813 269	3.02
103.695 357 4	50 433.011 96(10)	50 433.011 989	-0.78
104.337 310 1	50 433.137 10(10)	50 433.137 185	-2.66
104.691 419 8	50 433.205 37(10)	50 433.205 261	3.27
105.277 816 2	50 433.316 52(10)	50 433.316 487	1.11
105.688 004 5	50 433.393 24(10)	50 433.393 192	1.36
106.216 927 0	50 433.490 80(10)	50 433.490 791	0.20
106.684 795 5	50 433.576 10(10)	50 433.575 917	5.38
107.154 853 1	50 433.660 34(10)	50 433.660 321	0.51
107.681 527 8	50 433.753 58(10)	50 433.753 582	-0.16
108.091 797 1	50 433.825 37(10)	50 433.825 287	2.56
108.677 903 5	50 433.926 30(10)	50 433.926 319	-0.61
109.028 016 8	50 433.985 91(10)	50 433.985 896	0.54
109.673 478 8	50 434.094 32(10)	50 434.094 237	2.54
109.963 927 9	50 434.142 36(10)	50 434.142 368	-0.20
110.667 430 8	50 434.257 45(10)	50 434.257 381	2.01
110.900 332 1	50 434.294 94(10)	50 434.294 976	-1.15
111.657 970 6	50 434.415 69(10)	50 434.415 650	1.23
111.839 000 4	50 434.444 20(10)	50 434.444 121	2.38
112.640 970 0	50 434.568 69(10)	50 434.568 604	2.68
112.784 045 2	50 434.590 68(10)	50 434.590 534	4.35
113.742 734 5	50 434.735 45(10)	50 434.735 347	2.96
114.718 444 8	50 434.879 13(10)	50 434.879 019	3.38
115.705 371 9	50 435.020 73(10)	50 435.020 661	1.97
116.697 553 3	50 435.159 51(10)	50 435.159 450	1.88
117.355 112 0	50 435.249 50(10)	50 435.249 498	0.01
117.692 094 7	50 435.295 12(10)	50 435.295 061	1.75
118.280 186 1	50 435.373 73(10)	50 435.373 646	2.43
118.687 687 6	50 435.427 47(10)	50 435.427 416	1.56
119.203 551 7	50 435.494 70(10)	50 435.494 694	0.10
119.683 618 9	50 435.556 53(10)	50 435.556 524	0.28
120.125 636 5	50 435.612 85(10)	50 435.612 800	1.59

Table S26: Predicted  $g_{\text{th}}$  and experimental  $g_{\text{exp}}$  factors of  $|\nu, L = 0, F = 1/2\rangle$  Rydberg states obtained from laser spectroscopy in an atomic beam setup as described in App. B of the main text.

$\nu_{F_c=1}$	$g_{\text{exp}}$	$g_{\text{th}}$
30.519 412 0	2.70(16)	2.63
30.716 591 2	0.03(2)	0.04
35.710 337 2	0.06(2)	0.07
40.454 187 1	2.54(14)	2.54
40.704 535 0	0.13(2)	0.13
50.343 617 0	2.44(13)	2.42
50.694 224 9	0.25(5)	0.25
60.176 191 8	2.42(13)	2.29
60.684 539 9	0.38(4)	0.38
69.946 291 9	2.21(12)	2.15
70.668 862 8	0.54(3)	0.53
70.920 311 3	2.13(12)	2.13
71.665 825 2	0.57(4)	0.57
71.894 060 6	2.15(12)	2.10
72.662 066 6	0.57(4)	0.61
72.867 735 2	2.07(11)	2.05
73.657 277 9	0.66(4)	0.67
73.841 634 0	2.01(11)	1.99
74.650 995 6	0.78(4)	0.76
74.816 210 4	1.95(11)	1.91
75.642 548 8	0.89(5)	0.88
75.792 125 2	1.98(10)	1.78
76.631 062 4	1.09(6)	1.04
76.770 243 3	1.63(9)	1.62
77.751 458 8	1.46(8)	1.42
78.736 311 3	1.34(7)	1.22
79.724 690 7	1.05(6)	1.04
80.715 971 8	0.90(5)	0.91
81.709 393 3	0.82(5)	0.81
82.704 310 0	0.75(4)	0.75
83.700 251 6	0.71(4)	0.71
84.696 894 3	0.74(4)	0.67
85.367 654 0	2.19(18)	2.01
85.694 015 0	0.71(4)	0.65
86.691 456 4	0.54(4)	0.64
87.689 101 3	0.66(4)	0.63
88.245 011 2	2.04(12)	2.04
88.686 855 4	0.64(4)	0.63
89.202 003 3	2.02(14)	2.05
89.684 634 7	0.66(4)	0.62
90.158 039 1	2.03(14)	2.05
90.682 353 3	0.65(3)	0.63
91.679 911 4	0.66(4)	0.63
92.067 527 4	1.87(12)	2.04
92.677 176 2	0.65(4)	0.64
93.021 182 8	2.03(11)	2.03
93.673 950 4	0.69(5)	0.65
93.974 336 4	2.07(11)	2.01
94.669 911 9	0.65(5)	0.68
94.927 298 5	1.97(11)	1.99
95.664 490 5	0.76(4)	0.73
95.880 627 8	1.96(11)	1.94
96.656 611 3	0.79(5)	0.81
96.835 388 2	1.90(10)	1.86
97.644 233 1	0.96(6)	0.96
97.793 610 3	1.71(10)	1.70
98.624 046 8	1.40(10)	1.21
98.758 592 1	1.49(18)	1.45
99.733 293 0	1.17(6)	1.16

Table S26 (*continued*)

$\nu_{F_c=1}$	$g_{\text{exp}}$	$g_{\text{th}}$
100.717 156 5	0.98(5)	0.95
101.707 046 1	0.84(5)	0.82
102.700 291 2	0.74(4)	0.75
103.695 357 4	0.72(4)	0.71
104.691 419 8	0.66(3)	0.69
106.684 795 5	0.76(4)	0.67
107.681 527 8	0.67(3)	0.67
108.677 903 5	0.67(3)	0.68
109.673 478 8	0.70(4)	0.70
110.667 430 8	0.79(5)	0.74

Table S27: Predicted  $\alpha_{0,\text{th}}$  and experimental  $\alpha_{0,\text{exp}}$  static dipole polarizabilities of  $|\nu, L = 0, F = 1/2\rangle$  Rydberg states obtained from laser spectroscopy in an atomic beam setup as described in App. B of the main text.

$\nu_{F_c=1}$	$\alpha_{0,\text{exp}}$ (MHz/(V/cm) <sup>2</sup> )	$\alpha_{0,\text{th}}$ (MHz/(V/cm) <sup>2</sup> )
27.532 673 7	18.1(14)	16.8
28.528 458 0	37.1(9)	37.1
29.524 054 2	161.5(11)	167.9
30.519 412 0	-128.2(11)	-135.1
31.514 494 8	25.6(14)	-63.5
31.715 299 7	-63.4(11)	31.8
32.509 273 8	-49.1(9)	-48.0
32.714 030 4	43.6(19)	42.4
33.503 725 4	-40.9(9)	-42.0
33.712 781 1	58.5(12)	60.7
34.497 829 0	-38.9(10)	-39.3
34.711 550 2	-45.7(12)	-47.2
35.491 566 2	-37.6(8)	-37.9
35.710 337 2	116.6(16)	119.5
36.709 141 5	-274(7)	-288.2
37.707 963 3	3.2(9)	3.4
38.706 802 7	44.0(16)	44.9
39.705 659 8	71.0(9)	72.4
40.704 535 0	97.1(17)	98.1
41.703 428 3	122.5(15)	125.1
42.702 339 7	155(2)	155.0
43.701 269 2	186.8(11)	188.8
44.700 216 3	225.8(13)	227.4
58.214 635 5	-989.6(14)	-1034.95
59.195 732 5	-1142(5)	-1336.64
60.176 191 8	-1683(4)	-1771.13
61.156 009 8	-2310(5)	-2460.77
62.135 184 7	-3476(5)	-3744.12
63.113 716 5	-7155(4)	-7061.66
65.068 865 1	1911(20)	1796.33
66.045 498 3	11 526(28)	12 066.91
67.021 524 8	5747(4)	6094.47
67.996 970 2	4481(5)	4616.27
68.673 530 9	-6104(410)	-5281.4
68.971 873 5	3832(3)	4015.77
69.671 385 0	-3192(88)	-2967.8
69.946 291 9	3286(3)	3802.89
70.668 862 8	-2174(32)	-2072.1
70.920 311 3	3662(4)	3842.52
71.665 825 2	-2016(30)	-1718.3
71.894 060 6	3880(3)	4101.32
72.662 066 6	-1762(26)	-1711.0

Table S28: Predicted  $\Delta E_{\text{Stark,th}}$  and experimental  $\Delta E_{\text{Stark,exp}}$  Stark shifts of  $|\nu, L = 0, F = 1/2\rangle$  Rydberg states obtained from laser spectroscopy in an atomic beam setup as described in App. B of the main text at static electric fields of 23.8 mV/cm (<sup>a</sup>) or 41.6 mV/cm (<sup>b</sup>).

$\nu_{F_c=1}$	$\Delta E_{\text{Stark,exp}}$ (MHz)	$\Delta E_{\text{Stark,th}}$ (MHz)
64.091 608 0	12.9(6) <sup>a</sup>	11.8 <sup>a</sup>
65.678 538 9	-4.7(6) <sup>b</sup>	-4.8 <sup>b</sup>
66.677 049 5	-5.0(6) <sup>b</sup>	-5.3 <sup>b</sup>
67.675 396 4	17.3(6) <sup>b</sup>	18.3 <sup>b</sup>

**H.**  $^{171}\text{Yb S } F = 3/2$ 

Table S29: Spectroscopic data of the  $|\nu, L = 0, F = 3/2\rangle$  Rydberg series obtained from microwave spectroscopy in an atomic beam setup as described in App. B of the main text between  $f = |\nu, L = 0, F = 3/2\rangle$  and  $i = |\nu', L = 0, F = 1/2\rangle$  (a) or  $^b i = |\nu', L = 2, F = 5/2\rangle$  (b) states.

$\nu_{F_c=1}^f$	$\nu_{F_c=1}^i$	$\nu_{f \leftarrow i}$ (MHz)	$\tilde{\nu}_{\text{exp.}}$ ( $\text{cm}^{-1}$ )	$\tilde{\nu}_{\text{th.}}$ ( $\text{cm}^{-1}$ )	$E_{\text{exp.}} - E_{\text{th.}}$ ( $h \cdot \text{MHz}$ )
42.561 535 7	41.703 428 3 <sup>a</sup>	75 510.49(10)	50 382.639 145	50 382.639 012	4.01
43.561 481 7	42.281 582 8 <sup>b</sup>	106 550.02(10)	50 385.388 283	50 385.388 228	1.66
44.561 433 9	43.281 525 6 <sup>b</sup>	99 434.19(10)	50 387.954 467	50 387.954 469	-0.06

I.  $^{171}\text{Yb P } F = 1/2$ Table S30: Spectroscopic data of the  $|\nu, L = 1, F = 1/2\rangle$  Rydberg series obtained from microwave spectroscopy in an atomic beam setup as described in App. B of the main text between  $i = |\nu, L = 0, F = 1/2\rangle$  and  $f = |\nu', L = 1, F = 1/2\rangle$ .

$\nu_{F_c=1}^f$	$\nu_{F_c=1}^i$	$\nu_{f \leftarrow i}$ (MHz)	$\tilde{\nu}_{\text{exp.}}$ ( $\text{cm}^{-1}$ )	$\tilde{\nu}_{\text{th.}}$ ( $\text{cm}^{-1}$ )	$E_{\text{exp.}} - E_{\text{th.}}$ ( $h \cdot \text{MHz}$ )
28.056 052 3	27.720 640 6	101 759.03(10)	50 303.805 819	50 303.805 600	6.57
29.529 559 7	29.717 908 2	-47 673.09(10)	50 317.371 545	50 317.371 612	-2.00
29.827 861 8	29.717 908 2	27 406.71(10)	50 319.875 938	50 319.876 141	-6.09
30.511 356 6	30.716 591 2	-47 064.40(10)	50 325.340 310	50 325.340 265	1.34
31.052 583 6	30.716 591 2	75 043.07(10)	50 329.413 376	50 329.413 508	-3.94
32.051 433 2	31.715 299 7	68 236.65(10)	50 336.395 994	50 336.396 148	-4.61
33.050 259 4	32.714 030 4	62 222.71(10)	50 342.755 019	50 342.755 172	-4.61
33.735 950 3	34.711 550 2	-160 206.00(10)	50 346.797 389	50 346.797 509	-3.57
34.049 047 5	33.712 781 1	56 886.78(10)	50 348.562 472	50 348.562 611	-4.16
34.709 370 4	35.710 337 2	-150 943.26(10)	50 352.129 759	50 352.129 847	-2.63
35.047 781 9	34.711 550 2	52 133.44(10)	50 353.880 271	50 353.880 388	-3.49
35.438 636 3	35.710 337 2	-39 707.34(10)	50 355.840 189	50 355.840 127	1.88
35.438 636 3	34.711 550 2	110 889.87(10)	50 355.840 175	50 355.840 127	1.43
35.681 585 5	34.711 550 2	146 435.93(10)	50 357.025 863	50 357.025 948	-2.54
37.045 023 7	36.709 141 5	44 067.61(10)	50 363.253 668	50 363.253 734	-1.98
37.623 572 0	36.709 141 5	117 229.07(10)	50 365.694 072	50 365.694 076	-0.13
38.043 493 1	37.707 963 3	40 630.85(10)	50 367.395 986	50 367.396 026	-1.20
38.594 182 7	37.707 963 3	105 037.84(10)	50 369.544 372	50 369.544 339	0.97
39.041 831 5	38.706 802 7	37 523.91(10)	50 371.224 092	50 371.224 108	-0.48
39.565 259 0	38.706 802 7	94 255.01(10)	50 373.116 438	50 373.116 377	1.84
40.040 011 7	39.705 659 8	34 705.14(10)	50 374.768 900	50 374.768 894	0.20
40.378 690 0	39.705 659 8	68 981.76(10)	50 375.912 245	50 375.912 310	-1.94
40.537 438 5	39.705 659 8	84 758.71(10)	50 376.438 508	50 376.438 425	2.47
41.038 001 3	40.704 535 0	32 138.58(10)	50 378.057 598	50 378.057 571	0.81
41.511 391 5	40.704 535 0	76 440.13(10)	50 379.535 339	50 379.535 247	2.76
42.035 761 4	41.703 428 3	29 793.00(10)	50 381.114 174	50 381.114 129	1.34
42.487 743 7	41.703 428 3	69 195.41(10)	50 382.428 497	50 382.428 406	2.73
43.033 244 4	42.702 339 7	27 641.05(10)	50 383.959 855	50 383.959 794	1.80
43.334 757 2	42.702 339 7	52 272.09(10)	50 384.781 458	50 384.781 527	-2.08
44.030 392 4	43.701 269 2	25 658.58(10)	50 386.613 472	50 386.613 398	2.20
44.317 229 6	43.701 269 2	47 549.92(10)	50 387.343 688	50 387.343 751	-1.89
44.449 199 9	43.701 269 2	57 485.49(10)	50 387.675 103	50 387.675 039	1.93
45.027 134 5	44.700 216 3	23 824.08(10)	50 389.091 776	50 389.091 691	2.54
45.298 499 5	44.700 216 3	43 202.96(10)	50 389.738 186	50 389.738 240	-1.63
45.434 324 8	44.700 216 3	52 777.45(10)	50 390.057 557	50 390.057 513	1.30
46.279 037 6	45.699 180 6	39 226.39(10)	50 391.980 371	50 391.980 418	-1.42
46.421 944 3	45.699 180 6	48 671.25(10)	50 392.295 418	50 392.295 392	0.76
47.019 035 5	45.699 180 6	87 199.79(10)	50 393.580 591	50 393.580 492	2.98
47.259 370 7	46.698 161 3	35 615.51(10)	50 394.084 019	50 394.084 061	-1.28
47.411 588 9	46.698 161 3	45 060.07(10)	50 394.399 055	50 394.399 048	0.23
48.013 963 9	46.698 161 3	81 555.28(10)	50 395.616 405	50 395.616 299	3.16
48.239 981 0	47.697 157 4	32 359.65(10)	50 396.061 263	50 396.061 303	-1.19
48.402 820 3	47.697 157 4	41 856.84(10)	50 396.378 055	50 396.378 060	-0.14
49.008 023 9	47.697 157 4	76 327.23(10)	50 397.527 864	50 397.527 764	2.99
49.221 267 6	48.696 167 8	29 441.79(10)	50 397.922 757	50 397.922 794	-1.10
49.395 280 6	48.696 167 8	38 993.03(10)	50 398.241 352	50 398.241 366	-0.41
50.001 054 9	51.693 267 9	-84 739.02(10)	50 399.324 659	50 399.324 557	3.05
50.203 548 1	51.693 267 9	-74 149.39(10)	50 399.677 890	50 399.677 922	-0.95
50.992 891 0	52.692 317 5	-80 290.56(10)	50 401.015 517	50 401.015 428	2.68
51.187 069 6	52.692 317 5	-70 713.28(10)	50 401.334 981	50 401.335 009	-0.82
51.382 863 8	50.694 224 9	34 082.43(10)	50 401.653 562	50 401.653 587	-0.74
52.172 014 6	50.694 224 9	71 492.88(10)	50 402.901 440	50 402.901 463	-0.69
52.377 632 4	50.694 224 9	80 963.58(10)	50 403.217 349	50 403.217 378	-0.85
53.372 889 7	51.693 267 9	76 266.52(10)	50 404.695 225	50 404.695 252	-0.82

Table S30 (*continued*)

$\nu_{F_c=1}^f$	$\nu_{F_c=1}^i$	$\nu_{f \leftarrow i}$ (MHz)	$\tilde{\nu}_{\text{exp.}}$ ( $\text{cm}^{-1}$ )	$\tilde{\nu}_{\text{th.}}$ ( $\text{cm}^{-1}$ )	$E_{\text{exp.}} - E_{\text{th.}}$ ( $h \cdot \text{MHz}$ )
54.945 818 2	53.691 371 2	51 515.52(10)	50 406.869 275	50 406.869 228	1.41
55.136 155 3	53.691 371 2	59 024.72(10)	50 407.119 755	50 407.119 753	0.07
57.119 511 7	59.685 573 4	-84 837.58(10)	50 409.583 110	50 409.583 068	1.27
59.855 510 8	58.686 577 2	36 944.08(10)	50 412.587 640	50 412.587 655	-0.46
60.102 495 0	58.686 577 2	44 478.23(10)	50 412.838 952	50 412.838 877	2.24
60.348 111 9	58.686 577 2	51 874.16(10)	50 413.085 654	50 413.085 656	-0.07
60.834 245 5	59.685 573 4	34 544.86(10)	50 413.565 280	50 413.565 306	-0.78
61.098 304 3	59.685 573 4	42 215.38(10)	50 413.821 141	50 413.821 058	2.50
61.345 331 1	59.685 573 4	49 296.06(10)	50 414.057 327	50 414.057 330	-0.07
62.094 639 0	60.684 539 9	40 115.56(10)	50 414.756 936	50 414.756 846	2.69
62.789 243 7	61.683 468 0	30 184.97(10)	50 415.383 016	50 415.383 053	-1.12
63.091 400 0	61.683 468 0	38 162.58(10)	50 415.649 121	50 415.649 023	2.91
63.340 104 3	61.683 468 0	44 637.60(10)	50 415.865 104	50 415.865 093	0.33
63.765 619 5	61.683 468 0	55 543.54(10)	50 416.228 887	50 416.228 926	-1.17
64.088 505 3	62.682 346 9	36 342.27(10)	50 416.500 284	50 416.500 185	2.97
64.337 622 7	62.682 346 9	42 530.52(10)	50 416.706 702	50 416.706 685	0.51
64.741 301 3	62.682 346 9	52 409.07(10)	50 417.036 215	50 417.036 257	-1.28
65.085 887 3	63.681 163 4	34 642.93(10)	50 417.312 856	50 417.312 748	3.26
65.335 205 5	63.681 163 4	40 556.15(10)	50 417.510 100	50 417.510 075	0.76
65.716 320 5	63.681 163 4	49 467.22(10)	50 417.807 341	50 417.807 385	-1.30
66.083 489 4	62.682 346 9	83 973.07(10)	50 418.089 076	50 418.088 965	3.35
66.332 833 7	64.679 901 2	38 704.12(10)	50 418.277 557	50 418.277 525	0.95
66.690 703 7	64.679 901 2	46 704.54(10)	50 418.544 422	50 418.544 468	-1.39
67.081 263 7	64.679 901 2	55 297.41(10)	50 418.831 050	50 418.830 934	3.46

Table S31: Laser spectroscopic data of the  $|\nu, L = 1, F = 1/2\rangle$  Rydberg series from three-photon laser spectroscopy as presented in Ref. [S14].

$\nu_{F_c=1}$	$\tilde{\nu}_{\text{exp.}} \text{ (cm}^{-1}\text{)}$	$\tilde{\nu}_{\text{th.}} \text{ (cm}^{-1}\text{)}$	$E_{\text{exp.}} - E_{\text{th.}}$ ( $h \cdot \text{MHz}$ )	Ref.
9.066 624 2	49 110.298 23	49 108.277 609	60 576.73	[S14]
9.134 455 3	49 127.330 09	49 128.030 119	-20 986.44	[S14]
10.039 358 5	49 352.401 17	49 354.435 282	-60 981.24	[S14]
10.062 152 7	49 360.613 96	49 359.362 629	37 513.80	[S14]
11.011 721 5	49 536.197 10	49 538.230 163	-60 949.58	[S14]
11.056 532 5	49 546.660 39	49 545.550 934	33 260.53	[S14]
11.966 344 3	49 677.500 27	49 676.862 568	19 117.72	[S14]
12.052 410 8	49 688.692 45	49 687.768 596	27 696.37	[S14]
12.944 454 1	49 786.334 58	49 788.301 705	-58 973.04	[S14]
13.047 981 5	49 799.208 40	49 798.653 153	16 646.02	[S14]
13.849 943 9	49 867.123 98	49 871.137 302	-120 316.47	[S14]
14.042 293 4	49 886.952 15	49 886.702 515	7483.96	[S14]
15.034 437 6	49 957.876 25	49 957.729 418	4402.05	[S14]
15.253 191 7	49 969.154 28	49 971.554 848	-71 967.27	[S14]
16.024 022 0	50 015.868 31	50 015.841 740	796.69	[S14]
16.137 827 0	50 021.328 71	50 021.848 249	-15 575.44	[S14]
17.011 982 4	50 063.991 63	50 064.039 526	-1435.89	[S14]
17.100 780 5	50 067.877 19	50 067.967 169	-2697.48	[S14]
17.999 661 4	50 104.481 11	50 104.510 414	-878.60	[S14]
18.085 071 5	50 107.684 46	50 107.702 076	-527.98	[S14]
18.987 594 3	50 138.822 72	50 138.839 634	-506.97	[S14]
19.076 794 6	50 141.678 94	50 141.679 433	-14.93	[S14]
19.975 730 4	50 168.198 20	50 168.208 050	-295.33	[S14]
20.071 683 1	50 170.834 10	50 170.831 130	88.99	[S14]
20.963 858 0	50 193.516 27	50 193.522 102	-174.69	[S14]
21.068 142 4	50 195.991 33	50 195.987 901	102.76	[S14]
23.926 159 2	50 251.523 38	50 251.524 177	-23.88	[S14]
24.061 546 0	50 253.676 99	50 253.675 305	50.41	[S14]
25.897 662 7	50 279.598 84	50 279.599 219	-11.34	[S14]
26.058 573 9	50 281.614 62	50 281.613 660	28.69	[S14]
30.807 108 4	50 327.592 29	50 327.592 671	-11.50	[S14]
31.052 583 6	50 329.413 65	50 329.413 508	4.13	[S14]
35.681 585 5	50 357.025 33	50 357.025 948	-18.56	[S14]
36.046 446 6	50 358.762 00	50 358.761 974	0.77	[S14]
36.652 863 1	50 361.533 18	50 361.533 465	-8.45	[S14]
37.045 023 7	50 363.253 81	50 363.253 734	2.33	[S14]
37.623 572 0	50 365.693 82	50 365.694 076	-7.70	[S14]
38.043 493 1	50 367.396 14	50 367.396 026	3.33	[S14]
38.594 182 6	50 369.544 25	50 369.544 339	-2.58	[S14]
39.041 831 5	50 371.223 89	50 371.224 108	-6.61	[S14]
39.565 259 0	50 373.116 32	50 373.116 377	-1.82	[S14]
40.040 011 7	50 374.768 94	50 374.768 894	1.25	[S14]
40.537 438 5	50 376.437 59	50 376.438 425	-25.12	[S14]
41.038 001 3	50 378.057 57	50 378.057 571	-0.12	[S14]
47.019 035 5	50 393.580 37	50 393.580 492	-3.72	[S14]
50.203 548 1	50 399.677 12	50 399.677 922	-23.99	[S14]
50.388 696 3	50 399.996 71	50 399.997 298	-17.74	[S14]
54.146 556 4	50 405.787 31	50 405.788 229	-27.65	[S14]
54.368 550 6	50 406.093 00	50 406.093 262	-7.86	[S14]
55.930 277 4	50 408.138 39	50 408.137 538	25.59	[S14]
56.127 190 1	50 408.382 22	50 408.383 250	-30.95	[S14]
56.360 834 5	50 408.671 04	50 408.671 463	-12.76	[S14]

Table S32: Predicted  $g_{\text{th}}$  and experimental  $g_{\text{exp}}$  factors of  $|\nu, L = 1, F = 1/2\rangle$  Rydberg states obtained from microwave spectroscopy in an atomic beam setup as described in App. B of the main text.

$\nu_{F_c=1}$	$g_{\text{exp}}$	$g_{\text{th}}$
28.056 052 3	1.418(20)	1.404
29.827 861 8	2.033(20)	1.971
31.052 583 6	1.414(20)	1.402
33.735 950 2	2.064(20)	2.014
34.709 370 4	2.088(20)	2.033
35.047 781 9	1.395(20)	1.396
35.438 636 3	-0.167(20)	-0.165
35.681 585 5	2.112(20)	2.057
37.623 572 0	2.100(20)	2.120
38.043 493 1	1.387(20)	1.389
40.378 690 0	-0.326(20)	-0.325
41.511 391 5	2.217(20)	2.245
42.035 761 4	1.396(20)	1.374
42.487 743 7	2.203(20)	2.232
45.027 134 5	1.353(20)	1.352
46.279 037 6	0.107(20)	0.103
46.421 944 3	1.865(20)	1.855

J.  $^{171}\text{Yb P } F = 3/2$ 

Table S33: Spectroscopic data of the  $|\nu, L = 1, F = 3/2\rangle$  Rydberg series obtained from microwave spectroscopy in an atomic beam setup as described in App. B of the main text between  $i = |\nu, L = 0, F = 1/2\rangle$  and  $f = |\nu', L = 1, F = 3/2\rangle$ .

$\nu_{F_c=1}^f$	$\nu_{F_c=1}^i$	$\nu_{f \leftarrow i}$ (MHz)	$\tilde{\nu}_{\text{exp.}}$ ( $\text{cm}^{-1}$ )	$\tilde{\nu}_{\text{th.}}$ ( $\text{cm}^{-1}$ )	$E_{\text{exp.}} - E_{\text{th.}}$ ( $h \cdot \text{MHz}$ )
28.030 790 8	27.720 640 6	94 221.66(10)	50 303.554 399	50 303.554 209	5.69
28.071 196 1	27.720 640 6	106 260.55(10)	50 303.955 973	50 303.955 979	-0.17
29.858 574 7	29.717 908 2	35 019.09(10)	50 320.129 860	50 320.129 752	3.24
30.840 620 4	30.716 591 2	27 991.62(10)	50 327.843 909	50 327.843 815	2.81
31.015 845 2	30.716 591 2	66 958.10(10)	50 329.143 691	50 329.143 745	-1.64
31.068 421 5	30.716 591 2	78 522.04(10)	50 329.529 422	50 329.529 507	-2.55
32.800 501 2	33.712 781 1	-163 250.19(10)	50 341.219 493	50 341.219 414	2.38
33.004 386 8	32.714 030 4	53 847.84(10)	50 342.475 663	50 342.475 714	-1.53
33.066 936 1	32.714 030 4	65 261.55(10)	50 342.856 383	50 342.856 479	-2.87
33.778 291 7	34.711 550 2	-152 958.42(10)	50 347.039 143	50 347.039 084	1.76
33.998 156 5	33.712 781 1	48 388.47(10)	50 348.278 999	50 348.279 026	-0.82
34.066 281 3	33.712 781 1	59 758.58(10)	50 348.658 265	50 348.658 357	-2.76
34.754 703 5	35.710 337 2	-143 820.20(10)	50 352.367 358	50 352.367 316	1.26
34.991 570 9	34.711 550 2	43 525.38(10)	50 353.593 137	50 353.593 132	0.16
35.065 677 3	34.711 550 2	54 867.19(10)	50 353.971 459	50 353.971 548	-2.68
35.729 857 4	34.711 550 2	153 415.52(10)	50 357.258 677	50 357.258 685	-0.22
35.984 614 2	35.710 337 2	39 178.15(10)	50 358.471 526	50 358.471 485	1.25
36.065 118 8	35.710 337 2	50 504.09(10)	50 358.849 319	50 358.849 403	-2.51
36.977 271 1	36.709 141 5	35 279.35(10)	50 362.960 524	50 362.960 434	2.68
37.064 601 4	36.709 141 5	46 599.12(10)	50 363.338 111	50 363.338 186	-2.27
37.677 235 1	36.709 141 5	123 844.31(10)	50 365.914 733	50 365.914 750	-0.51
37.969 526 4	37.707 963 3	31 771.80(10)	50 367.100 480	50 367.100 329	4.51
38.064 121 0	37.707 963 3	43 093.02(10)	50 367.478 115	50 367.478 183	-2.03
38.650 045 8	37.707 963 3	111 416.29(10)	50 369.757 134	50 369.757 154	-0.59
38.961 364 7	38.706 802 7	28 607.17(10)	50 370.926 662	50 370.926 426	7.08
39.063 674 1	38.706 802 7	39 935.50(10)	50 371.304 535	50 371.304 596	-1.86
39.622 740 9	38.706 802 7	100 345.82(10)	50 373.319 606	50 373.319 625	-0.58
39.952 771 2	39.705 659 8	25 744.76(10)	50 374.470 014	50 374.469 640	11.23
40.063 257 3	39.705 659 8	37 083.96(10)	50 374.848 249	50 374.848 301	-1.56
40.595 693 0	39.705 659 8	90 497.21(10)	50 376.629 923	50 376.629 942	-0.57
40.943 731 1	40.704 535 0	23 151.73(10)	50 377.757 829	50 377.757 173	19.67
41.062 868 0	40.704 535 0	34 501.65(10)	50 378.136 421	50 378.136 465	-1.32
41.569 255 7	40.704 535 0	81 748.21(10)	50 379.712 397	50 379.712 414	-0.51
42.062 503 6	41.703 428 3	32 157.17(10)	50 381.193 034	50 381.193 071	-1.12
42.543 737 5	41.703 428 3	73 986.21(10)	50 382.588 301	50 382.588 315	-0.43
43.062 161 9	42.702 339 7	30 023.54(10)	50 384.039 326	50 384.039 354	-0.84
44.061 840 8	43.701 269 2	28 077.18(10)	50 386.694 147	50 386.694 170	-0.67
44.902 822 5	43.701 269 2	90 943.91(10)	50 388.791 156	50 388.791 585	-12.88
45.061 538 7	44.700 216 3	26 297.88(10)	50 389.174 293	50 389.174 309	-0.48
45.474 795 9	44.700 216 3	55 611.41(10)	50 390.152 087	50 390.152 092	-0.15
45.891 341 6	44.700 216 3	84 351.63(10)	50 391.110 758	50 391.111 047	-8.66
46.061 253 9	45.699 180 6	24 667.90(10)	50 391.494 752	50 391.494 762	-0.29
46.454 707 7	45.699 180 6	50 822.88(10)	50 392.367 188	50 392.367 195	-0.21
46.879 334 1	45.699 180 6	78 308.34(10)	50 393.284 005	50 393.284 213	-6.24
47.060 985 0	45.699 180 6	89 848.41(10)	50 393.668 940	50 393.668 944	-0.13
47.436 095 9	46.698 161 3	46 571.54(10)	50 394.449 473	50 394.449 477	-0.12
47.866 788 5	46.698 161 3	72 758.62(10)	50 395.322 979	50 395.323 132	-4.56
48.060 730 6	46.698 161 3	84 328.11(10)	50 395.708 896	50 395.708 893	0.08
48.418 914 7	47.697 157 4	42 790.10(10)	50 396.409 185	50 396.409 193	-0.24
48.853 693 5	47.697 157 4	67 653.05(10)	50 397.238 524	50 397.238 637	-3.39
49.060 489 7	47.697 157 4	79 252.57(10)	50 397.625 442	50 397.625 434	0.26
49.403 092 8	48.696 167 8	39 419.62(10)	50 398.255 582	50 398.255 589	-0.22
50.060 261 0	51.693 267 9	-81 630.86(10)	50 399.428 335	50 399.428 319	0.48
50.388 543 4	48.696 167 8	91 626.72(10)	50 399.997 023	50 399.997 035	-0.37

Table S33 (*continued*)

$\nu_{F_c=1}^f$	$\nu_{F_c=1}^i$	$\nu_{f \leftarrow i}$ (MHz)	$\tilde{\nu}_{\text{exp.}}$ ( $\text{cm}^{-1}$ )	$\tilde{\nu}_{\text{th.}}$ ( $\text{cm}^{-1}$ )	$E_{\text{exp.}} - E_{\text{th.}}$ ( $h \cdot \text{MHz}$ )
50.825 813 5	52.692 317 5	-88 626.40(10)	50 400.737 464	50 400.737 514	-1.51
51.375 171 7	50.694 224 9	33 709.67(10)	50 401.641 128	50 401.641 139	-0.33
51.811 008 5	50.694 224 9	54 590.95(10)	50 402.337 653	50 402.337 682	-0.88
52.362 880 9	50.694 224 9	80 288.24(10)	50 403.194 822	50 403.194 837	-0.45
52.795 614 1	51.693 267 9	50 873.91(10)	50 403.848 219	50 403.848 231	-0.35
53.351 575 8	51.693 267 9	75 343.99(10)	50 404.664 453	50 404.664 467	-0.43
54.763 022 2	53.691 371 2	44 227.83(10)	50 406.626 184	50 406.626 166	0.54
55.331 564 6	53.691 371 2	66 654.24(10)	50 407.374 248	50 407.374 268	-0.60
57.058 932 7	59.685 573 4	-86 979.65(10)	50 409.511 659	50 409.511 612	1.42
59.670 657 2	58.686 577 2	31 248.46(10)	50 412.397 655	50 412.397 585	2.09
60.058 470 7	58.686 577 2	43 142.10(10)	50 412.794 384	50 412.794 325	1.77
60.293 135 8	58.686 577 2	50 225.78(10)	50 413.030 670	50 413.030 682	-0.36
60.650 266 1	59.685 573 4	29 146.52(10)	50 413.385 211	50 413.385 136	2.24
61.058 326 7	59.685 573 4	41 060.28(10)	50 413.782 611	50 413.782 551	1.80
61.286 930 7	59.685 573 4	47 629.02(10)	50 414.001 721	50 414.001 730	-0.26
62.607 532 3	61.683 468 0	25 337.93(10)	50 415.221 337	50 415.221 246	2.71
63.058 050 2	61.683 468 0	37 287.29(10)	50 415.619 924	50 415.619 855	2.07
63.275 581 5	61.683 468 0	42 963.77(10)	50 415.809 271	50 415.809 282	-0.31
63.585 188 8	61.683 468 0	50 949.20(10)	50 416.075 637	50 416.075 542	2.82
64.057 916 5	62.682 346 9	35 576.29(10)	50 416.474 734	50 416.474 663	2.12
64.270 342 9	62.682 346 9	40 864.94(10)	50 416.651 144	50 416.651 151	-0.22
64.562 198 4	62.682 346 9	48 052.49(10)	50 416.890 895	50 416.890 796	2.95
65.057 785 1	63.681 163 4	33 970.77(10)	50 417.290 436	50 417.290 363	2.17
65.265 331 0	63.681 163 4	38 904.19(10)	50 417.454 997	50 417.454 999	-0.08
65.538 569 9	63.681 163 4	45 333.94(10)	50 417.669 470	50 417.669 366	3.12
66.057 655 0	64.679 901 2	32 463.28(10)	50 418.069 385	50 418.069 306	2.37
66.260 494 0	64.679 901 2	37 069.78(10)	50 418.223 041	50 418.223 039	0.06
66.514 319 3	64.679 901 2	42 781.05(10)	50 418.413 549	50 418.413 438	3.32
67.057 525 6	64.679 901 2	54 778.70(10)	50 418.813 747	50 418.813 666	2.45

Table S34: Laser spectroscopic data of the  $|\nu, L = 1, F = 3/2\rangle$  Rydberg series from three-photon laser spectroscopy as presented in Ref. [S14].

$\nu_{F_c=1}$	$\tilde{\nu}_{\text{exp.}} \text{ (cm}^{-1}\text{)}$	$\tilde{\nu}_{\text{th.}} \text{ (cm}^{-1}\text{)}$	$E_{\text{exp.}} - E_{\text{th.}}$ ( $h \cdot \text{MHz}$ )	Ref.
9.066 137 6	49 110.142 99	49 108.134 316	60 218.56	[S14]
9.135 223 1	49 127.555 21	49 128.251 203	-20 865.36	[S14]
10.040 747 8	49 352.676 72	49 354.736 575	-61 752.79	[S14]
10.061 418 4	49 360.477 86	49 359.204 427	38 176.60	[S14]
11.013 442 2	49 536.466 59	49 538.512 920	-61 347.41	[S14]
11.055 668 2	49 546.527 43	49 545.410 580	33 482.26	[S14]
11.987 081 2	49 677.721 59	49 679.511 771	-53 668.37	[S14]
12.051 473 3	49 688.567 86	49 687.651 058	27 485.07	[S14]
12.947 132 9	49 786.580 68	49 788.572 685	-59 718.81	[S14]
13.047 047 6	49 799.109 60	49 798.560 870	16 450.60	[S14]
13.852 156 2	49 867.293 33	49 871.320 016	-120 717.09	[S14]
14.041 605 0	49 886.889 71	49 886.647 949	7247.81	[S14]
15.034 535 9	49 957.881 49	49 957.735 765	4368.76	[S14]
15.254 831 7	49 969.256 72	49 971.656 256	-71 936.40	[S14]
16.025 644 6	50 015.960 54	50 015.928 279	967.29	[S14]
16.138 929 2	50 021.381 51	50 021.905 803	-15 717.85	[S14]
17.015 534 3	50 064.155 98	50 064.197 814	-1254.26	[S14]
17.101 568 4	50 067.920 72	50 068.001 746	-2429.06	[S14]
18.005 101 0	50 104.689 62	50 104.715 041	-762.18	[S14]
18.079 861 5	50 107.497 53	50 107.508 678	-334.06	[S14]
18.994 793 2	50 139.055 45	50 139.070 306	-445.34	[S14]
19.071 319 8	50 141.504 01	50 141.506 282	-67.99	[S14]
19.984 635 2	50 168.444 30	50 168.453 073	-262.94	[S14]
20.065 010 4	50 170.651 91	50 170.649 934	59.12	[S14]
20.974 487 5	50 193.770 12	50 193.775 119	-149.97	[S14]
21.059 989 3	50 195.798 60	50 195.796 439	64.64	[S14]
23.942 445 3	50 251.783 99	50 251.784 876	-26.42	[S14]
24.047 600 6	50 253.456 40	50 253.455 407	29.81	[S14]
25.918 276 1	50 279.859 42	50 279.859 374	1.40	[S14]
26.039 520 5	50 281.377 62	50 281.377 078	16.24	[S14]
26.073 508 2	50 281.796 58	50 281.798 733	-64.65	[S14]
30.840 620 4	50 327.843 86	50 327.843 815	1.40	[S14]
31.015 845 2	50 329.143 73	50 329.143 745	-0.60	[S14]
31.068 421 5	50 329.526 29	50 329.529 507	-96.51	[S14]
35.729 857 4	50 357.258 56	50 357.258 685	-3.83	[S14]
35.984 614 2	50 358.471 57	50 358.471 485	2.43	[S14]
36.065 118 8	50 358.846 45	50 358.849 403	-88.45	[S14]
36.703 946 7	50 361.760 74	50 361.760 678	1.87	[S14]
36.977 271 1	50 362.960 44	50 362.960 434	0.25	[S14]
37.064 601 4	50 363.335 22	50 363.338 186	-89.05	[S14]
37.677 235 0	50 365.914 41	50 365.914 750	-10.32	[S14]
37.969 526 4	50 367.100 43	50 367.100 329	3.09	[S14]
38.064 121 0	50 367.474 66	50 367.478 183	-105.68	[S14]
38.650 045 8	50 369.756 83	50 369.757 154	-9.59	[S14]
38.961 364 7	50 370.926 55	50 370.926 426	3.68	[S14]
39.063 674 1	50 371.300 83	50 371.304 596	-113.04	[S14]
39.622 740 9	50 373.319 26	50 373.319 625	-11.05	[S14]
39.952 771 2	50 374.470 10	50 374.469 640	13.66	[S14]
40.063 257 3	50 374.845 04	50 374.848 301	-97.87	[S14]
40.595 693 0	50 376.629 52	50 376.629 942	-12.67	[S14]
40.943 731 1	50 377.757 23	50 377.757 173	1.60	[S14]
41.062 868 0	50 378.132 98	50 378.136 465	-104.37	[S14]
46.454 707 7	50 392.366 96	50 392.367 195	-7.17	[S14]
46.879 334 1	50 393.284 00	50 393.284 213	-6.48	[S14]
47.060 985 0	50 393.665 20	50 393.668 944	-112.13	[S14]
50.388 543 4	50 399.996 71	50 399.997 035	-9.88	[S14]
50.825 813 5	50 400.737 19	50 400.737 514	-9.86	[S14]
51.060 043 7	50 401.121 79	50 401.126 361	-136.99	[S14]

Table S34 (*continued*)

$\nu_{F_c=1}$	$\tilde{\nu}_{\text{exp.}} \text{ (cm}^{-1}\text{)}$	$\tilde{\nu}_{\text{th.}} \text{ (cm}^{-1}\text{)}$	$E_{\text{exp.}} - E_{\text{th.}}$ $(h \cdot \text{MHz})$	Ref.
54.341 165 5	50 406.055 61	50 406.055 836	-6.84	[S14]
55.745 807 9	50 407.905 10	50 407.904 986	3.32	[S14]
56.059 098 5	50 408.294 39	50 408.298 577	-125.58	[S14]
56.322 693 6	50 408.624 47	50 408.624 659	-5.61	[S14]

Table S35: Predicted  $g_{\text{th}}$  and experimental  $g_{\text{exp}}$  factors of  $|\nu, L = 1, F = 3/2\rangle$  Rydberg states obtained from microwave spectroscopy in an atomic beam setup as described in App. B of the main text.

$\nu_{F_c=1}$	$g_{\text{exp}}$	$g_{\text{th}}$
28.030 790 8	1.047(20)	1.037
28.071 196 1	1.477(20)	1.461
29.858 574 8	0.964(20)	0.954
30.840 620 4	0.967(20)	0.953
31.015 845 2	1.125(20)	1.116
31.068 421 5	1.393(20)	1.380
33.778 291 7	0.974(20)	0.951
34.754 703 5	0.980(20)	0.951
34.991 570 9	1.196(20)	1.197
35.065 677 3	1.295(20)	1.296
35.729 857 5	0.974(20)	0.951
37.677 235 0	0.981(20)	0.952
37.969 526 4	1.239(20)	1.240
38.064 121 0	1.252(20)	1.249
41.569 255 7	0.950(20)	0.958
42.062 503 6	1.219(20)	1.203
42.543 737 5	0.952(20)	0.961
45.891 341 6	1.304(20)	1.308
46.061 253 9	1.165(20)	1.169
46.454 707 7	0.989(20)	0.974
50.060 261 0	1.157(20)	1.143
52.362 880 9	1.021(20)	0.996
57.709 504 4	1.362(20)	1.338
58.058 773 2	1.122(20)	1.108
58.306 855 5	1.031(20)	1.016
58.690 401 7	1.414(20)	1.339
59.058 619 4	1.129(20)	1.105
59.299 759 8	1.044(20)	1.019
59.670 657 2	1.353(20)	1.339
60.058 470 8	1.108(20)	1.101
60.293 135 8	1.046(20)	1.022
60.650 266 1	1.361(20)	1.340
61.058 326 7	1.119(20)	1.098
61.286 930 7	1.050(20)	1.025
62.607 532 3	1.351(20)	1.340
63.058 050 2	1.104(20)	1.092
63.275 581 5	1.057(20)	1.031

**K. Hyperfine splitting of  $^{171}\text{Yb}$   $P F = 1/2$  and  $F = 3/2$  Rydberg states**

Table S36: Hyperfine splitting of  $^{171}\text{Yb}$   $P F = 1/2$  and  $F = 3/2$  Rydberg states referenced to the  $6s^2\ ^1S_0 \rightarrow 6snp\ ^1P_1$  transition of  $^{176}\text{Yb}$  (see Tab. S38). The data is reproduced from Tab. 3.3a or from Fig. 3.9 (marked by<sup>†</sup>) of Ref. [S14].

$n$	$\Delta E^{(171-176)} (h \cdot \text{MHz})$		
	$F = 3/2$	$F = 1/2$	$F = 1/2^\dagger$
13	4134	-2615	—
14	4779	-3482	—
15	4775	-3304	—
16	4625	-2010	—
17	4298	-3080	—
18	3478	-1599	—
19	2980	-91	—
20	2824	1241	—
21	3851	2546	—
22	-2236	3368	—
23	-1425	3819	—
24	-1401	4061	—
25	-1568	4210	—
28	-2245	4368	—
30	-2727	4378	9833
35	-3814	4278	7655
40	-4615	4092	6624
41	-4749	4046	6486
42	-4870	3995	6349
43	-4986	3928	6235
44	-5086	3873	6154
45	-5202	3802	6063
51	-5731	3154	5697
55	-6004	—	5526
60	-6258	736	5413

Table S37: Hyperfine splitting of  $^{171}\text{Yb}$   $P F = 1/2$  and  $F = 3/2$  Rydberg states referenced to the  $6s^2\ ^1S_0 \rightarrow 6snp\ ^3P_1$  transition of  $^{176}\text{Yb}$  (see Tab. S38). The data is reproduced from Tab. 3.3b or from Fig. 3.11 (marked by<sup>†</sup>) of Ref. [S14].

$n$	$\Delta\nu^{(171-176)} (h \cdot \text{MHz})$		
	$F = 3/2$	$F = 1/2$	$F = 3/2^\dagger$
13	470	5124	—
14	616	4696	—
15	603	4589	—
16	616	4351	—
17	968	3930	—
18	1271	3143	—
19	1924	1767	—
20	2795	30	—
21	3537	-1390	—
22	4002	-2249	—
23	4270	-2707	—
24	4415	-2963	—
25	4502	-3108	—
28	4573	-3240	—
30	4567	-3245	—
35	4474	-3068	—
40	4394	-2598	—
41	4391	-2431	—

Table S37 (*continued*)

$n$	$\Delta\nu^{(171-176)} (h \cdot \text{MHz})$		
	$F = 3/2$	$F = 1/2$	$F = 3/2^\dagger$
42	4373	-2240	—
43	4371	-2002	—
44	4370	-1714	—
45	4372	-1382	—
51	4451	—	—
55	4521	4521	-5060
59	4596	5717	-3447
61	4630	6026	-2633

Table S38: Experimental term values of  $6snp^{1,3}P_1$  Rydberg states of  $^{176}\text{Yb}$ . The data is reproduced from Tab. 3.1 of Ref. [S14].

$n$	$\tilde{\nu} (\text{cm}^{-1})$	
	$6snp^1P_1$	$6snp^3P_1$
13	49 127.37(14)	49 110.08(14)
14	49 352.47(14)	49 360.41(14)
15	49 536.26(14)	49 546.46(14)
16	49 677.52(14)	49 688.50(14)
17	49 786.39(14)	49 799.03(14)
18	49 867.13(14)	49 886.80(14)
19	49 969.11(14)	49 957.77(14)
20	50 021.24(14)	50 015.82(14)
21	50 067.62(14)	50 064.04(14)
22	50 107.54(14)	50 104.49(14)
23	50 141.58(14)	50 138.88(14)
24	50 170.61(14)	50 168.18(14)
25	50 195.82(14)	50 193.59(14)
26	50 217.67(14)	50 215.56(14)
27	50 236.75(14)	50 234.73(14)
28	50 253.50(14)	50 251.61(14)
29	50 268.31(14)	50 266.46(14)
30	50 281.42(14)	50 279.67(14)
31	50 293.13(14)	50 291.43(14)
32	50 303.63(14)	50 301.95(14)
33	50 313.03(14)	50 311.40(14)
34	50 321.54(14)	50 319.94(14)
35	50 329.23(14)	50 327.64(14)
36	50 336.23(14)	50 334.67(14)
37	50 342.56(14)	50 341.03(14)
38	50 348.37(14)	50 346.86(14)
39	50 353.70(14)	50 352.16(14)
40	50 358.56(14)	50 357.08(14)
41	50 363.10(14)	50 361.54(14)
42	50 367.23(14)	50 365.69(14)
43	50 371.05(14)	50 369.57(14)
44	50 374.65(14)	50 373.13(14)
45	50 377.88(14)	50 376.42(14)
46	50 380.94(14)	50 379.53(14)
47	50 383.79(14)	50 382.41(14)
48	50 386.47(14)	50 385.08(14)
49	50 388.94(14)	50 387.60(14)
50	50 391.28(14)	50 389.97(14)
51	50 393.44(14)	50 392.18(14)
52	50 395.50(14)	50 394.24(14)
53	50 397.38(14)	50 396.22(14)
54	50 399.21(14)	50 398.07(14)

Table S38 (*continued*)

$n$	$\tilde{\nu}$ (cm <sup>-1</sup> )	
	$6snp^1P_1$	$6snp^3P_1$
55	50 400.91(14)	50 399.83(14)
56	50 402.48(14)	50 401.42(14)
57	50 404.02(14)	50 402.99(14)
58	50 405.44(14)	50 404.46(14)
59	50 406.78(14)	50 405.85(14)
60	50 408.05(14)	50 407.14(14)
61	50 409.26(14)	50 408.41(14)
62	50 410.39(14)	50 409.57(14)
63	50 411.50(14)	50 410.73(14)
64	50 412.56(14)	50 411.79(14)
65	50 413.51(14)	50 412.79(14)
66	50 414.47(14)	50 413.77(14)
67	50 415.37(14)	50 414.70(14)
68	50 416.22(14)	50 415.58(14)
69	50 417.08(14)	50 416.43(14)
70	50 417.85(14)	50 417.26(14)
71	50 418.57(14)	50 418.03(14)
72	50 419.27(14)	50 418.75(14)
73	50 419.97(14)	50 419.48(14)
74	50 420.61(14)	50 420.12(14)
75	50 421.23(14)	50 420.74(14)
76	50 421.83(14)	50 421.39(14)
77	50 422.39(14)	—
78	50 422.96(14)	—
79	50 423.48(14)	—
80	50 424.02(14)	—
81	50 424.49(14)	—
82	50 424.98(14)	—
83	50 425.44(14)	—
84	50 425.86(14)	—
85	50 426.27(14)	—
86	50 426.71(14)	—
87	50 427.07(14)	—
88	50 427.46(14)	—
89	50 427.80(14)	—
90	50 428.16(14)	—
91	50 428.49(14)	—
92	50 428.85(14)	—
93	50 429.14(14)	—
94	50 429.45(14)	—
95	50 429.73(14)	—
96	50 430.04(14)	—
97	50 430.33(14)	—
98	50 430.61(14)	—
99	50 430.87(14)	—
100	50 431.10(14)	—
101	50 431.31(14)	—
102	50 431.60(14)	—
103	50 431.80(14)	—
104	50 432.01(14)	—
105	50 432.27(14)	—
111	50 433.41(14)	—
112	50 433.56(14)	—
113	50 433.77(14)	—
114	50 433.95(14)	—
115	50 434.10(14)	—
116	50 434.26(14)	—
118	50 434.54(14)	—

Table S38 (*continued*)

$n$	$\tilde{\nu}$ (cm <sup>-1</sup> )	
	$6snp^1P_1$	$6snp^3P_1$
121	50 434.98(14)	—

L.  $^{171}\text{Yb D } F = 3/2$ Table S39: Laser spectroscopic data of the  $|\nu, L = 2, F = 3/2\rangle$  Rydberg series obtained from laser spectroscopy in an atomic beam setup as described in App. B of the main text.

$\nu_{F_c=1}$	$\tilde{\nu}_{\text{exp.}} \text{ (cm}^{-1}\text{)}$	$\tilde{\nu}_{\text{th.}} \text{ (cm}^{-1}\text{)}$	$E_{\text{exp.}} - E_{\text{th.}}$ ( $h \cdot \text{MHz}$ )
30.197 934 9	50 322.880 83(10)	50 322.880 692	4.04
30.249 174 5	50 323.287 55(10)	50 323.288 028	-14.39
30.287 590 2	50 323.591 84(10)	50 323.592 064	-6.63
31.192 530 5	50 330.432 60(10)	50 330.432 392	6.20
31.249 137 0	50 330.840 46(10)	50 330.840 633	-5.03
31.287 372 1	50 331.114 97(10)	50 331.115 128	-4.72
32.186 771 4	50 337.292 67(10)	50 337.292 579	2.59
32.249 105 6	50 337.701 66(10)	50 337.701 667	-0.29
32.287 186 8	50 337.950 41(10)	50 337.950 422	-0.30
33.180 645 4	50 343.543 27(10)	50 343.543 170	3.04
33.249 079 1	50 343.953 06(10)	50 343.953 050	0.20
33.287 026 2	50 344.179 13(10)	50 344.179 243	-3.41
34.174 140 5	50 349.254 37(10)	50 349.254 303	2.01
34.249 056 7	50 349.665 13(10)	50 349.664 923	6.13
34.286 885 0	50 349.871 17(10)	50 349.871 240	-2.15
35.167 245 2	50 354.486 27(10)	50 354.486 314	-1.38
35.249 037 6	50 354.897 60(10)	50 354.897 622	-0.56
35.286 759 4	50 355.086 38(10)	50 355.086 350	1.00
36.159 948 0	50 359.291 46(10)	50 359.291 332	3.84
36.249 021 4	50 359.703 48(10)	50 359.703 282	6.01
36.286 646 7	50 359.876 52(10)	50 359.876 383	4.17
37.152 237 5	50 363.714 59(10)	50 363.714 586	-0.02
37.249 007 5	50 364.127 38(10)	50 364.127 134	7.37
37.286 544 8	50 364.286 31(10)	50 364.286 299	0.31
38.144 102 4	50 367.795 59(10)	50 367.795 474	3.49
38.248 995 7	50 368.208 68(10)	50 368.208 578	3.04
39.135 531 7	50 371.568 53(10)	50 371.568 436	2.95
39.248 985 5	50 371.982 19(10)	50 371.982 057	4.03
39.286 367 6	50 372.117 55(10)	50 372.117 558	-0.14
40.126 514 2	50 375.063 67(10)	50 375.063 691	-0.71
40.248 976 7	50 375.478 08(10)	50 375.477 793	8.74
41.117 038 9	50 378.307 78(10)	50 378.307 839	-1.86
41.286 218 5	50 378.838 68(10)	50 378.838 713	-0.87
42.107 094 8	50 381.324 30(10)	50 381.324 369	-2.11
42.286 152 5	50 381.847 48(10)	50 381.847 423	1.55
43.096 670 9	50 384.134 05(10)	50 384.134 088	-1.20
43.286 091 4	50 384.650 08(10)	50 384.650 056	0.60
44.085 756 5	50 386.755 44(10)	50 386.755 479	-1.31
44.286 034 5	50 387.265 05(10)	50 387.265 009	1.34
45.074 340 5	50 389.204 89(10)	50 389.205 003	-3.36
45.285 981 5	50 389.708 69(10)	50 389.708 671	0.58
45.285 981 5	50 389.708 69(10)	50 389.708 671	0.67
46.062 412 2	50 391.497 22(10)	50 391.497 363	-4.32
46.285 932 0	50 391.995 68(10)	50 391.995 681	-0.09
47.049 960 8	50 393.645 59(10)	50 393.645 722	-3.95
47.285 885 6	50 394.139 16(10)	50 394.139 148	0.36
48.036 975 5	50 395.661 77(10)	50 395.661 894	-3.79
48.285 842 0	50 396.150 90(10)	50 396.150 836	1.78
49.023 445 5	50 397.556 34(10)	50 397.556 505	-5.07
49.285 800 9	50 398.041 36(10)	50 398.041 331	0.79
50.285 762 2	50 399.820 17(10)	50 399.820 175	-0.04
50.994 708 8	50 401.018 30(10)	50 401.018 437	-4.13
51.285 725 5	50 401.496 01(10)	50 401.495 988	0.72
51.979 480 8	50 402.602 16(10)	50 402.602 246	-2.45
52.285 690 6	50 403.076 66(10)	50 403.076 577	2.56

Table S39 (continued)

$\nu_{F_c=1}$	$\tilde{\nu}_{\text{exp.}} \text{ (cm}^{-1}\text{)}$	$\tilde{\nu}_{\text{th.}} \text{ (cm}^{-1}\text{)}$	$E_{\text{exp.}} - E_{\text{th.}}$ $(h \cdot \text{MHz})$
52.963 665 6	50 404.097 48(10)	50 404.097 668	-5.78
53.285 657 4	50 404.569 00(10)	50 404.569 022	-0.52
53.947 252 5	50 405.511 00(10)	50 405.511 159	-4.66
54.285 625 7	50 405.979 77(10)	50 405.979 756	0.50
54.930 231 0	50 406.848 30(10)	50 406.848 597	-8.95
55.285 595 4	50 407.314 70(10)	50 407.314 637	1.76
55.912 590 7	50 408.115 18(10)	50 408.115 341	-4.67
56.285 566 2	50 408.579 03(10)	50 408.579 007	0.75
56.894 321 0	50 409.316 19(10)	50 409.316 288	-2.91
57.285 538 0	50 409.777 83(10)	50 409.777 746	2.47
57.875 411 5	50 410.455 78(10)	50 410.455 916	-4.08
58.285 510 6	50 410.915 39(10)	50 410.915 318	2.20
58.855 851 9	50 411.538 23(10)	50 411.538 331	-3.05
59.285 484 0	50 411.995 86(10)	50 411.995 815	1.24
59.835 631 8	50 412.567 36(10)	50 412.567 300	1.84
60.285 458 0	50 413.023 11(10)	50 413.022 992	3.38
60.814 740 9	50 413.546 22(10)	50 413.546 283	-1.95
61.285 432 4	50 414.000 32(10)	50 414.000 301	0.56
61.793 168 9	50 414.478 33(10)	50 414.478 467	-4.01
62.285 407 0	50 414.931 00(10)	50 414.930 918	2.46
62.770 905 7	50 415.366 84(10)	50 415.366 788	1.53
63.285 381 7	50 415.817 80(10)	50 415.817 770	0.95
63.747 941 1	50 416.213 86(10)	50 416.213 955	-2.73
64.285 356 2	50 416.663 54(10)	50 416.663 559	-0.41
64.724 265 1	50 417.022 31(10)	50 417.022 473	-4.98
65.285 330 3	50 417.470 86(10)	50 417.470 781	2.28
65.285 330 3	50 417.470 97(10)	50 417.470 781	5.69
65.699 867 8	50 417.794 43(10)	50 417.794 657	-6.87
66.285 303 6	50 418.241 77(10)	50 418.241 746	0.79
66.674 739 1	50 418.532 48(10)	50 418.532 652	-5.02
67.285 275 9	50 418.978 58(10)	50 418.978 592	-0.32
67.648 869 5	50 419.238 37(10)	50 419.238 447	-2.18
68.285 246 5	50 419.683 26(10)	50 419.683 304	-1.32
68.622 249 3	50 419.913 72(10)	50 419.913 889	-5.21
69.285 214 7	50 420.357 74(10)	50 420.357 723	0.59
69.594 869 2	50 420.560 58(10)	50 420.560 694	-3.45
70.285 179 5	50 421.003 61(10)	50 421.003 559	1.58
70.566 720 2	50 421.180 30(10)	50 421.180 459	-4.64
71.285 139 5	50 421.622 38(10)	50 421.622 404	-0.66
71.537 794 0	50 421.774 53(10)	50 421.774 672	-4.17
72.285 092 2	50 422.215 69(10)	50 422.215 741	-1.52
72.508 083 0	50 422.344 57(10)	50 422.344 720	-4.64
73.285 033 6	50 422.784 97(10)	50 422.784 950	0.49
73.477 581 5	50 422.891 79(10)	50 422.891 897	-3.29
74.284 956 6	50 423.331 28(10)	50 423.331 318	-1.01
74.446 287 1	50 423.417 25(10)	50 423.417 414	-5.07
75.284 846 2	50 423.856 01(10)	50 423.856 043	-1.02
75.284 846 2	50 423.856 10(10)	50 423.856 043	1.81
75.414 205 4	50 423.922 26(10)	50 423.922 408	-4.46
76.284 666 5	50 424.360 19(10)	50 424.360 237	-1.51
76.381 363 3	50 424.407 80(10)	50 424.407 952	-4.55
77.284 303 9	50 424.844 89(10)	50 424.844 902	-0.27
77.347 867 3	50 424.874 96(10)	50 424.875 086	-3.74
78.283 134 5	50 425.310 76(10)	50 425.310 750	0.17
78.314 338 9	50 425.324 77(10)	50 425.325 017	-7.38
79.289 989 0	50 425.762 45(10)	50 425.762 636	-5.49
80.286 622 2	50 426.193 32(10)	50 426.193 296	0.72
81.286 011 2	50 426.609 29(10)	50 426.609 338	-1.44
82.285 761 0	50 427.010 47(10)	50 427.010 455	0.51

Table S39 (*continued*)

$\nu_{F_c=1}$	$\tilde{\nu}_{\text{exp.}} \text{ (cm}^{-1}\text{)}$	$\tilde{\nu}_{\text{th.}} \text{ (cm}^{-1}\text{)}$	$E_{\text{exp.}} - E_{\text{th.}}$ ( $h \cdot \text{MHz}$ )
83.285 621 2	50 427.397 20(10)	50 427.397 257	-1.81
84.285 529 1	50 427.770 31(10)	50 427.770 392	-2.37
85.285 461 5	50 428.130 45(10)	50 428.130 489	-1.08
86.285 408 1	50 428.478 12(10)	50 428.478 144	-0.59
87.285 363 3	50 428.814 03(10)	50 428.813 922	3.21
88.285 323 7	50 429.138 38(10)	50 429.138 357	0.67
89.285 287 3	50 429.452 06(10)	50 429.451 954	3.32
90.285 252 3	50 429.755 19(10)	50 429.755 189	0.10
91.285 217 2	50 430.048 59(10)	50 430.048 513	2.30
92.285 180 5	50 430.332 36(10)	50 430.332 354	0.33
93.285 140 0	50 430.607 08(10)	50 430.607 115	-1.14
94.285 092 7	50 430.873 12(10)	50 430.873 178	-1.88
95.285 032 9	50 431.130 86(10)	50 431.130 906	-1.30
96.284 949 3	50 431.380 55(10)	50 431.380 640	-2.57
97.284 812 5	50 431.622 64(10)	50 431.622 701	-1.92
98.284 518 2	50 431.857 36(10)	50 431.857 375	-0.43
99.283 241 4	50 432.084 87(10)	50 432.084 776	2.75
101.285 898 2	50 432.520 63(10)	50 432.520 663	-1.07
102.285 595 3	50 432.728 74(10)	50 432.728 734	0.12
103.285 455 0	50 432.930 82(10)	50 432.930 825	-0.25
104.285 368 3	50 433.127 14(10)	50 433.127 141	-0.12
105.285 304 9	50 433.317 96(10)	50 433.317 895	1.88
106.285 252 6	50 433.503 29(10)	50 433.503 293	-0.04
107.285 204 9	50 433.683 53(10)	50 433.683 531	0.04
108.285 157 2	50 433.858 82(10)	50 433.858 800	0.48
109.285 104 3	50 434.029 29(10)	50 434.029 278	0.42
110.285 038 7	50 434.195 24(10)	50 434.195 139	2.93
111.284 943 5	50 434.356 60(10)	50 434.356 543	1.80
112.284 767 4	50 434.513 64(10)	50 434.513 643	0.04
113.284 220 1	50 434.666 57(10)	50 434.666 545	0.83
115.285 838 0	50 434.960 95(10)	50 434.960 894	1.54
116.285 506 9	50 435.102 28(10)	50 435.102 243	1.25
117.285 369 0	50 435.240 03(10)	50 435.240 019	0.32
118.285 284 4	50 435.374 33(10)	50 435.374 322	0.33
119.285 219 6	50 435.505 27(10)	50 435.505 265	0.15
120.285 160 7	50 435.632 93(10)	50 435.632 957	-0.72

Table S40: Predicted  $g_{\text{th}}$  and experimental  $g_{\text{exp}}$  factors of  $|\nu, L = 2, F = 3/2\rangle$  Rydberg states obtained from laser spectroscopy in an atomic beam setup as described in App. B of the main text.

$\nu_{F_c=1}$	$g_{\text{exp}}$	$g_{\text{th}}$
30.197 934 9	0.761(20)	0.748
30.249 174 5	0.981(20)	0.959
30.287 590 3	1.274(20)	1.227
31.249 137 0	0.987(20)	0.955
31.287 372 1	1.253(20)	1.226
34.174 140 5	0.785(20)	0.762
34.286 885 0	1.222(20)	1.225
35.167 245 2	0.780(20)	0.764
36.159 948 0	0.811(20)	0.767
36.286 646 7	1.190(20)	1.225
37.152 237 5	0.782(20)	0.769
37.286 544 8	1.234(20)	1.224
38.144 102 4	0.808(20)	0.771
39.135 531 7	0.806(20)	0.773
39.286 367 6	1.247(20)	1.223
41.117 038 9	0.804(20)	0.777
41.286 218 5	1.246(20)	1.223
42.286 152 5	1.217(20)	1.223
43.286 091 4	1.249(20)	1.222
44.085 756 5	0.803(20)	0.781
44.286 034 5	1.286(20)	1.222
45.285 981 5	1.242(20)	1.222
46.062 412 2	0.763(20)	0.783
46.285 932 0	1.238(20)	1.221
47.049 960 8	0.784(20)	0.784
47.285 885 6	1.328(20)	1.221
48.285 842 0	1.250(20)	1.221
49.023 445 5	0.819(20)	0.786
49.285 800 9	1.270(20)	1.221
50.994 708 8	0.835(20)	0.787
51.285 725 5	1.250(20)	1.220
51.979 480 9	0.794(20)	0.788
52.285 690 6	1.262(20)	1.220
52.963 665 6	0.833(20)	0.788
53.285 657 4	1.215(20)	1.220
54.285 625 7	1.228(20)	1.220
54.930 231 1	0.837(20)	0.789
56.285 566 2	1.242(20)	1.220
56.894 321 0	0.819(20)	0.790
57.285 538 0	1.220(20)	1.220
58.285 510 6	1.351(20)	1.219
59.285 484 0	1.277(20)	1.219
60.814 740 9	0.828(20)	0.792
61.285 432 4	1.240(20)	1.219
61.793 168 9	0.821(20)	0.792
62.285 407 0	1.231(20)	1.219
63.285 381 7	1.239(20)	1.219
64.285 356 2	1.274(20)	1.219
65.285 330 3	1.252(20)	1.219
66.285 303 7	1.237(20)	1.219
66.674 739 1	0.782(20)	0.794
67.285 275 9	1.254(20)	1.219
67.648 869 5	0.800(20)	0.794
68.285 246 5	1.238(20)	1.219
68.622 249 3	0.814(20)	0.794
69.285 214 7	1.249(20)	1.219
69.594 869 2	0.799(20)	0.795
70.566 720 2	0.826(20)	0.795
71.285 139 5	1.232(20)	1.219

Table S40 (*continued*)

$\nu_{F_c=1}$	$g_{\text{exp}}$	$g_{\text{th}}$
72.285 092 2	1.279(20)	1.218
72.508 083 0	0.819(20)	0.795
74.284 956 6	1.262(20)	1.218
75.284 846 2	1.270(20)	1.218
76.284 666 5	1.276(20)	1.217
76.381 363 4	0.799(20)	0.798
77.347 867 3	0.796(20)	0.801
78.314 338 9	0.805(20)	0.821
79.289 989 0	1.136(20)	1.096

M.  $^{171}\text{Yb D } F = 5/2$ Table S41: Laser spectroscopic data of the  $|\nu, L = 2, F = 5/2\rangle$  Rydberg series obtained from laser spectroscopy in an atomic beam setup as described in App. B of the main text.

$\nu_{F_c=1}$	$\tilde{\nu}_{\text{exp.}} \text{ (cm}^{-1}\text{)}$	$\tilde{\nu}_{\text{th.}} \text{ (cm}^{-1}\text{)}$	$E_{\text{exp.}} - E_{\text{th.}}$ ( $h \cdot \text{MHz}$ )
30.222 107 4	50 323.072 99(10)	50 323.073 113	-3.70
30.252 825 3	50 323.317 48(10)	50 323.316 972	15.23
30.283 070 3	50 323.556 42(10)	50 323.556 352	2.19
31.216 835 8	50 330.607 84(10)	50 330.607 951	-3.38
31.252 726 5	50 330.866 82(10)	50 330.866 445	11.16
31.282 833 3	50 331.082 77(10)	50 331.082 596	5.25
32.211 179 5	50 337.453 09(10)	50 337.453 048	1.35
32.252 647 9	50 337.725 13(10)	50 337.724 843	8.48
32.282 633 5	50 337.920 79(10)	50 337.920 725	1.82
33.205 133 3	50 343.690 06(10)	50 343.690 130	-2.01
33.252 583 9	50 343.973 97(10)	50 343.973 974	0.01
33.282 462 1	50 344.152 15(10)	50 344.152 079	2.04
34.198 690 4	50 349.389 14(10)	50 349.389 160	-0.62
34.252 530 9	50 349.684 00(10)	50 349.683 900	2.94
34.282 313 2	50 349.846 31(10)	50 349.846 341	-1.01
35.191 843 0	50 354.610 33(10)	50 354.610 310	0.69
35.252 486 4	50 354.914 97(10)	50 354.914 902	2.13
35.282 182 6	50 355.063 43(10)	50 355.063 484	-1.53
36.184 582 3	50 359.405 73(10)	50 359.405 566	4.98
36.252 448 5	50 359.719 20(10)	50 359.719 071	3.99
36.282 067 0	50 359.855 30(10)	50 359.855 342	-1.34
37.176 899 2	50 363.820 04(10)	50 363.820 030	0.44
37.252 415 8	50 364.141 70(10)	50 364.141 606	2.87
37.281 964 1	50 364.267 03(10)	50 364.266 902	3.98
38.168 784 2	50 367.893 01(10)	50 367.892 985	0.87
38.252 387 5	50 368.221 71(10)	50 368.221 879	-5.18
38.281 871 9	50 368.337 20(10)	50 368.337 357	-4.67
39.160 227 4	50 371.658 89(10)	50 371.658 776	3.37
39.252 362 6	50 371.994 16(10)	50 371.994 314	-4.72
39.281 788 8	50 372.100 87(10)	50 372.100 982	-3.31
40.151 218 9	50 375.147 57(10)	50 375.147 534	1.06
40.252 340 7	50 375.488 97(10)	50 375.489 115	-4.44
40.281 713 6	50 375.587 71(10)	50 375.587 852	-4.11
41.141 748 4	50 378.385 76(10)	50 378.385 784	-0.60
41.252 321 2	50 378.732 71(10)	50 378.732 868	-4.61
41.281 645 2	50 378.824 38(10)	50 378.824 448	-1.95
42.131 805 8	50 381.396 99(10)	50 381.396 950	1.17
42.252 303 7	50 381.748 93(10)	50 381.749 055	-3.83
42.281 582 8	50 381.834 05(10)	50 381.834 157	-3.21
43.121 380 5	50 384.201 83(10)	50 384.201 781	1.54
43.252 288 0	50 384.558 36(10)	50 384.558 475	-3.58
43.281 525 6	50 384.637 59(10)	50 384.637 699	-3.21
44.110 462 1	50 386.818 74(10)	50 386.818 708	1.01
44.252 273 8	50 387.179 49(10)	50 387.179 602	-3.26
44.281 473 1	50 387.253 39(10)	50 387.253 481	-2.62
45.099 040 2	50 389.264 30(10)	50 389.264 149	4.53
45.252 260 9	50 389.628 75(10)	50 389.628 895	-4.43
45.281 424 5	50 389.697 75(10)	50 389.697 900	-4.46
46.087 104 2	50 391.552 86(10)	50 391.552 768	2.78
46.252 249 1	50 391.920 91(10)	50 391.921 050	-4.22
46.281 379 6	50 391.985 44(10)	50 391.985 604	-5.00
47.074 643 6	50 393.697 80(10)	50 393.697 693	3.28
47.252 238 2	50 394.069 09(10)	50 394.069 227	-4.08
47.281 337 8	50 394.129 54(10)	50 394.129 706	-5.05
48.061 647 8	50 395.710 75(10)	50 395.710 707	1.20

Table S41 (*continued*)

$\nu_{F_c=1}$	$\tilde{\nu}_{\text{exp.}} \text{ (cm}^{-1}\text{)}$	$\tilde{\nu}_{\text{th.}} \text{ (cm}^{-1}\text{)}$	$E_{\text{exp.}} - E_{\text{th.}}$ ( $h \cdot \text{MHz}$ )
48.252 228 2	50 396.085 12(10)	50 396.085 238	-3.56
48.281 298 9	50 396.141 85(10)	50 396.141 978	-3.88
49.048 106 2	50 397.602 47(10)	50 397.602 409	1.96
49.252 218 9	50 397.979 58(10)	50 397.979 705	-3.74
49.281 262 5	50 398.032 86(10)	50 398.033 010	-4.49
50.034 008 4	50 399.382 47(10)	50 399.382 355	3.55
50.252 210 3	50 399.762 11(10)	50 399.762 205	-2.78
50.281 228 4	50 399.812 28(10)	50 399.812 348	-2.04
51.019 343 7	50 401.059 20(10)	50 401.059 179	0.61
51.252 202 3	50 401.441 26(10)	50 401.441 392	-4.03
51.281 196 3	50 401.488 49(10)	50 401.488 618	-3.91
52.004 101 7	50 402.640 73(10)	50 402.640 695	1.16
52.252 194 7	50 403.024 98(10)	50 403.025 097	-3.54
52.281 165 9	50 403.069 53(10)	50 403.069 629	-3.11
52.988 271 7	50 404.134 02(10)	50 404.133 992	0.96
53.252 187 6	50 404.520 31(10)	50 404.520 425	-3.33
53.281 137 2	50 404.562 30(10)	50 404.562 464	-4.85
53.971 843 3	50 405.545 57(10)	50 405.545 511	1.83
54.252 180 9	50 405.933 69(10)	50 405.933 830	-4.31
54.281 109 9	50 405.973 46(10)	50 405.973 560	-3.08
54.954 806 1	50 406.881 24(10)	50 406.881 117	3.71
55.252 174 5	50 407.271 09(10)	50 407.271 190	-2.87
55.281 083 8	50 407.308 66(10)	50 407.308 777	-3.43
55.937 149 4	50 408.146 25(10)	50 408.146 157	2.77
56.252 168 3	50 408.537 77(10)	50 408.537 864	-2.69
56.281 058 8	50 408.573 36(10)	50 408.573 459	-2.99
56.918 863 1	50 409.345 49(10)	50 409.345 516	-0.78
57.252 162 5	50 409.738 58(10)	50 409.738 747	-4.97
57.281 034 7	50 409.772 38(10)	50 409.772 488	-3.19
57.899 936 5	50 410.483 64(10)	50 410.483 664	-0.85
58.252 156 8	50 410.878 15(10)	50 410.878 316	-5.02
58.281 011 5	50 410.910 23(10)	50 410.910 330	-3.12
58.880 359 5	50 411.564 71(10)	50 411.564 697	0.37
59.252 151 3	50 411.960 57(10)	50 411.960 677	-3.22
59.280 988 9	50 411.990 93(10)	50 411.991 080	-4.62
59.860 121 6	50 412.592 41(10)	50 412.592 374	1.01
60.252 145 9	50 412.989 48(10)	50 412.989 595	-3.55
60.280 966 8	50 413.018 42(10)	50 413.018 493	-2.28
60.839 212 6	50 413.570 18(10)	50 413.570 148	1.01
61.252 140 6	50 413.968 47(10)	50 413.968 532	-2.01
61.280 945 2	50 413.995 91(10)	50 413.996 022	-3.48
61.817 622 3	50 414.501 21(10)	50 414.501 199	0.39
62.252 135 4	50 414.900 51(10)	50 414.900 673	-4.99
62.280 923 7	50 414.926 76(10)	50 414.926 845	-2.58
62.795 340 5	50 415.388 44(10)	50 415.388 458	-0.54
63.252 130 2	50 415.788 85(10)	50 415.788 954	-3.01
63.280 902 4	50 415.813 80(10)	50 415.813 891	-2.70
63.772 357 0	50 416.234 62(10)	50 416.234 629	-0.29
64.252 125 0	50 416.635 95(10)	50 416.636 084	-4.15
64.280 880 9	50 416.659 71(10)	50 416.659 861	-4.38
64.748 661 8	50 417.042 16(10)	50 417.042 209	-1.41
65.252 119 6	50 417.444 49(10)	50 417.444 566	-2.28
65.280 859 2	50 417.467 13(10)	50 417.467 254	-3.65
65.724 245 0	50 417.813 50(10)	50 417.813 512	-0.29
66.252 114 2	50 418.216 64(10)	50 418.216 716	-2.39
66.280 836 8	50 418.238 32(10)	50 418.238 379	-1.76
66.699 096 6	50 418.550 70(10)	50 418.550 677	0.64
67.252 108 5	50 418.954 62(10)	50 418.954 678	-1.68
67.280 813 7	50 418.975 27(10)	50 418.975 377	-3.19

Table S41 (*continued*)

$\nu_{F_c=1}$	$\tilde{\nu}_{\text{exp.}} \text{ (cm}^{-1}\text{)}$	$\tilde{\nu}_{\text{th.}} \text{ (cm}^{-1}\text{)}$	$E_{\text{exp.}} - E_{\text{th.}} \text{ (} h \cdot \text{MHz)}$
67.673 206 8	50 419.255 69(10)	50 419.255 691	0.06
68.252 102 5	50 419.660 33(10)	50 419.660 442	-3.31
68.280 789 2	50 419.680 10(10)	50 419.680 232	-3.88
68.646 566 1	50 419.930 42(10)	50 419.930 396	0.65
69.252 096 1	50 420.335 80(10)	50 420.335 853	-1.52
69.280 763 1	50 420.354 69(10)	50 420.354 785	-2.94
69.619 165 0	50 420.576 50(10)	50 420.576 505	-0.19
70.252 089 0	50 420.982 52(10)	50 420.982 627	-3.11
70.280 734 4	50 421.000 64(10)	50 421.000 749	-3.24
70.590 994 4	50 421.195 61(10)	50 421.195 613	-0.23
71.252 081 2	50 421.602 33(10)	50 421.602 361	-0.89
71.280 702 2	50 421.619 68(10)	50 421.619 716	-0.99
71.562 045 5	50 421.789 30(10)	50 421.789 203	2.80
72.280 664 9	50 422.213 11(10)	50 422.213 168	-1.73
72.532 310 3	50 422.358 80(10)	50 422.358 661	4.03
73.252 061 6	50 422.766 61(10)	50 422.766 552	1.61
73.280 620 0	50 422.782 50(10)	50 422.782 489	0.36
73.501 781 9	50 422.905 36(10)	50 422.905 279	2.45
74.252 048 5	50 423.313 63(10)	50 423.313 687	-1.77
74.280 563 4	50 423.328 93(10)	50 423.328 966	-1.21
74.470 455 4	50 423.430 22(10)	50 423.430 264	-1.21
75.252 031 5	50 423.839 07(10)	50 423.839 154	-2.59
75.280 487 2	50 423.853 70(10)	50 423.853 801	-2.93
75.438 330 4	50 423.934 77(10)	50 423.934 747	0.66
76.252 007 8	50 424.344 01(10)	50 424.344 080	-2.08
76.280 374 9	50 424.358 04(10)	50 424.358 115	-2.36
76.405 416 4	50 424.419 80(10)	50 424.419 793	0.24
77.251 971 2	50 424.829 45(10)	50 424.829 519	-2.15
77.280 184 9	50 424.842 88(10)	50 424.842 943	-1.76
77.371 751 4	50 424.886 42(10)	50 424.886 409	0.29
78.251 905 0	50 425.296 40(10)	50 425.296 454	-1.73
78.279 774 3	50 425.309 11(10)	50 425.309 213	-3.15
78.337 485 4	50 425.335 47(10)	50 425.335 589	-3.49
79.251 740 1	50 425.745 63(10)	50 425.745 784	-4.75
79.278 197 6	50 425.757 36(10)	50 425.757 443	-2.52
79.303 623 3	50 425.768 67(10)	50 425.768 637	1.08
80.250 590 1	50 426.178 04(10)	50 426.178 005	0.98
80.262 526 9	50 426.183 10(10)	50 426.183 073	0.70
80.283 970 1	50 426.192 17(10)	50 426.192 171	-0.15
81.225 075 3	50 426.584 48(10)	50 426.584 409	2.10
81.252 738 0	50 426.595 57(10)	50 426.595 733	-5.00
81.281 919 7	50 426.607 59(10)	50 426.607 666	-2.27
82.187 661 7	50 426.971 84(10)	50 426.971 743	2.94
82.252 375 3	50 426.997 22(10)	50 426.997 296	-2.40
82.281 452 5	50 427.008 68(10)	50 427.008 758	-2.26
83.148 828 5	50 427.345 16(10)	50 427.345 161	-0.15
83.252 273 1	50 427.384 60(10)	50 427.384 580	0.53
83.281 245 7	50 427.395 58(10)	50 427.395 594	-0.44
84.108 947 0	50 427.705 42(10)	50 427.705 463	-1.20
84.252 223 8	50 427.758 17(10)	50 427.758 177	-0.30
84.281 125 8	50 427.768 78(10)	50 427.768 778	0.17
85.068 089 3	50 428.053 27(10)	50 428.053 287	-0.39
85.252 193 9	50 428.118 57(10)	50 428.118 712	-4.34
85.281 045 2	50 428.128 89(10)	50 428.128 926	-1.21
86.026 274 8	50 428.389 21(10)	50 428.389 213	-0.07
86.252 173 2	50 428.466 69(10)	50 428.466 783	-2.72
86.280 985 2	50 428.476 54(10)	50 428.476 633	-2.71
86.983 507 1	50 428.713 79(10)	50 428.713 780	0.34
87.252 157 5	50 428.802 96(10)	50 428.802 957	0.25

Table S41 (*continued*)

$\nu_{F_c=1}$	$\tilde{\nu}_{\text{exp.}} \text{ (cm}^{-1}\text{)}$	$\tilde{\nu}_{\text{th.}} \text{ (cm}^{-1}\text{)}$	$E_{\text{exp.}} - E_{\text{th.}}$ $(h \cdot \text{MHz})$
87.280 937 2	50 428.812 42(10)	50 428.812 461	-1.38
87.939 783 8	50 429.027 55(10)	50 429.027 498	1.47
88.252 144 7	50 429.127 71(10)	50 429.127 769	-1.85
88.280 896 5	50 429.136 80(10)	50 429.136 945	-4.43
88.895 099 5	50 429.330 80(10)	50 429.330 846	-1.51
89.252 133 7	50 429.441 72(10)	50 429.441 725	-0.18
89.280 860 2	50 429.450 52(10)	50 429.450 588	-2.01
89.849 447 9	50 429.624 27(10)	50 429.624 277	-0.21
90.252 123 8	50 429.745 23(10)	50 429.745 304	-2.29
90.280 826 3	50 429.753 70(10)	50 429.753 869	-4.99
90.802 821 7	50 429.908 30(10)	50 429.908 220	2.43
91.252 114 3	50 430.039 01(10)	50 430.038 957	1.69
91.280 793 3	50 430.047 17(10)	50 430.047 237	-1.88
91.755 213 8	50 430.183 19(10)	50 430.183 078	3.49
92.252 104 8	50 430.323 07(10)	50 430.323 113	-1.16
92.280 759 6	50 430.331 06(10)	50 430.331 119	-1.70
92.706 616 8	50 430.449 24(10)	50 430.449 237	0.13
93.252 094 9	50 430.598 11(10)	50 430.598 176	-2.01
93.280 723 5	50 430.605 81(10)	50 430.605 921	-3.47
93.657 023 8	50 430.707 07(10)	50 430.707 060	0.41
94.252 084 0	50 430.864 48(10)	50 430.864 531	-1.52
94.280 682 6	50 430.871 96(10)	50 430.872 024	-1.89
94.606 428 9	50 430.956 93(10)	50 430.956 892	1.24
95.252 071 1	50 431.122 50(10)	50 431.122 540	-1.20
95.280 632 9	50 431.129 69(10)	50 431.129 790	-3.02
95.554 828 1	50 431.199 09(10)	50 431.199 062	0.75
96.252 054 7	50 431.372 42(10)	50 431.372 549	-3.75
96.252 054 7	50 431.372 53(10)	50 431.372 549	-0.52
96.280 567 1	50 431.379 50(10)	50 431.379 563	-2.02
96.280 567 1	50 431.379 51(10)	50 431.379 563	-1.69
96.502 221 6	50 431.433 82(10)	50 431.433 881	-1.87
96.502 221 6	50 431.433 88(10)	50 431.433 881	0.02
97.252 031 4	50 431.614 74(10)	50 431.614 883	-4.25
97.252 031 4	50 431.614 85(10)	50 431.614 883	-1.06
97.280 468 0	50 431.621 57(10)	50 431.621 665	-2.80
97.280 468 0	50 431.621 62(10)	50 431.621 665	-1.45
97.448 621 0	50 431.661 58(10)	50 431.661 649	-2.01
97.448 621 0	50 431.661 64(10)	50 431.661 649	-0.18
98.251 992 7	50 431.849 76(10)	50 431.849 853	-2.73
98.251 992 7	50 431.849 82(10)	50 431.849 853	-1.10
98.280 285 8	50 431.856 33(10)	50 431.856 397	-1.97
98.280 285 8	50 431.856 44(10)	50 431.856 397	1.19
98.394 076 2	50 431.882 58(10)	50 431.882 659	-2.53
98.394 076 2	50 431.882 72(10)	50 431.882 659	1.95
99.251 906 5	50 432.077 99(10)	50 432.077 746	7.37
99.279 781 8	50 432.084 12(10)	50 432.084 000	3.66
99.338 849 1	50 432.097 28(10)	50 432.097 236	1.30
100.251 477 0	50 432.298 78(10)	50 432.298 779	0.03
100.273 489 7	50 432.303 62(10)	50 432.303 572	1.50
100.288 693 5	50 432.306 97(10)	50 432.306 881	2.67
101.221 297 3	50 432.507 02(10)	50 432.507 005	0.35
101.252 644 8	50 432.513 62(10)	50 432.513 636	-0.36
101.281 772 3	50 432.519 83(10)	50 432.519 792	1.05
102.163 149 0	50 432.703 64(10)	50 432.703 577	1.83
102.252 290 9	50 432.721 89(10)	50 432.721 900	-0.35
102.281 251 8	50 432.727 83(10)	50 432.727 843	-0.30
103.103 307 4	50 432.894 46(10)	50 432.894 447	0.25
103.252 210 8	50 432.924 18(10)	50 432.924 200	-0.54
103.281 065 4	50 432.929 90(10)	50 432.929 950	-1.65

Table S41 (*continued*)

$\nu_{F_c=1}$	$\tilde{\nu}_{\text{exp.}} \text{ (cm}^{-1}\text{)}$	$\tilde{\nu}_{\text{th.}} \text{ (cm}^{-1}\text{)}$	$E_{\text{exp.}} - E_{\text{th.}}$ ( $h \cdot \text{MHz}$ )
104.042 245 0	50 433.080 00(10)	50 433.079 928	2.05
104.252 173 3	50 433.120 61(10)	50 433.120 714	-3.07
104.280 963 4	50 433.126 33(10)	50 433.126 289	1.35
104.980 033 3	50 433.260 23(10)	50 433.260 237	-0.25
105.252 150 0	50 433.311 65(10)	50 433.311 657	-0.20
105.280 894 3	50 433.317 19(10)	50 433.317 066	3.73
105.916 689 7	50 433.435 55(10)	50 433.435 569	-0.48
106.252 132 8	50 433.497 15(10)	50 433.497 236	-2.51
106.280 840 4	50 433.502 54(10)	50 433.502 486	1.57
106.852 217 1	50 433.606 15(10)	50 433.606 107	1.23
107.252 118 6	50 433.677 70(10)	50 433.677 648	1.55
107.280 793 4	50 433.682 72(10)	50 433.682 747	-0.95
107.786 613 7	50 433.772 11(10)	50 433.772 026	2.62
108.252 105 4	50 433.853 26(10)	50 433.853 084	5.28
108.280 748 2	50 433.858 15(10)	50 433.858 038	3.43
108.719 876 1	50 433.933 45(10)	50 433.933 492	-1.28
109.252 091 9	50 434.023 71(10)	50 434.023 725	-0.36
109.280 700 3	50 434.028 84(10)	50 434.028 538	9.02
109.652 001 1	50 434.090 79(10)	50 434.090 663	3.79
110.252 076 6	50 434.190 07(10)	50 434.189 743	9.95
110.280 643 6	50 434.194 57(10)	50 434.194 419	4.53
110.582 987 7	50 434.243 91(10)	50 434.243 692	6.48
111.252 056 9	50 434.351 71(10)	50 434.351 304	12.18
111.280 566 5	50 434.355 94(10)	50 434.355 846	2.71
111.512 841 8	50 434.392 76(10)	50 434.392 725	0.96
112.252 026 6	50 434.508 49(10)	50 434.508 565	-2.16
112.280 438 5	50 434.512 98(10)	50 434.512 972	0.22
112.441 592 2	50 434.538 11(10)	50 434.537 905	6.11
113.251 964 3	50 434.661 75(10)	50 434.661 674	2.35
113.280 130 5	50 434.665 92(10)	50 434.665 928	-0.11
113.369 381 4	50 434.679 55(10)	50 434.679 387	5.02
114.251 695 9	50 434.810 84(10)	50 434.810 750	2.71
114.277 548 2	50 434.814 58(10)	50 434.814 553	0.84
114.298 470 0	50 434.817 83(10)	50 434.817 629	5.99
115.218 487 8	50 434.951 39(10)	50 434.951 239	4.61
115.281 686 3	50 434.960 32(10)	50 434.960 300	0.47
116.143 219 2	50 435.082 43(10)	50 435.082 346	2.46
116.281 146 8	50 435.101 88(10)	50 435.101 634	7.47
117.066 107 8	50 435.210 28(10)	50 435.210 107	5.06
117.280 975 1	50 435.239 53(10)	50 435.239 421	3.20

Table S42: Predicted  $g_{\text{th}}$  and experimental  $g_{\text{exp}}$  factors of  $|\nu, L = 2, F = 5/2\rangle$  Rydberg states obtained from laser spectroscopy in an atomic beam setup as described in App. B of the main text.

$\nu_{F_c=1}$	$g_{\text{exp}}$	$g_{\text{th}}$
30.222 107 4	1.187(20)	1.255
30.252 825 3	1.023(20)	0.991
30.283 070 3	1.019(20)	1.012
31.216 835 8	1.283(20)	1.254
31.252 726 5	1.028(20)	0.983
31.282 833 3	1.027(20)	1.021
32.211 179 5	1.284(20)	1.252
32.252 647 9	1.008(20)	0.977
32.282 633 5	1.028(20)	1.029
33.205 133 3	1.254(20)	1.249
33.252 583 9	1.003(20)	0.973
33.282 462 1	1.058(20)	1.036
34.198 690 4	1.254(20)	1.247
34.252 530 9	0.977(20)	0.969
34.282 313 2	1.060(20)	1.042
35.191 843 0	1.258(20)	1.244
35.282 182 6	1.055(20)	1.048
36.184 582 3	1.268(20)	1.242
36.252 448 5	0.979(20)	0.964
36.282 067 1	1.132(20)	1.053
37.176 899 2	1.271(20)	1.239
37.252 415 8	0.984(20)	0.962
37.281 964 1	1.078(20)	1.057
38.168 784 2	1.248(20)	1.237
38.252 387 5	0.960(20)	0.960
38.281 871 9	1.079(20)	1.062
39.160 227 4	1.265(20)	1.234
39.252 362 6	0.993(20)	0.958
39.281 788 8	1.079(20)	1.065
40.151 218 9	1.246(20)	1.232
40.252 340 7	0.975(20)	0.957
40.281 713 6	1.086(20)	1.069
41.141 748 5	1.260(20)	1.230
41.252 321 2	0.972(20)	0.956
41.281 645 2	1.098(20)	1.072
42.131 805 8	1.250(20)	1.229
42.252 303 7	1.031(20)	0.955
42.281 582 8	1.089(20)	1.075
43.121 380 4	1.261(20)	1.227
43.252 288 0	0.980(20)	0.954
43.281 525 6	1.093(20)	1.077
44.110 462 1	1.228(20)	1.225
44.252 273 8	0.976(20)	0.954
44.281 473 1	1.102(20)	1.079
45.099 040 2	1.240(20)	1.224
45.252 260 9	0.968(20)	0.953
45.281 424 5	1.104(20)	1.082
46.087 104 2	1.248(20)	1.222
46.252 249 1	0.973(20)	0.952
46.281 379 6	1.094(20)	1.084
47.074 643 6	1.243(20)	1.221
47.252 238 2	0.976(20)	0.952
47.281 337 8	1.094(20)	1.085
48.061 647 8	1.237(20)	1.220
48.252 228 2	0.957(20)	0.951
48.281 298 9	1.107(20)	1.087
49.048 106 2	1.292(20)	1.219
49.252 218 9	1.023(20)	0.951
49.281 262 5	1.100(20)	1.089

Table S42 (*continued*)

$\nu_{F_c=1}$	$g_{\text{exp}}$	$g_{\text{th}}$
50.034 008 4	1.250(20)	1.218
50.252 210 3	0.974(20)	0.950
50.281 228 4	1.109(20)	1.090
51.019 343 7	1.252(20)	1.217
51.252 202 3	0.978(20)	0.950
51.281 196 3	1.132(20)	1.091
52.004 101 7	1.217(20)	1.216
52.252 194 7	0.971(20)	0.950
52.281 166 0	1.112(20)	1.093
52.988 271 7	1.247(20)	1.215
53.252 187 6	0.955(20)	0.949
53.281 137 2	1.132(20)	1.094
53.971 843 3	1.245(20)	1.214
54.252 180 9	0.948(20)	0.949
54.281 109 9	1.125(20)	1.095
54.954 806 1	1.224(20)	1.214
55.252 174 5	0.968(20)	0.949
55.281 083 8	1.110(20)	1.096
55.937 149 4	1.258(20)	1.213
56.252 168 3	0.966(20)	0.949
56.281 058 8	1.128(20)	1.097
56.918 863 1	1.224(20)	1.212
57.252 162 5	0.963(20)	0.948
57.281 034 7	1.133(20)	1.098
57.899 936 5	1.228(20)	1.212
58.252 156 8	0.962(20)	0.948
58.281 011 5	1.114(20)	1.098
58.880 359 5	1.238(20)	1.211
59.252 151 3	0.974(20)	0.948
59.280 988 9	1.129(20)	1.099
59.860 121 6	1.218(20)	1.211
60.252 145 9	0.944(20)	0.948
60.280 966 8	1.139(20)	1.100
60.839 212 6	1.236(20)	1.210
61.252 140 7	0.974(20)	0.948
61.280 945 2	1.124(20)	1.100
61.817 622 3	1.216(20)	1.210
62.252 135 4	0.968(20)	0.947
62.280 923 7	1.132(20)	1.101
62.795 340 5	1.236(20)	1.209
63.252 130 2	0.963(20)	0.947
63.280 902 4	1.129(20)	1.102
63.772 357 0	1.226(20)	1.209
64.252 125 0	0.982(20)	0.947
64.280 880 9	1.129(20)	1.102
64.748 661 8	1.237(20)	1.209
65.252 119 6	0.965(20)	0.947
65.280 859 2	1.101(20)	1.103
65.724 245 0	1.240(20)	1.208
66.252 114 2	0.953(20)	0.947
66.280 836 8	1.150(20)	1.103
66.699 096 5	1.228(20)	1.208
67.252 108 5	0.968(20)	0.947
67.280 813 7	1.147(20)	1.104
67.673 206 8	1.209(20)	1.208
68.252 102 5	0.937(20)	0.946
68.280 789 2	1.118(20)	1.104
68.646 566 1	1.219(20)	1.207
69.252 096 1	0.961(20)	0.946
69.280 763 1	1.118(20)	1.105

Table S42 (*continued*)

$\nu_{F_c=1}$	$g_{\text{exp}}$	$g_{\text{th}}$
69.619 165 0	1.217(20)	1.207
70.252 089 0	0.969(20)	0.946
70.280 734 4	1.128(20)	1.105
70.590 994 4	1.248(20)	1.207
71.252 081 2	0.973(20)	0.946
71.280 702 1	1.134(20)	1.106
71.562 045 5	1.216(20)	1.206
72.280 664 9	1.140(20)	1.106
72.532 310 3	1.232(20)	1.206
73.252 061 6	0.994(20)	0.945
73.280 620 0	1.062(20)	1.107
73.501 781 9	1.228(20)	1.206
74.252 048 5	0.960(20)	0.945
74.280 563 4	1.121(20)	1.107
74.470 455 4	1.231(20)	1.205
75.252 031 5	0.953(20)	0.945
75.280 487 2	1.140(20)	1.108
75.438 330 4	1.239(20)	1.205
76.252 007 8	0.970(20)	0.944
76.280 374 9	1.135(20)	1.109
76.405 416 4	1.232(20)	1.205
77.251 971 2	0.960(20)	0.944
77.280 184 9	1.130(20)	1.111
77.371 751 4	1.232(20)	1.204
78.251 905 0	0.935(20)	0.943
78.279 774 3	1.132(20)	1.114
78.337 485 4	1.232(20)	1.201
79.251 740 2	0.974(20)	0.941
79.278 197 6	1.159(20)	1.130
79.303 623 3	1.200(20)	1.187
80.262 526 9	1.218(20)	1.199
80.283 970 1	1.141(20)	1.108
81.225 075 3	1.211(20)	1.189
81.252 738 0	0.977(20)	0.965
81.281 919 7	1.114(20)	1.104
82.187 661 8	1.216(20)	1.201
83.148 828 4	1.227(20)	1.202
83.252 273 1	0.965(20)	0.950

- 
- [S1] R. Zerneck, L. Caiyan, J. Zhankui, and J. Larsson, Landé  $g_J$  factor measurements in the  $6snd\ 1,3D_2$  sequences of Yb I, *Z. Phys. D* **37**, 259 (1996).
- [S2] M. Aymar, R. J. Champeau, C. Delsart, and O. Robaux, Three-step laser spectroscopy and multichannel quantum defect analysis of odd-parity Rydberg states of neutral ytterbium, *J. Phys. B: At. Mol. Phys.* **17**, 3645 (1984).
- [S3] W. F. Meggers and J. L. Tech, The First Spectrum of Ytterbium (Yb I), *J. Res. NBS* **83**, 13 (1977).
- [S4] P. Camus, A. Débarre, and C. Morillon, Highly excited levels of neutral ytterbium. I. Two-photon and two-step spectroscopy of even spectra, *J. Phys. B: At. Mol. Phys.* **13**, 1073 (1980).
- [S5] M. Aymar, A. Débarre, and O. Robaux, Highly excited levels of neutral ytterbium. II. Multichannel quantum defect analysis of odd- and even-parity spectra, *J. Phys. B: At. Mol. Phys.* **13**, 1089 (1980).
- [S6] H. Lehec, A. Zuliani, W. Maineult, E. Luc-Koenig, P. Pillet, P. Cheinet, F. Niyaz, and T. F. Gallagher, Laser and microwave spectroscopy of even-parity Rydberg states of neutral ytterbium and multichannel-quantum-defect-theory analysis, *Phys. Rev. A* **98**, 062506 (2018).
- [S7] H. Maeda, Y. Matsuo, M. Takami, and A. Suzuki, Optical-microwave double-resonance spectroscopy of highly excited Rydberg states of ytterbium, *Phys. Rev. A* **45**, 1732 (1992).
- [S8] H. Lehec, *Spectroscopie Rydberg et excitation du coeur isolé d'atomes d'ytterbium ultra-froids*, Ph.D. thesis, Université Paris Saclay (COMUE) (2017).
- [S9] P. Camus and F. S. Tomkins, Spectre d'absorption de Yb I, *J. Physique* **30**, 545 (1969).
- [S10] W. C. Martin, R. Zalubas, and L. Hagan, Atomic Energy Levels: The Rare Earth Elements, *Nat. Stand. Ref. Data Ser., NSRDS-NBS* **60**, 10.6028/NBS.NSRDS.60 (1978).
- [S11] W. Bi-ru, Z. You-feng, X. Yun-fei, P. Li-gang, L. Ji, and Z. Jian-wei, The  $6snp\ 3P_{0,2}$  Rydberg series of neutral ytterbium, *J. Phys. B: At., Mol. Opt. Phys.* **24**, 49 (1991).
- [S12] R. Ali, M. Yaseen, A. Nadeem, S. A. Bhatti, and M. A. Baig, Two-colour three-photon excitation of the  $6snf\ 1,3F_3$  and  $6snp\ 1P_1, 3P_{1,2}$  Rydberg levels of Yb I, *J. Phys. B: At., Mol. Opt. Phys.* **32**, 953 (1999).
- [S13] J.-F. Wyart and P. Camus, Extended Analysis of the Emission Spectrum of Neutral Ytterbium (Yb I), *Phys. Scr.* **20**, 43 (1979).
- [S14] U. Majewski, *"Hochauflösende Laserspektroskopie von Ytterbium-Rydbergzuständen"*, Diploma thesis, Freie Universität Berlin (1985).
- [S15] Compiled spectroscopic data used in the analysis of MQDT models presented in "Spectroscopy and modeling of  $^{171}\text{Yb}$  Rydberg states for high-fidelity two-qubit gates" (2024).
- [S16] M. L. Zimmerman, M. G. Littman, M. M. Kash, and D. Kleppner, Stark structure of the Rydberg states of alkali-metal atoms, *Phys. Rev. A* **20**, 2251 (1979).